Solid Catalysts Designed for Carbon Dioxide Conversion

二酸化炭素転換用固体触媒の設計

Lisheng Guo

郭立升

Supervisor: Prof. Noritatsu Tsubaki

Tsubaki Laboratory
Graduate School of Science and Engineering for Education
University of Toyama

Preface

For the past two centuries, carbon-rich fossil fuels, such as coal and natural gas have been utilized in promoting the development of the economic society. This has caused massive carbon dioxide emission that has resulted in a series of ecological problems such as global warming and ocean acidification. Various strategies have, therefore, been adopted in the utilization, storage and capture of carbon dioxide to mitigate the concentration of carbon dioxide in the air. Rather than a waste resource, carbon dioxide turns out to be a promising C1 building block to fabricate a series of value-added chemicals. Compared to the capture and storage of carbon dioxide, the transformation and utilization of carbon dioxide are more attractive in the long term. The utilization of carbon dioxide can provide an alternative way to convert the renewable raw material into useful chemicals or fuels and simultaneously realize the effective circulation of global carbon resources. Generally, CO_2 hydrogenation to hydrocarbons takes two steps: first initial reduction of CO_2 to CO through reverse water-gas shift (RWGS) reaction, and then chain propagation reaction via the Fischer-Tropsch synthesis (FTS) reaction. Thereinto, at the end of the 1920s, FTS was first mentioned by Hans Fischer and Franz Tropsch and from then on, the FTS is regarded as an alternative pathway to producing valuable fuels and chemicals from nonpetroleum sources. Thereinto, syngas (mixtures of CO and H_2) as a key intermediate is a good link between carbon dioxide reactants and valuable hydrocarbons, expanding the application range of CO_2 gases.

In chapter 1, we designed a bimetallic catalyst through impregnation method for catalyzing CO_2 into liquid hydrocarbons. The introduction of cobalt metal increases the adsorption ability of CO_2, which promotes the CO_2 activation over iron species through

RWGS reaction. Besides, the carbide content also increases significantly with the further introduction of cobalt metal in comparison to potassium modified one, achieving a high C-C bond coupling activity. Therefore, K-Co/Fe showed better activity of 29.4% and lower CO selectivity of 15.7% than K-Fe (23.3% CO_2 conv. and 30.2% CO sel.). CO_2 conversion was limited by the thermodynamics, and the equilibrium conversion was generally less than 40% under normal operation conditions. To further enhance the catalytic activity of CO_2 hydrogenation via ex situ water removal manner, a two-stage reactor system was developed and investigated, where the water product formed by RWGS reaction was trapped in the first ice-trap and the mixtures (including CO_2, CO, light hydrocarbons) sequentially entered the second reactor. Facts proved that ex situ water removal is of great significance in enhancing catalytic activity and reducing the selectivity of CO by-product. This effectively promotional effect derived from water removal facilitates constructing a new route for improving the catalytic performance of CO_2 conversion, further enhancing the yield of liquid fuel.

In chapter 2, a nitrogen functionalized carbon with embedded iron nanoparticles was developed by a simple one-pot hydrothermal synthesis process for improving CO_2 hydrogenation performance. Four different nitrogenous reagents (ethylenediamine, pyridine, and diethylformamide, and pyrrolidine) were adopted to synthesize the functionalized catalysts. The characterization and catalytic performance evaluation revealed that different nitrogen sources have various effects on physical-chemical properties of catalysts. The improved CO_2 hydrogenation performance over these functionalized catalysts was found to be correlated with the specific surface areas, the carbonization degree of iron species precursor, the amount of defect sites, and the content of pyridine-like nitrogen structures, which are determined by the doping nitrogen atom

types. Pyrrolidine as a well-performing nitrogen source precisely regulated the physiochemical properties of the final catalyst, consequently achieving an outstanding performance. Correspondingly, Fe/C-PYL shows the highest reaction activity (21.6%) and the lowest CO selectivity (29.2%) among these catalysts.

In chapter 3, a promising Ni based mesoporous Al_2O_3 catalyst was prepared by one-step evaporation-induced self-assembly (EISA) method, and was employed as an efficient catalyst in combined methane dry reforming (DRM) and methane partial oxidization (POM) reaction. For comparison, a supported catalyst with ordered mesoporous Al_2O_3 was also prepared by sample impregnation method. The catalytic activity tests results indicated that the catalysts prepared by the one-pot method had better catalytic performance for combined methane dry reforming and methane partial oxidation reaction, ascribing to the larger exposed metal Ni surface area of Ni-MA than that of Ni/MA. Meanwhile, the catalytic performance remained stable at 750 °C for 100 h reaction. The characterization results of used catalysts indicated that combined POM with DRM could effectively suppress carbon deposition.

In chapter 4, a carbon dioxide hydrogenation to olefin process achieves 72% selectivity for alkenes and 50.3% selectivity for C_{4-18} alkenes, of which formation of linear α-olefins accounts for 80%. Besides, the biopromoters-driven iron catalyst presents a highest activity (31.0% CO_2 conv.). The process is catalyzed by carbon-supported iron, commonly used in C-C coupling reactions, with multiple alkali promoters extracted from corncob. The design is based on the synergistic catalysis of mineral elements in biomass enzyme on which carbon dioxide can be directly converted into carbohydrate. The mineral elements from corncob may promote the surface enrichment of potassium, suppressing the secondary hydrogenation of alkenes on active sites. Furthermore,

carburization of iron species is enhanced to form more Fe_5C_2 species, promoting both the reverse water-gas shift reaction and subsequent C-C coupling.

Herein, four types of catalysts with special structures were rationally designed, synthesized and applied to transform the carbon dioxide greenhouse gases into valuable chemicals or syngas. The physical-chemical properties and catalytic performances of these efficient catalysts were also studied in detail to shed new insights for solid catalyst design.

Content

Content

Chapter 1

Enhanced Liquid Fuel Production from CO_2 Hydrogenation: Catalytic Performance of Bimetallic Catalysts over a Two-Stage Reactor System

Catalytic performance of CO_2 hydrogenation is conveniently improved via a cobalt-doped iron-based catalyst. The enhanced performance for CO_2 hydrogenation is ascribed to the improvement of CO_2 activation and chain propagation reaction. The two-stage reactor system with ex situ water removal further provides a straightforward access for enhancing the yield of liquid fuel.

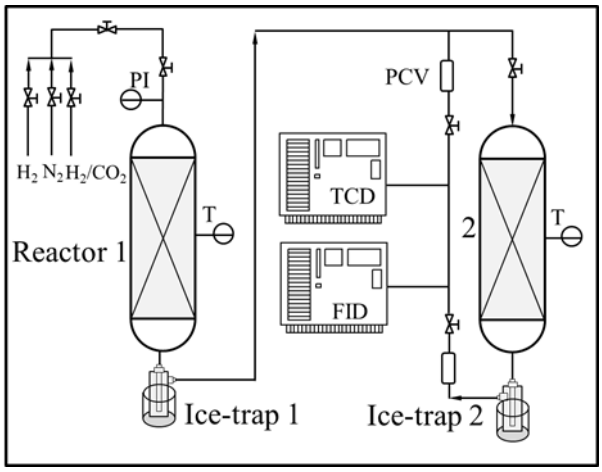

Abstract

A bimetallic catalyst combining Fe and Co active sites enables direct conversion of CO_2 to hydrocarbons with a higher activity but modest CO selectivity compared with a sole Fe catalyst. The introduction of cobalt metal increases the adsorption ability of CO_2, which promotes the CO_2 activation over iron species through RWGS reaction. Besides, the carbide content (Fe_5C_2) also increases significantly with the further introduction of cobalt metal in comparison to potassium modified one, achieving a high C-C bond coupling activity. On the basis, the catalytic performance of CO_2 hydrogenation over this bimetallic catalyst was investigated in a two-stage reactor system, where the influence of number of reactors on CO_2 conversion and the catalytic performance over each reactor were analyzed regarding the yield of liquid fuel. A significant increase in liquid fuel production was achieved under ordinary conditions. It was proven that ex situ water removal plays the determining role in the integrated process for improving the catalytic activity and lowering the selectivity of undesired CO by-product. The utilization of a two-stage reactor system promotes CO_2 conversion, making the CO_2 conversion approaching a higher value (69.9%). Meanwhile, the yield of liquid fuel exceeds 300 $g_{fuels}/(kg_{cat}h)$ under conventional conditions.

Keywords: CO_2 hydrogenation, Two-stage reactor system, Bimetallic catalysts, Ex situ water removal, Liquid fuel,

1.1. Introduction

Considering the stern environmental pressure and global ecologic problems caused by greenhouse gases, the reduction of CO_2 emissions from production and living has become one of more focused research topics in this century [1-3]. Contrary to carbon capture and storage (CCS), the reutilization of catalyzing CO_2 to valuable chemicals or fuels provides a new path. Based on the concept of reutilization, plentiful studies have been done on CO_2 conversion including electrocatalysis, photocatalysis and thermalcatalysis [4-9]. In terms of the high energy density, convenient storage and transportation performance, the production of liquid fuel by utilizing CO_2 conversion has important economic benefits and advantages compared with low-carbon hydrocarbons. In these methods, catalytic conversion of CO_2 is a promising route to produce valuable liquid fuel with a certain production scale.

Generally, CO_2 hydrogenation to hydrocarbons usually takes two steps: first initial reduction of CO_2 to CO through reverse water-gas shift (RWGS) reaction, and then chain propagation reaction via the Fischer-Tropsch synthesis (FTS) reaction [10, 11]. Although Fe-based catalysts are intensively used for CO_2 conversion, the catalytic activity and selectivity of desired products over sole Fe catalysts cannot meet demand including catalytic activity and selectivity. Thereinto, the activity of CO_2 conversion was hindered by the rate-determining step of chain propagation reaction while the selectivity of desired products was limited by Anderson-Schulz-Flory (ASF) model. These challenges make it difficult to produce large amounts of liquid fuel from CO_2 hydrogenation. As a consequence, many different methods, from the catalyst preparation to operation conditions, have been investigated to solve this problem. One of the most common methods is to modify the catalysts by dopant addition such as potassium (K), and

manganese (Mn) promoter [11-14]. The introduction of K not only regulates the surface adsorption proprieties, but also promotes the formation of active carbides which is beneficial for the formation of liquid fuel [13, 15, 16]. Mn acts as an electronic as well as a structural promoter promoting the dispersion and carburization of iron oxides, thus favoring the formation of liquid fuel [17, 18]. Besides, the special spinel precursors such as $ZnFe_2O_4$ was applied to catalyze CO_2 hydrogenation, and exhibited a high selectivity of liquid fuel [19, 20]. Meanwhile, the bifunctional catalysts combing metal oxides with zeolite catalysts were also investigated for CO_2 conversion, and a high selectivity of liquid fuel was also achieved on these catalytic systems [4, 5]. The excellent performance can be attributed to the proper distance and the benign synergistic effect of different active sites. In addition, constructing a bimetallic catalyst combining the intrinsic merit of Fe and Co metal was also investigated recently [21-27]. Previous findings suggest that the introduction of cobalt can regulate the adsorption properties of hydrogen for facilitating carbon-carbon bond formation, and then it promotes the formation of higher hydrocarbons [23, 28, 29]. Indeed, the introduction of highly active Co in Fe significantly promotes the CO_2 hydrogenation activity, as reported previously. Although these bimetallic catalysts achieved a well catalytic performance, the role of Co metal on CO_2 hydrogenation reaction has not been explained in detail. Besides, facile design and preparation of functional catalysts for the synthesis of renewable fuel, are still a severe challenge for the upgrading of CO_2 hydrogenation products.

Despite many efforts to improve catalytic performance including selectivity or/and activity, the space time yield (STY) of liquid fuel limited by selectivity and activity simultaneously, is usually less than 100 $g_{fuels}/(kg_{cat}h)$. Even for these bifunctional catalysts with excellent catalytic performance, the catalytic yield is still less than 150 $g_{fuels}/(kg_{cat}h)$

[4, 5]. Further increase in the yield of liquid fuel has become more difficult from the perspective of catalyst design. Thus, a new strategy is indispensable to improve the catalytic yield. Considering the detrimental effect of H_2O formed by RWGS reaction, the method of ex situ water removal is an effective means to improve the yield of liquid fuel. In reality, although tandem reactors with water removal can improve CO_2 hydrogenation performance, few studies have considered the effect of reactor number on the performance of CO_2 conversion [30]. Therefore, we fabricate a bimetallic catalyst for improving the catalytic performance and investigate the effect of cobalt dopants on the catalytic performance of CO_2 hydrogenation. On the basis we further take advantage of a two-stage reactor system applied for ex situ water removal to enhance CO_2 conversion, and investigate the effects of the two-stage reactor system on catalytic performance.

1.2. Experimental

1.2.1 Catalyst Preparation

The sole Fe catalyst was prepared by ammonia precipitation method. Typically, $Fe(NO_3)_3 \cdot 9H_2O$ solution and $NH_3 \cdot H_2O$ solution were added into deionized (DI) water containing a certain amount of ammonia with stirring to form a suspension solution. In the above solution, $Fe(NO_3)_3 \cdot 9H_2O$ solution and $NH_3 \cdot H_2O$ solution were added drop wise under stirring, and the pH value of suspension was always maintained at 10. Consequently, the resulting suspension was kept at 60 °C for 7 hours. The collected precipitate was filtered and washed with DI water. The resulting precipitate was dried at 120 °C for 10 hours. KNO_3, $Co(NO_3)_3 \cdot 6H_2O$ or $Ru(NO_3)_3$ solution was selected as potassium, cobalt or ruthenium source, and was introduced into sole Fe catalyst via a simple impregnation method. The obtained products were calcined at 550 °C for 5 hours. The value of x% and

y% in the xK-yM/Fe catalysts represents weight percentage of K/Fe and M/Fe. Unless otherwise specified, 5K-10Co/Fe or 5K-10Ru/Fe is marked as K-Co/Fe and K-Ru/Fe respectively, which is in accordance to the characterization results (Table 1.1).

1.2.2 Catalyst characterization

XRD spectra of the powder catalysts were recorded by a Rigaku RINT 2400 X-ray Diffractometer using Cu-Ka (40 kV, 20 mA) irradiation. Scans were recorded in the 2θ range of 5-90^{o} with a step size of 0.02 ^{o}/s. N_2 physisorption was performed on a Micromeritics analyzer. Before sample analysis, the catalysts were vacuum dried at 120 ^{o}C for 6h. Scanning electron microscopy (SEM) images were taken by a JEOL JSM-6360LV microscope operated at an accelerating voltage of 10 kV, which were used to obtain the surface morphology and elemental composition of the prepared catalysts. SEM with dispersive spectroscopy (SEM-EDS, JED-2300 energy dispersive spectroscopy) was used to analysis element composition. The X-ray photoelectron spectroscopy (XPS) analysis was conducted on Thermo Fisher Scientific ESCALAB 250Xi multifunctional X-ray photoelectron spectroscopy. The adsorption and reduction properties of as-prepared catalysts were determined by a BELCAT-II-T-SP Characterization System. The analysis of element composition was also evaluated by a PHILIPS PW2404R X-ray spectrometer.

1.2.3 Catalytic performance test

CO_2 hydrogenation reactions were performed in a continuous flowing two-stage reactor system with an inner diameter of 6 mm (Scheme 1.1). Prior to reaction, the prepared catalysts were in situ reduced at 380 ^{o}C for 10 h in a pure H_2 flow (40 ml min^{-1}, atmospheric pressure). After reduction, the reactor was cooled to reaction temperature. Then the reactant gas mixture CO_2/H_2/Ar was fed into the reactor, and the system was

pressured gradually to reaction pressure. The effluents of the reaction were analyzed by an online gas chromatograph with a TCD detector. Light hydrocarbons were analyzed by an online gas chromatograph with a flame ionization detector (FID). Besides, ice trap with n-octane as solvent was equipped to capture the liquid hydrocarbons in the effluents. Liquid hydrocarbons from the ice trap were analyzed by an off-line gas chromatograph using an FID.

Moreover, the selectivity of hydrocarbon was calculated based on the total carbon moles with a unit of C-mol% on all tested catalysts. The catalytic performances after at least 6 h on stream were typically used for discussion. The CO_2 conversion was calculated by equation (1). CO and hydrocarbon selectivity were calculated according to equation (2) and (3) respectively.

$$CO_{2\ conversion\ (\%)} = (CO_{2\ in}\text{-}CO_{2\ out})/CO_{2\ in} \times 100\% \quad (1)$$

CO_2 in: mole fraction of CO_2 in the inlet, CO_2 out: mole fraction of CO_2 in the outlet.

$$CO_{selectivity\ (\%)} = CO_{out}/ (CO_{2\ in}\text{-}CO_{2\ out}) \times 100\% \quad (2)$$

CO out: mole fraction of CO in the outlet.

$$C_{i\ hydrocarbon\ selectivity\ (C\text{-}mol\ \%)} = \text{Mole of } C_{i\ hydrocarbons} / \text{Mole of total hydrocarbon} \times 100\% \quad (3)$$

1.3. Results and discussion

1.3.1 Structure and surface properties of catalysts

Scanning electron microscopy (SEM) was applied to obtain the surface morphology (Figure 1.1). As can be seen, all three catalysts (5K-Fe, 5K-10Co/Fe, and 5K-10Ru/Fe) have irregular polyhedral block structures. The average diameters of these massive structures are greater than 10 μm. Compared with the as-prepared catalysts, the morphologies and structures of these spent catalyst changed little except for 5K-Fe

catalyst. It indicates that the introduction of Ru or Co is more conducive to maintaining structural stability.

The obtained structural properties of as-prepared and spent Fe, 5K-Fe and 5K-10Co/Fe catalysts were characterized using XRD analyses, as shown in Figure 1.2. As for as-prepared catalysts, the main phase is Fe_2O_3 in these catalysts regardless of the addition of K or/and Co element. Meanwhile, no additional peaks of K or/and Co substances were found probably because of the uniform distribution of particles or fine particle sizes. Different from the as-prepared catalysts, the spent catalysts exhibited some difference in carbide peaks. The content of active carbides (Fe_5C_2, JCPDS 20-0509) was evidently enhanced with the doping of K promoter, which was beneficial for promoting the carbonization of iron species [13, 16, 33]. The content of iron carbides was further increased with the introduction of Co additives, therefore it demonstrating that the existence of Co metal promoter exerted a positive effect on the carbonization of iron species. According to the related reports above, iron and cobalt can form an alloy catalyst under similar reaction conditions [24, 25]. However, as shown in Figure 1.2, there are no peaks ascribed to CoFe alloy. It suggests that in addition to the possible formation of alloys, there may be other factors that further promote the catalytic activity. It has previously been reported that the carbon monoxide dissociation barrier is lower on the cobalt metal surface [45], thus the existence of cobalt active sites may also improve catalytic performance by providing a more active carbon monoxide intermediate. Based on the above two considerations, the presence of cobalt may play a role in two aspects: one is the formation of bimetallic catalytic active sites (FeCo alloy), which promote the reaction performance through the synergistic action between cobalt and iron, and the other is the independent cobalt species active sites providing more active CO* intermediates,

achieving a low CO selectivity. Compared with 5K-Fe and 5K-10Co/Fe catalysts, the weak diffraction peak may be due to the post-treatment process such as calcination process. N_2 physisorption measurement was applied to investigate the specific surface area of reference 5K-Fe, 5K-10Co/Fe and 5K-10Ru/Fe (Table 1.2). As can be seen, the surface area and pore volume varied little with the introduction of K, Co or Ru (between 10.8-12.9 m^2/g). All of these catalysts have a low surface area and pore volume, which indicate that these catalysts are nonporous.

Given that CO_2 activation and chain propagation reaction occurred on the surface of catalyst, X-ray photoelectron spectroscopy (XPS) was applied to further investigate the phase composition and the content of surface species. The binding energy peaks at 711.7, 711.0, and 707.3 eV in the Fe2p spectrum are respectively ascribed to Fe^{III}, Fe^{II}, and Fe-C (Figure 1.3) [34]. According to the spectra results after curve fitting, the carbide content was increased with the addition of alkali metal K promoter, which is in accordance with XRD results. Besides, the carbonization degree of iron species on the catalyst surface was improved again with the introduction of cobalt additives. The carbide content of 18% over a 5K-10Co/Fe is much higher than that of 5K-Fe (7.9%, Table 1.3 and Figure 1.3), which indicates that Co additives can promote the formation of active carbides on catalyst surface. As an active phase (Fe_5C_2) for chain propagation reaction, the increased carbide content can promote C-C bond coupling reaction, which is beneficial for the highly selective formation of liquid hydrocarbons [19]. Therefore, Co additives as an effective metal dopant can improve the reaction performance by further promoting the formation of carbides. However, the promotional effect on the carbonation degree of iron species from ruthenium metal was significantly weaker than that of cobalt metal (Table 1.3 and Figure 1.4). The inferior carbonation degree of iron species was responsible for the poor

hydrogenation performance over a Ru/Fe catalyst (Table 1.3 and Table 1.4).

Given that the metal oxide reduction and reactant adsorption states are key factors influencing CO_2 activation and hydrogenation, the properties of H_2 reduction as well as CO and CO_2 adsorption for Co doped Fe catalysts were investigated by employing the temperature-programmed reduction (H_2-TPR), CO and CO_2 temperature-programmed desorption (CO-TPD, CO_2-TPD) techniques. According to the H_2-TPR profiles (Figure 1.5), the peaks drifted toward lower temperature with the addition of Co metal, which means that Co addition is beneficial for the reduction of iron species. The improvement of reduction performance could be due to the induction behavior of cobalt oxide reduction, owing to the easier reduction of cobalt oxides compared with iron oxides [35, 36]. When Co dopant was introduced into 5K-Fe catalyst, CO_2 adsorption was increased significantly as compared in Figure 1.6a. The adsorption intensity of CO_2 reached its maximum level when the mass ratio of Co/Fe was 20%, and then decreased with the further increase of Co/Fe mass ratio.

To investigate the effect of adsorption strength on the catalytic performance, the K-Fe based catalysts with different Co/Fe mass ratio were evaluated and compared in Figure 1.6b. CO_2 conversion was increased with the increase of CO_2 adsorption strength while CO selectivity was suppressed evidently from 30.2% to 10.6%. However, the further introduction of superfluous Co metal would cover active sites for CO_2 activation and subsequent C-C bond coupling reaction, thus it led to an inferior catalytic performance as in Figure 1.6b. All these findings prove that the suitable amount introduction of Co metal promotes CO_2 adsorption, and the enhanced CO_2 adsorption is conducive to subsequent CO_2 activation on iron active sites to some extent which is beneficial for promoting CO_2 conversion. Although the introduction of Co additives promotes the reduction and

adsorption process, the change of CO adsorption states is not obvious (Figure 1.7). Thus, the introduction of Co dopant is more conducive to promoting CO_2 adsorption than CO intermediates formed by RWGS reaction, the adsorbed CO_2 was converted into CO intermediates on the surface of iron species followed by chain propagation reaction. The combination of these merits led to a high CO_2 catalytic activity as well as a low CO selectivity (Table 1.4), which is advantageous for the utilization of carbon element.

To further demonstrate the promotional effect of cobalt addition on CO_2 hydrogenation reaction, the atmospheric pressure platform reactions were investigated as illustrated in Figure 1.8. These catalysts showed no any catalytic activity when the reaction temperature was lower than 220 ^oC. When the reaction temperature reached 220 ^oC, these catalysts began to convert CO_2. CO_2 conversion increased when enhancing reaction time during 220 and 260 ^oC periods. Although the conversion was increased with the prolonged of reaction time, no methane was produced between 220 to 260 ^oC for 120 minutes reaction regardless of the types of catalysts, demonstrating that only the RWGS reaction occurred under this condition. Clearly, 5K-Fe catalyst with the modification of cobalt showed the highest activity of RWGS reaction, followed by 5K-Fe and 5K-10Ru/Fe catalysts. It manifests that the introduction of cobalt in 5K-Fe catalyst will promote reduction behavior of CO_2 over iron species via a RWGS reaction compared with 5K-Fe and 5K-10Ru/Fe catalyst.

Based on surface composition analysis, CO_2 adsorption strength results as well as platform reaction performances, we can learn that the improvement of CO_2 hydrogenation performance is closely related to these factors. Generally, Co metal is thought to improve C-C bond coupling and then further enhance the activity. According to XPS and XRD results (Figure 1.2 and 1.3), the existence of cobalt promotes the carbonization degree of

iron species, which is crucial for the C-C coupling reaction. The enhanced CO_2 adsorption capacity contributes to the activation of CO_2. Platform reaction performances also demonstrate the modified effect for RWGS reaction. In reality, the existence of cobalt metal in a bimetallic 5K-10Co/Fe catalyst will promote RWGS and C-C coupling reaction simultaneously, based on experimental and characterization results, thus CO_2 conversion goes up and CO selectivity goes down. The introduction of Co metal first promotes the adsorption of CO_2, and then the adsorbed CO_2 is converted in CO intermediates over iron species. Subsequently, surface-adsorbed CO is hydrogenated to hydrocarbons over active species. Thus, this enhanced interface reaction coupling improves the performance of CO_2 hydrogenation.

1.3.2 Catalytic performance of varied catalysts for CO_2 hydrogenation

The catalytic performances of CO_2 hydrogenation on as-prepared Fe-based catalysts were evaluated, as shown in Table 1.4. Catalytic activity of CO_2 conversion was increased from 16.8 to 23.3 % with the addition of K promoter, and CO selectivity decreased from 44.0 to 30.2%. According to Figure 1.2 and Figure 1.3, although the characteristic peak of as-prepared catalyst did not change significantly with the introduction of electronic promoter K. However, for the spent catalysts, the diffraction peaks of metal Fe was significantly reduced. At the same time, the diffraction peaks of active carbide (Fe_5C_2) were obviously enhanced, indicating that the introduction of K promoter was helpful to carbonization of iron species, which is important for enhancing catalytic activity. With the introduction of Co additives, catalytic activity of CO_2 hydrogenation was further improved. Meanwhile, the CO selectivity was decreased again with the introduction of Co additives for 5K-10Co/Fe catalysts. Therefore, when the iron catalyst was modified by K and Co, it showed the highest activity of 29.4% and the lowest selectivity of 15.7%.

As discussed above, the introduction of cobalt metal on the one hand promotes the increase of carbide content and on the other hand improves the adsorption behavior of CO_2 on the surface of catalyst, which are key factors to promote the performance improvement. The value of x% and y% in the xK-yM/Fe catalysts represents weight percentage of K/Fe and M/Fe. It indicates that the introduction of cobalt dopants can increase the reaction activity as well as lower CO selectivity evidently, thus it promotes the utilization of carbon element and the yield of liquid fuel. If the rate-determining step of chain propagation reaction is overcome, the driving force pushing CO intermediates to liquid hydrocarbons will promote the CO_2 conversion via a reversible RWGS reaction, a principle for designing bimetallic catalysts [21]. Therefore, a metal with a high activity for chain propagation reaction may present a good reaction performance for CO_2 hydrogenation if this special metal replaces Co metal. Compared with Co-based catalysts, Ru-based catalysts generally exhibit a higher catalytic activity and higher C-C bond coupling activity. According to the Table 1.5, the FTS CO conversion and C-C bond coupling activity from 5K-10Ru/Fe, as expected, was higher than that from 5K-10Co/Fe. It indicated that the introduction of Ru has contributed to C-C bond coupling reaction and the formation of hydrocarbons. On this basis we used these two catalysts (5K-10Ru/Fe, 5K-10Co/Fe) for CO_2 hydrogenation. On the contrary, a higher CO_2 conversion and a lower selectivity of CO were obtained from 5K-10Co/Fe rather than 5K-10Ru/Fe, as compared in Table 1.4. To some extent, the enhanced performance for CO_2 hydrogenation over a bimetallic 5K-10Co/Fe catalyst is more than just promoting the C-C bond coupling reaction by a simple comparison experiment. Considering that the reaction performance is affected by the preparation of the catalyst and the operating conditions, the various bimetallic catalysts generally show different catalytic performance [31, 32]. Therefore,

another kind of metal used in bimetallic catalyst system needs to be screened accordingly. Compared with 5K-10Ru/Fe catalyst, 5K-10Co/Fe catalyst presents better catalytic performance for catalyzing CO_2 conversion in this system, based on the reaction results.

Generally, CO_2 conversion was less than 40% under normal operation conditions [33, 37-39]. To further enhance the catalytic activity of CO_2 hydrogenation via ex situ water removal manner, a two-stage reactor system was developed and investigated, where the water product formed by RWGS reaction was trapped in the first ice-trap and the mixtures (including CO_2, CO, light hydrocarbons) sequentially entered the second reactor. The catalytic performance was listed in Table 1.6. According to the Table 1.6, it is disclosed that the CO_2 conversion is lower than the equilibrium conversion when using a single reactor. However, when using a two-stage reactor system, the catalytic conversion rate increases significantly from 36.5 to 64.2% (Table 1.6). More recently, Bordet et al. reported that water elimination accelerates the carbidization process, which is crucial for improving CO_2 hydrogenation activity [40]. Compared to the results from other literatures [20, 41-44], the two-stage reactor system exhibited a high CO_2 conversion while the selectivity of CO was low.

To further improve the yield of liquid fuel, we investigated the effect of W/F on conversion, selectivity, and STY. While the hydrocarbon and CO selectivities were not significantly changed, the CO_2 conversion was slightly increased from 64.2 to 65.1% if W/F decreased from 6.0 to 3.7 $g \cdot h \cdot mol^{-1}$. Especially, the yield of liquid fuel was enhanced sharply from 140.5 to 227.4 $g_{fuels}/kg_{cat} \cdot h$, greater than 1.6 times in the yield of liquid fuel. However, catalytic performance including activity and the yield of liquid fuel was deteriorated as the W/F value was lowered further. This indicates that the suitable flow velocity via regulating W/F value can significantly increase the yield of the liquid fuel

without increasing the undesired by-product (CO). However, increasing the yield of the liquid fuel by regulating W/F value is not particularly desirable for single reactor system. Different from the two-stage reactor system, the conversion of CO_2 decreased evidently while the selectivity of CO increased sharply with the decrease of W/F from 12.0 to 4.0 $g \cdot h \cdot mol^{-1}$, which was not particularly conducive to the formation of liquid fuel. As shown in the Table 1.6, increased flow velocity reduces the conversion of CO_2 and increases the selectivity of undesired CO by-product. But for the two-stage reactor system, the selectivity of by-product (CO) was not significantly boosted up while the catalytic activity was not significantly lowered with the increase of flow velocity. This illustrates that the regulation of W/F value is more suitable and powerful for the two-stage reactor system for enhancing the yield of liquid fuel than for single reactor system.

In order to investigate the influencing behavior of ex situ water removal, a similar two-stage reactor system without ex situ water removal was also adopted. As compared in Table 1.6, the conversion of CO_2 is significantly lower than that of a system with an ex situ water removal (24.6% vs. 65.1%). Furthermore, the selectivity of CO is 4 times more than that of a system with ex situ water removal. Therefore, the yield of liquid fuel increases from 70.2 to 227.4 $g_{fuels}/kg_{cat} \cdot h$, almost more three times if water is removed. When we compare two-stage reactor system without H_2O removal and 1 reactor system, we can find that the catalytic performance of CO_2 hydrogenation is slightly worse (Table 1.4). As for a two-stage reactor system without H_2O removal, the W/F over each reactor is a half of 1 reactor system owing to the same W/F value for these two systems. However, the decreased value of W/F has a negative effect on catalytic performance, as mentioned above. Thus, for a two-stage reactor system without water removal, the poor catalytic performance may be due to the negative impact of the flow rate on each reactor. Evidently,

ex situ water removal is of great significance in enhancing catalytic activity and reducing the selectivity of CO by-product. Although multi-stage temperature can be controlled to regulate the reaction parameters, the un-removed water vapor still affects the reaction performance. Moreover, this un-removed water vapor has a major negative effect on CO_2 hydrogenation, as shown in Table 1.6. Thus, it may not be ideal to achieve similar performance by controlling different heating zone in a single reactor without water removal. This effectively promotional effect derived from water removal facilitates CO_2 conversion, further enhances the yield of liquid fuel. It is worth mentioning that this tandem two-stage reaction system with an ex situ water removal is more powerful and economic than connected two reactors without water removal (Table 1.6). To some extent, this phenomenon provides an alternative route for industrial amplification applications of CO_2 hydrogenation, that is to say suitable tandem two-stage reaction system is better than connected two reactors without water removal from a perspective of economic benefit. Regarding the stability (Figure 1.9), the 5K-10Co/Fe catalyst presents a good stability in the CO_2 hydrogenation reactions during the time on stream (6 h).

In view of the obvious influence of reaction temperature on catalytic performance, we further investigated the influence of temperature, and the catalytic performance was listed in Table 1.7. According to Table 1.7, it is learnt that temperature is of positive significance to the improvement of catalytic activity. When the temperature rises from 270 to 330 ^oC, the conversion of CO_2 is improved from 39.0 to 69.9%, almost 1.8 times. Although the conversion of CO_2 is increased with the increase of temperature, the selectivity of CO as well as that of light hydrocarbons (C_1-C_4) does not increase, or even decrease. In addition, the selectivity of liquid fuel is also increased when reaction temperature reaches 330 ^oC. The enhancement of selectivity and activity promotes the

generation of liquid fuel. Consequently, the yield of liquid fuel is increased sharply from 128.1 to 326.2 $g_{fuels}/kg_{cat}·h$.

According to the above description, we can learn that the CO_2 hydrogenation performance can be significantly improved through a two-stage reaction system. To further investigate the impacts of number of reactors on the catalytic performance, each individual reactor performance was also examined and the results are listed in Table 1.8. Evidently different from the excellent performance over a two-stage reaction system, the CO_2 conversion is fairly low while the selectivity of CO is high over Reactor 1. However, the overall conversion of CO_2 is significantly higher than that from Reactor 1. Besides that, the selectivity of CO is fairly modest over a two-stage reaction system. As shown in Table 1.8, we can find that the selectivity of light hydrocarbons (C_1-C_4) increases while the selectivity of heavy hydrocarbons (C_{5+}) decreases. The phenomenon of poor catalytic performance may be resulted from the change of reaction gas composition. On the contrary, the utilization of second reactor did not promote the production of liquid products, but reduced the generation of CO by-product. Reactor 2 helped improving the conversion of CO_2 and CO to hydrocarbons. Thus, this result is a direct indication of the important role of the Reactor 2, which markedly promotes the conversion of CO_2 and CO intermediates. This advantage can be attributed to two aspects: ex situ water removal and CO intermediates further reaction via an FTS reaction. Ex situ water removal is conducive to the improvement of activity, while the further reaction of CO intermediates is beneficial for the decrease of by-product selectivity.

1.4. Conclusions

In summary, a simple precipitation and impregnation method is achieved to fabricate a bimetallic catalyst for improving CO_2 hydrogenation performance. We demonstrate that

Co metal as an effective dopant can enhance CO_2 hydrogenation reaction activity significantly. The enhanced performance for CO_2 hydrogenation is ascribed to the improvement of CO_2 adsorption and carbide content, i.e., a strengthening of interface reaction coupling of a tandem reaction including CO_2 activation and subsequent chain propagation reaction. The introduction of Co metal can increase the adsorption ability of CO_2, which is in favour of RWGS reaction on the surface of iron specials. Besides, Co dopant further promotes the carbonization process of iron species forming more carbides, which is beneficial for the chain propagation reaction. Therefore, the improvement of these two processes facilitates the whole process of CO_2 hydrogenation rather than a conventional one-way driving force. In addition, the yield of the target liquid fuel is obviously increased when a two-stage reactor system is employed. The enhanced catalytic performance is attributed to the powerful means of ex situ water removal. The ex situ water removal as well as further accelerated reaction of CO intermediates via a tandem system promotes CO_2 conversion, and makes the yield of liquid hydrocarbons exceeds 300 $g_{fuels}/(kg_{cat}h)$. Meanwhile, the utilization of a two-stage reactor system paves a new route for increasing the yield of renewable liquid hydrocarbons.

References

[1] H. Yang, C. Zhang, P. Gao, H. Wang, X. Li, L. Zhong, W. Wei, Y. Sun, Catal Sci Technol, 7 (2017) 4580-4598.

[2] W. Li, H. Wang, X. Jiang, J. Zhu, Z. Liu, X. Guo, C. Song, RSC Adv, 8 (2018) 7651-7669.

[3] M.D. Porosoff, B. Yan, J.G. Chen, Energy Environ Sci, 9 (2016) 62-73.

[4] J. Wei, Q. Ge, R. Yao, Z. Wen, C. Fang, L. Guo, H. Xu, J. Sun, Nat Commun, 8 (2017) 15174-15181.

[5] P. Gao, S. Li, X. Bu, S. Dang, Z. Liu, H. Wang, L. Zhong, M. Qiu, C. Yang, J. Cai, W. Wei, Y. Sun, Nat Chem, 9 (2017) 1019-1024.

[6] W.H. Wang, Y. Himeda, J.T. Muckerman, G.F. Manbeck, E. Fujita, Chem Rev, 115 (2015) 12936-12973.

[7] E.V. Kondratenko, G. Mul, J. Baltrusaitis, G.O. Larrazábalc, J. Pérez-Ramírez, Energy Environ Sci, 6 (2013) 3112-3135.

[8] X. Liu, M. Wang, C. Zhou, W. Zhou, K. Cheng, J. Kang, Q. Zhang, W. Deng, Y. Wang, Chem Commun, 54 (2018) 140-143.

[9] J. Dean, Y. Yang, N. Austin, G. Veser, G. Mpourmpakis, ChemSusChem, 11 (2018) 1169-1178.

[10] J. Zhang, S. Lu, X. Su, S. Fan, Q. Ma, T. Zhao, J CO2 Util, 12 (2015) 95-100.

[11] J. Wei, J. Sun, Z. Wen, C. Fang, Q. Ge, H. Xu, Catal Sci Technol, 6 (2016) 4786-4793.

[12] M. Amoyal, R. Vidruk-Nehemya, M.V. Landau, M. Herskowitz, J Catal, 348 (2017) 29-39.

[13] L. Guo, J. Sun, X. Ji, J. Wei, Z. Wen, R. Yao, H. Xu, Q. Ge, Commun Chem, 1 (2018)

11.

[14] U. Rodemerck, M. Holeña, E. Wagner, Q. Smejkal, A. Barkschat, M. Baerns, 5 (2013) 1948-1955.

[15] P. Kangvansuraa, L.M. Chewb, W. Saengsuic, P. Santawajad, Y. Poo-arporne, M. Muhlerb, H. Schulzf, A. Worayingyong, Catal Today, 275 (2016) 59-65.

[16] N. Fischer, R. Henkel, B. Hettel, M. Iglesias, G. Schaub, M. Claeys, Catal Lett, 146 (2016) 509-517.

[17] R.W. Dorner, D.R. Hardy, F.W. Williams, H.D. Willauer, Appl Catal A-Gen, 373 (2010) 112-121.

[18] T. Li, Y. Yang, C. Zhang, X. An, H. Wan, Z. Tao, H. Xiang, Y. Li, F. Yi, B. Xu, Fuel, 86 (2007) 921-928.

[19] Y.H. Choi, Y.J. Jang, H. Park, W.Y. Kim, Y.H. Lee, S.H. Choi, J.S. Lee, Appl Catal B-Environ, 202 (2017) 605-610.

[20] Y.H. Choi, E.C. Ra, E.H. Kim, K.Y. Kim, Y.J. Jang, K.-N. Kang, S.H. Choi, J.-H. Jang, J.S. Lee, ChemSusChem, 10 (2017) 4764 -4770.

[21] S. Geng, F. Jiang, Y. Xu, X. Liu, ChemCatChem, 8 (2016) 1303-1307.

[22] R. Satthawong, N. Koizumi, C. Song, P. Prasassarakich, Catal Today, 251 (2015) 34-40.

[23] R. Satthawong, N. Koizumi, C. Song, P. Prasassarakich, J CO2 Util, 3-4 (2013) 102-106.

[24] M.K. Gnanamani, G. Jacobs, H.H. Hamdeh, W.D. Shafer, F. Liu, S.D. Hopps, G.A. Thomas, B.H. Davis, ACS Catal, 6 (2016) 913-927.

[25] W. Li, A. Zhang, X. Jiang, M.J. Janik, J. Qiu, Z. Liu, X. Guo, C. Song, J CO2 Util, 23 (2018) 219-225.

[26] G. Chen, R. Gao, Y. Zhao, Z. Li, G.I.N. Waterhouse, R. Shi, J. Zhao, M. Zhang, L. Shang, G. Sheng, X. Zhang, X. Wen, L.Z. Wu, C.H. Tung, T. Zhang, Adv Mater, 30 (2018), 1704663.

[27] F. Jiang, B. Liu, S. Geng, Y. Xu, X. Liu, Catal Sci Technol, 8 (2018), 4097–4107.

[28] R. Satthawong, N. Koizumi, C. Song, P. Prasassarakich, Top Catal, 57 (2013) 588-594.

[29] T. Ishihara, K. Eguchi, H. Arai, Appl Catal, 30 (1987) 225-238.

[30] M.V. Landau, R. Vidruk, M. Herskowitz, ChemSusChem, 7 (2014) 785-794.

[31] K.L. Luska, A. Bordet, S. Tricard, I. Sinev, W. Grüert, B. Chaudret, W. Leitner, ACS Catal, 6 (2016) 3719-3726.

[32] M.I. Qadir, A. Weilhard, J.A. Fernandes, I.d. Pedro, B.J.C. Vieira, J.C. Waerenborgh, J. Dupont, ACS Catal, 8 (2018) 1621-1627.

[33] C.G. Visconti, M. Martinelli, L. Falbo, L. Fratalocchi, L. Lietti, Catal Today, 277 (2016) 161-170.

[34] J. Sun, H. Xu, G. Liu, P. Zhu, R. Fan, Y. Yoneyama, N. Tsubaki, ChemCatChem, 7 (2015) 1642-1645.

[35] C.-W. Tang, C.-B. Wang, S.-H. Chien, Thermochim Acta, 473 (2008) 68-73.

[36] H.-Y. Chen, W.M.H. Sachtler, Catal Today, 42 (1998) 73-83.

[37] C. Xie, C. Chen, Y. Yu, J. Su, Y. Li, G.A. Somorjai, P. Yang, Nano Lett, 17 (2017) 3798-3802.

[38] Z. Li, J. Wang, Y. Qu, H. Liu, C. Tang, S. Miao, Z. Feng, H. An, C. Li, ACS Catal, 7 (2017) 8544-8548.

[39] P. Gao, S. Dang, S. Li, X. Bu, Z. Liu, M. Qiu, C. Yang, H. Wang, L. Zhong, Y. Han, Q. Liu, W. Wei, Y. Sun, ACS Catal, 8 (2017) 571-578.

[40] A. Bordet, J.M. Asensio, K. Soulantica, B. Chaudret, ChemCatChem, (2018).

[41] T. Xie, J. Wang, F. Ding, A. Zhang, W. Li, X. Guo, C. Song, J CO2 Util, 19 (2017) 202-208.

[42] C.G. Visconti, M. Martinelli, L. Falbo, A. Infantes-Molina, L. Lietti, P. Forzatti, G. Iaquaniello, E. Palo, B. Picutti, F. Brignoli, Appl Catal B-Environ, 200 (2017) 530-542.

[43] M. Albrecht, U. Rodemerck, M. Schneider, M. Bröring, D. Baabe, E.V. Kondratenko, Appl Catal B-Environ, 204 (2017) 119-126.

[44] R.E. Owen, P. Plucinski, D. Mattia, L. Torrente-Murciano, V.P. Ting, M.D. Jones, J CO2 Util, 16 (2016) 97-103.

[45] C. Yang, B. Zhao, R. Gao, S.Y. Yao, P. Zhai, S.W. Li, J. Yu, Y.L. Hou, D. Ma, ACS Catal 7 (2017) 5661-5667

Table 1.1 Weight percentage of K/Fe and Co/Fe based on various technical results.

Catalysts	SEM-EDS results (%)		XRF results (%)	
	K/Fe	Co/Fe	K/Fe	Co/Fe
Fe	0	0	0	0
5K-Fe	4.8	0	4.8	0
5K-10Co/Fe	5.6	11.7	6.3	11.1

Table 1.2 Surface area and pore volume of 5K-Fe, 5K-10Co/Fe and 5K-10Ru/Fe.

Catalysts	BET surface area (m^2/g)	Pore volume (cm^3/g)
5K-Fe	12.9	0.000562
5K-10Co/Fe	10.8	0.000312
5K-10Ru/Fe	11.7	0.000340

Table 1.3 Carbide content on spent catalyst surface is derived from Fe2p analysis.

Catalysts	Carbide content (Fe-C, mol %) in catalyst surface
Fe	3.6
5K-Fe	7.9
5K-10Co/Fe	18.0
5K-10Ru/Fe	5.3

Table 1.4 CO_2 hydrogenation performances over different Fe-based catalysts.

Catalyst	Number of reactors	Conv. / %	CO Sel./%	Hydrocarbon Sel. / %		
				CH_4	C_2-C_4	C_{5+}
Fe	1	16.8	44.0	34.3	48.3	17.5
5K-Fe	1	23.3	30.2	15.9	34.0	50.1
5K-10Co/Fe	1	29.4	15.7	13.2	36.3	50.5
5K-10Ru/Fe	1	23.4	22.5	26.4	28.6	45.0

Reaction conditions: 12 g h mol^{-1}, 300 ^oC, 1.0 MPa. H_2/CO_2=2.65.

Table 1.5 FTS performance of 5K-10Co/Fe and 5K-10Ru/Fe after 6h on stream.

Entry	Catalyst	Conv. / %	CO_2 Sel. (%)	Hydrocarbon Sel. / %		
				CH_4	C_2-C_4	C_{5+}
1	5K-10Co/Fe	65.8	46.9	14.6	32.1	53.3
2	5K-10Ru/Fe	97.8	35.0	13.7	31.8	54.5

Reaction conditions: CO: 31.4 v%, H_2: 64.5 v%, Ar: 4.1 v%, 300 ^oC, 1.0 MPa, W/F = 10 g h mol^{-1}.

Table 1.6 CO_2 hydrogenation performance over a single or tandem catalytic system.

Catalyst	Number of reactors	W/F/ ($g \cdot h \cdot mol^{-1}$)	Conv. / %	CO Sel./%	Selectivity / %			STY /
					CH_4	C_2-C_4	C_{5+}	C_{5+}
K-Co/Fe	1	12.0	40.4	7.1	20.7	38.4	40.9	42.6
K-Co/Fe	1	6.0	36.5	11.6	17.7	46.3	36.0	64.4
K-Co/Fe	1	4.0	31.6	17.4	16.2	47.8	35.9	78.0
K-Co/Fe	2	6.0	64.2	3.3	17.0	42.2	40.8	140.5
K-Co/Fe	2	3.7	65.1	3.3	21.0	40.4	38.5	227.4
K-Co/Fe	2	3.0	52.7	5.9	17.3	46.3	36.4	215.9
K-Co/Fe[a]	2	3.7	24.6	15.1	19.9	44.3	35.8	70.2

Reaction conditions: 300 °C, 3.0 MPa, H_2/CO_2 =2.93; [a], a similar two-stage reactor system without ex situ water removal.

Table 1.7 CO_2 hydrogenation performance under different reaction temperature.

Catalyst	Number of reactors	T/ °C	Conv. / %	CO Sel./%	Selectivity / %			STY / $g_{fuels}/(kg_{cat}\cdot h)$
					CH_4	C_2-C_4	C_{5+}	C_{5+}
5K-10Co/Fe	2	270	39.0	8.6	17.7	43.9	38.4	128.1
5K-10Co/Fe	2	300	65.1	3.3	21.0	40.4	38.5	227.4
5K-10Co/Fe	2	330	69.9	3.2	16.7	31.8	51.5	326.2

Reaction conditions: 3.7 g h mol^{-1}, 3.0 MPa, H_2/CO_2 =2.93.

Table 1.8 CO_2 hydrogenation performance over each individual reactor.

Catalyst	Order number	Conv. / %	CO Sel./%	Selectivity / %			STY / $g_{fuels}/kg_{cat}\cdot h$)
				CH_4	C_2-C_4	C_{5+}	C_{5+}
5K-10Co/Fe (I)	Reactor 1	24.6	21.9	14.6	45.0	40.4	145.3
5K-10Co/Fe[a] (II)	Reactor 2	/	/	31.0	33.3	35.6	82.1
5K-10Co/Fe (III)	Overall	65.1	3.3	21.0	40.4	38.5	227.4

Reaction conditions: 3.7 g h mol^{-1}, 300 ºC, 3.0 MPa, H_2/CO_2 =2.93; [a], data calculated based on hydrocarbon balance (II=III-I).

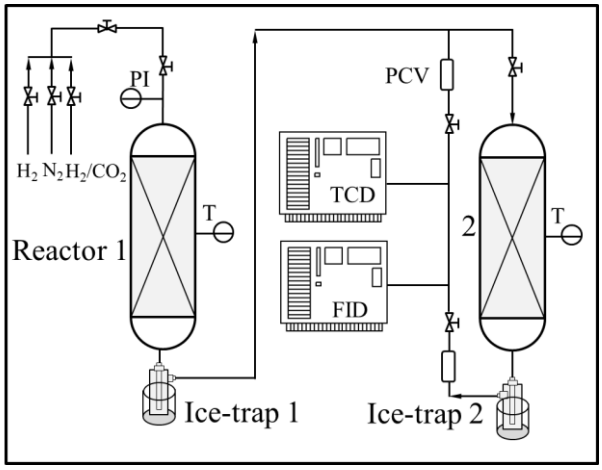

Scheme 1.1 Two-stage reactor system for catalyzing CO_2 hydrogenation.

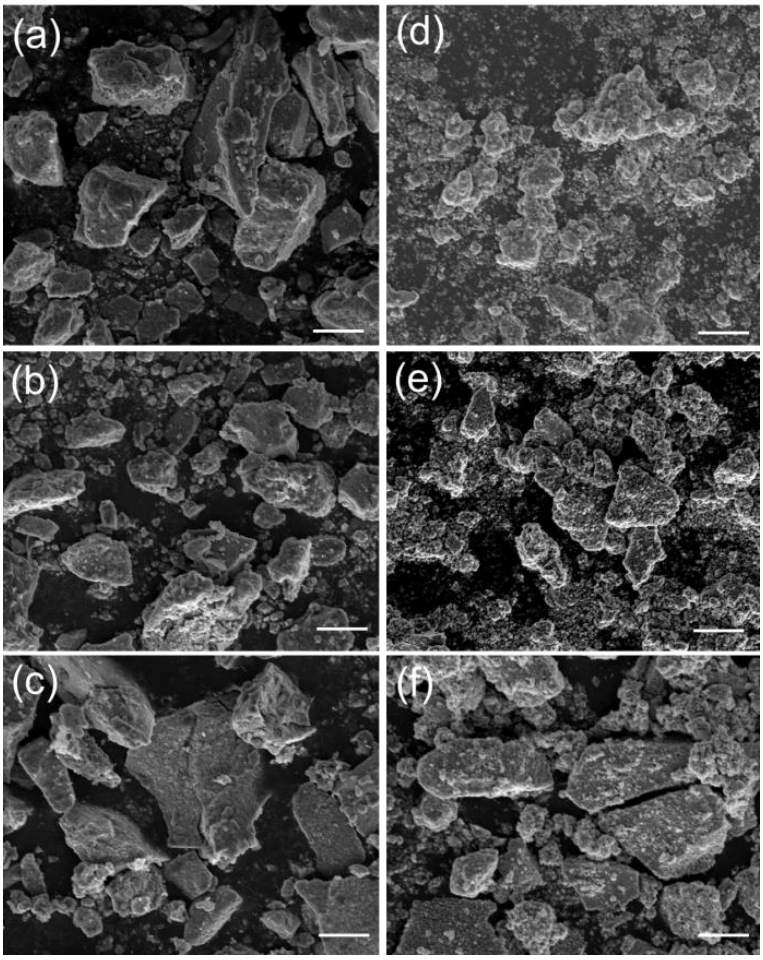

Figure 1.1 SEM images of (a) as-prepared 5K-Fe; (b) as-prepared 5K-10Co/Fe; (c) as-prepared 5K-10Ru/Fe catalysts; (d) spent 5K-Fe; (e) spent 5K-10Co/Fe; (f) spent 5K-10Ru/Fe catalysts. (The length of the scale bar in panels a-f, represents 10 μm)

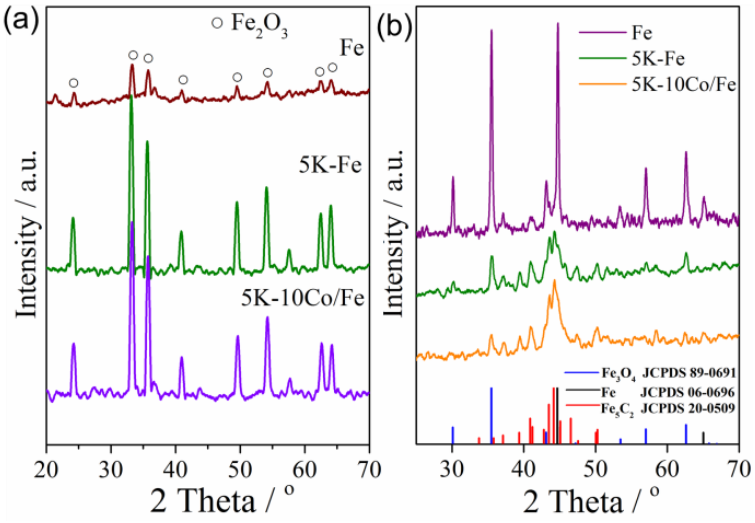

Figure 1.2 XRD patterns of (a) as-prepared Fe, 5K-Fe and 5K-10Co/Fe catalysts, (b) spent Fe, 5K-Fe and 5K-10Co/Fe catalysts.

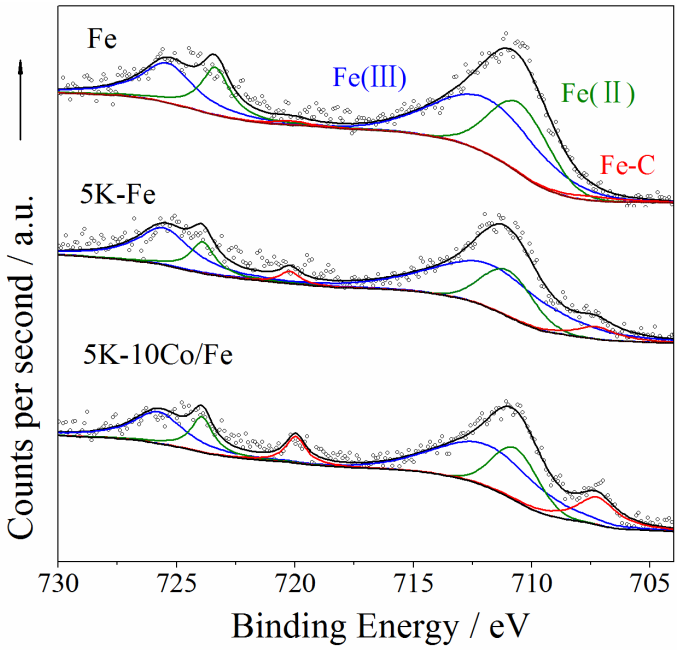

Figure 1.3 XPS spectra of the Fe2p levels of spent Fe, 5K-Fe, and 5K-10Co/Fe catalysts.

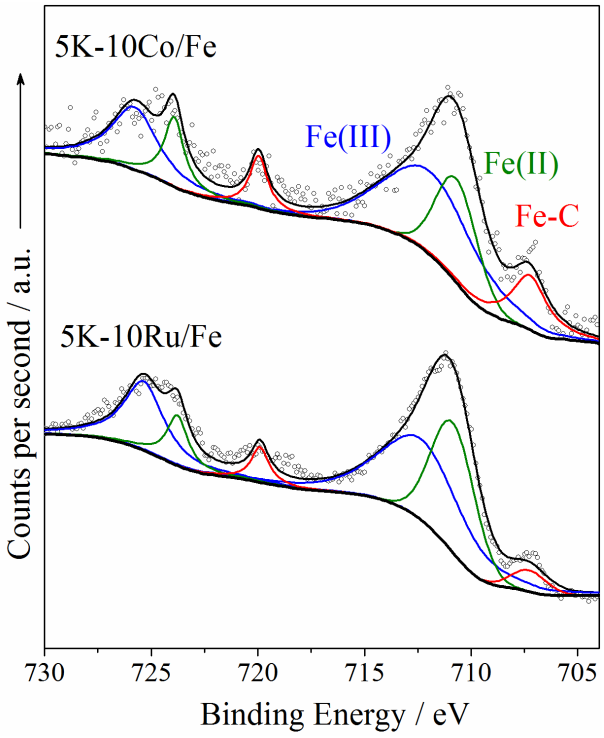

Figure 1.4 XPS spectra of the Fe2p levels of spent 5K-10Co/Fe and 5K-10Ru/Fe catalysts.

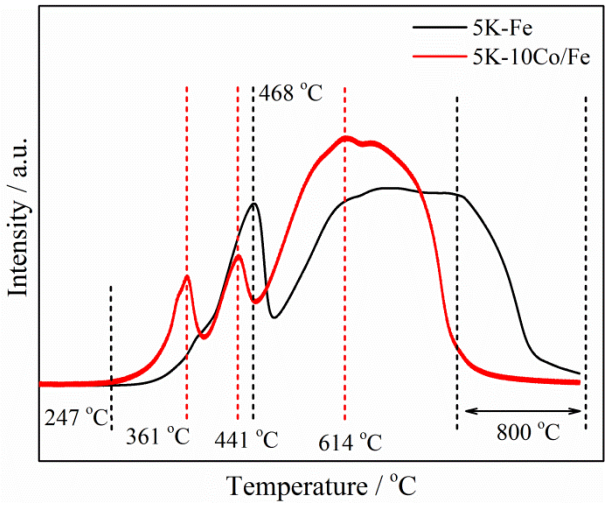

Figure 1.5 H_2-TPR profiles of as-prepared 5K-Fe and 5K-10Co/Fe catalysts.

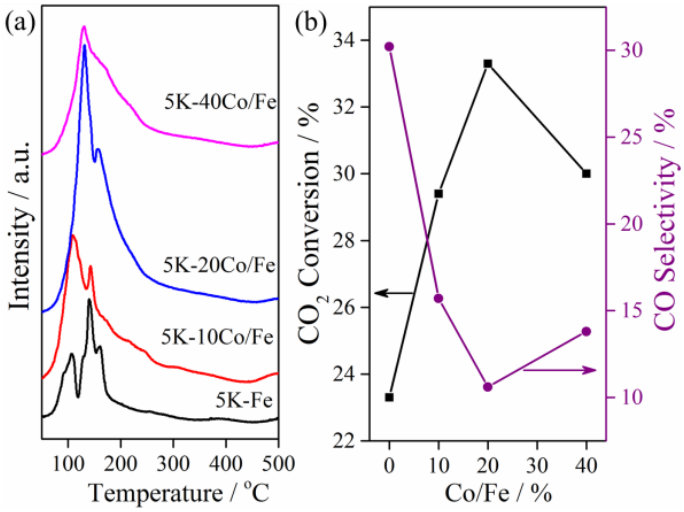

Figure 1.6 (a) CO_2-TPD profiles of as-prepared 5K-Fe, and 5K-Co/Fe with different Co/Fe mass ratio, (b) the effect of Co/Fe mass ratio on the catalytic performance.

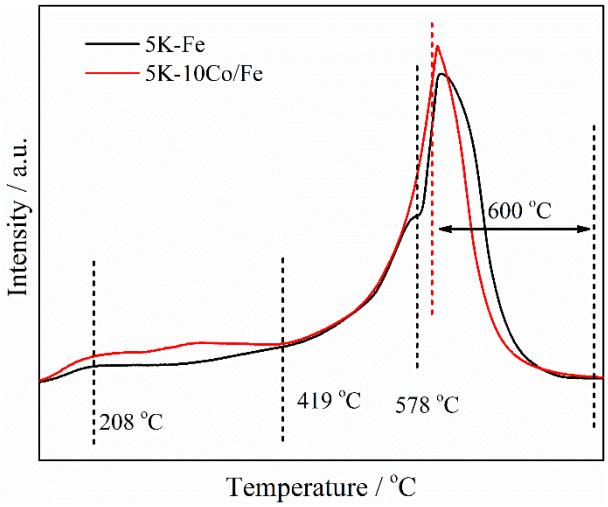

Figure 1.7 CO-TPD profiles of as-prepared 5K-Fe and 5K-10Co/Fe catalysts.

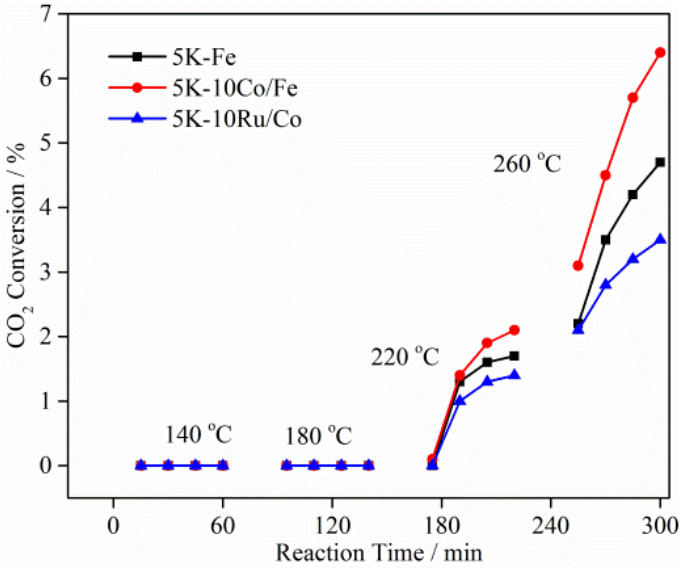

Figure 1.8 Platform reaction performances of 5K-Fe, 5K-10Co/Fe and 5K-10Ru/Fe under different temperatures. After reduction, the catalysts reacted in feed gas at 140 °C for 60 min. Then the temperature rised to 180 °C and reacted for 60 minutes. Same operations repeated for 220 °C and 260 °C stage reaction.

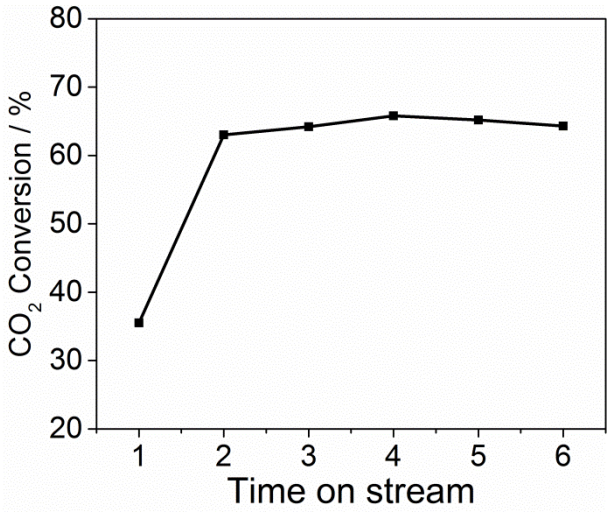

Figure 1.9 Time on stream CO_2 conversion of 5K-10Co/Fe over a two-stage reactor.

Chapter 2

One-Pot Hydrothermal Synthesis of Nitrogen Functionalized Carbonaceous Material Catalysts with Embedded Iron Nanoparticles for CO_2 Hydrogenation

A facile fabrication, rather than conventional post-treatment processing, of nitrogen functionalized carbon supported iron catalysts as efficient metal promoter-free CO_2 hydrogenation catalysts.

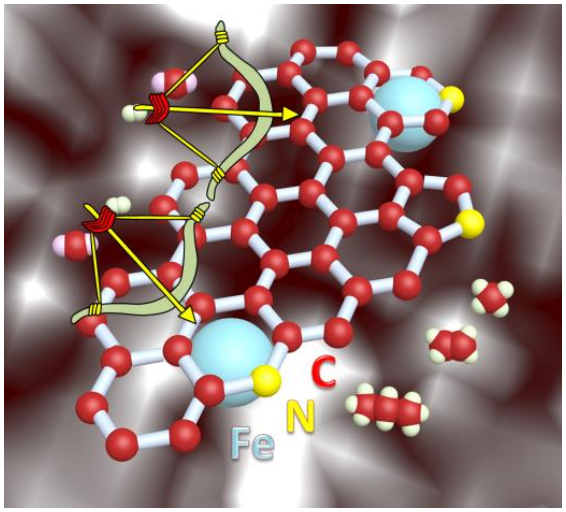

Abstract

Nitrogen functionalized carbon with embedded iron nanoparticles was developed by a simple one-pot hydrothermal synthesis process. Different nitrogen atom sources can obviously affect the morphologies, structures and surface properties of the formed functionalized catalysts through a one-pot hydrothermal self-assembly process. Among these processes, the introduction of nitrogen atom from pyrrolidine can promote the improvement of CO_2 hydrogenation activity while lower the selectivity of undesired CO by-product. Different from pyrrolidine introduction, although the addition of three other nitrogenous reagents (ethylenediamine, pyridine, and diethylformamide) changed the physicochemical properties of the catalysts, the catalytic performance was not improved significantly. The improved CO_2 hydrogenation performance over these functionalized catalysts was found to be correlated with the specific surface areas, the carbonization degree of iron species precursor, the amount of defect sites, and the content of pyridine-like nitrogen structures, which are determined by the doping nitrogen atom types. Furthermore, the one-step utilization of nitrogenous reagent as carbon sources also, besides nitrogen source, did not show a benign performance for catalyzing CO_2 hydrogenation, indicating the importance of synergistic self-assembly process derived from carbonization process of pyrrolidine and glucose.

Keywords: CO_2 hydrogenation, Hydrothermal self-assembly, Carbon materials, Iron catalysts, Nitrogen functionalization

2.1. Introduction

Considering the gradual consumption of nonrenewable petroleum resources and the prominence of environmental issues, catalytic conversion of CO_2 and H_2 to commodity chemicals or fuels is a promising route to mitigate this challenge, which not only stores energy but also reduces environmental stress [1-5]. In these catalytic processes, iron-based catalysts, bimetallic catalysts, and composite catalysts have been widely used for the production of valuable chemicals such as olefins, fuels, aromatics, and oxygenated chemicals [6-19]. Unlike other metals, iron has a high reverse water-gas shift (RWGS) activity, apart from cheap and easy to obtain, which makes it more promising for catalyzing CO_2 hydrogenation via a modified Fischer-Tropsch synthesis (FTS) process [20].

Generally, support materials play a crucial role in the dispersion and stabilization of active sites during the reaction process. The conventional support materials for iron-based catalysts include SiO_2, TiO_2, Al_2O_3, and zeolite [21-24]. Although these common support materials possess benign physicochemical properties, such as a high ability for stabilizing active sites and a high surface area for dispersing active sites, the strong metal-support interaction (SMSI) usually led to the difficult reduction and carburization of iron species, even the formation of hardly reducible complex compounds [25-27]. Apart from oxide materials, carbon materials (carbon sphere, well-defined mesoporous carbon, carbon nanotube, graphene etc.) have also been widely used for catalysis reaction in the past decades due to well tunable properties [28-30]. Likewise, these carbon materials have also been the hot research topic and broad applications in sensing, energy conversion and storage, adsorption, etc [31-34]. Weak interactions between carbon supports and metal oxides and a favorable carbon environmental factor are in favor of the reduction and

carbonization process of iron species, which promote the improvement of catalytic performance.

It is well recognized that metal promoters, as the electron donors, can improve the catalytic activity and selectivity by affecting the electron distribution state of active sites. Previous research indicates that the doping of alkali metal (K, Na, Mg, etc.) promotes the formation of higher hydrocarbons and suppresses the CH_4 and CO by-product selectivity [10, 14, 35]. In addition, nitrogen doping as promoter-like doping can also well regulate the surface properties of carbon materials, such as surface basicity, electric conductivity, and electron-donor affinity via electron donor or anchor of active sites [25, 36, 37]. Thus, these nitrogen-containing carbon materials as potential supports have broad and promising prospects in heterogeneous catalysis. Recently, Liu et al. reported that strong basicity derived from nitrogen-containing groups could effectively promote the formation of light olefins while suppress methane selectivity during FTS process [25]. Hendrik et al. found that nitrogen-containing functional groups act as efficient anchoring sites for iron nanoparticles, and this nitrogen functionalized groups led to a high intrinsic activity [38]. Similarly, Martin et al. also demonstrated that the presence of nitrogen groups is beneficial to the improvement of activity [20]. Chew et al. reported that iron oxide nanoparticles on N-doped carbon nanotubes (CNTs) were easier to reduction than O-functionalized one and silica supported one, and N-functionalized one achieved a higher olefin selectivity [39]. The N-doped CNTs were even treated with nitric acid to further improve FTS performance [40]. Owing to the high selectivity of undesired CH_4 (approaching 66%) over N-functionalized CNTs, Praewpilin et al. improved the catalytic performance through further Mn and K promoter doping [41]. It is worth noting that most nitrogen-doped carbon materials are prepared by post-treatment processing, such as

calcination in ammonia atmosphere [20, 39, 41-43]. Although carbon materials with nitrogen incorporation have been widely used in CO hydrogenation [20, 25, 38, 40], few related reports concerning it for CO_2 hydrogenation exist [39, 41].

Herein, we report a facile fabrication of nitrogen functionalized carbon supported iron catalysts as efficient metal promoter-free CO_2 hydrogenation catalysts, rather than a conventional post-treatment processing. Functionalized nitrogen-containing groups were directionally introduced into carbon supports through one-pot hydrothermal self-assembly. The effects of different nitrogenous reagents on the structure and properties of carbon supports were studied. CO_2 hydrogenation performances over these nitrogen functionalized carbon supported iron catalysts were also investigated and discussed in detail.

2.2. Experimental

2.2.1 Catalyst Preparation

First, glucose and iron nitrate were dissolved in deionized water. After stirring for two hours, the obtained liquid was transferred into a Teflon-lined stainless-steel autoclave, followed by one-pot hydrothermal synthesis at 150 °C for 24 h. Obtained products were filtered and washed several times with distilled water and ethanol successively. Finally, products were dried in drying oven at 120 °C overnight, marked as Fe/C. As for these nitrogen functionalized Fe/C catalysts, pyrrolidine (PYL, 5.0g), ethylenediamine (EDA, 2.1g), diethylformamide (DFM, 7.1g), and pyridine (PYD, 5.6g) as nitrogen sources were added into an aqueous solution containing glucose and iron nitrate, respectively. Thereinto, each added nitrogenous reagent had the same molar nitrogen content (0.07 mol). The next steps were similar to the preparation of Fe/C catalyst. Finally, the obtained

products were denoted as Fe/C-PYL, Fe/C-EDA, Fe/C-DFM, and Fe/C-PYD, respectively. Besides, PYL acting as a carbon and nitrogen source simultaneously was also used to fabricate a catalyst, and the corresponding product was marked as Fe-PYL.

2.2.2 Catalyst characterization

Scanning electron microscopy (SEM) images were taken by a JEOL JSM-6360LV microscope operated at an accelerating voltage of 10 kV. High-resolution transmission electron microscopy (HRTEM) for spent catalysts was obtained by a Tecnai G2 F30 at 300kV. N_2 physisorption was performed on a Micromeritics analyzer. Before sample analysis, the catalysts were vacuum dried at 120 ºC for 6h. XRD spectra of the powder catalysts were recorded by a Rigaku RINT 2400 X-ray Diffractometer using Cu-Ka (40 kV, 40 mA) irradiation. Scans were recorded in the 2θ range of 5-90º with a step size of 0.02 º/s. Raman spectroscopy measurements were taken by an inVia Basis 532LE Raman spectroscopy. The X-ray photoelectron spectroscopy (XPS) analysis was conducted on Thermo Fisher Scientific ESCALAB 250Xi multifunctional X-ray photoelectron spectroscope. The adsorption and reduction properties of the as-prepared catalysts were determined by a BELCAT-II-T-SP Characterization System.

2.2.3 Catalytic performance test

CO_2 hydrogenation performances over these as-prepared catalysts were conducted in a fixed-bed stainless steel reactor (6.0 mm inner diameter). Before reaction, the as-prepared catalysts (0.5 g) were in situ reduced at 380 ºC for 8 h in a pure H_2 flow (40 ml min^{-1}). After reduction, the temperature was dropped to 300 ºC. Subsequently, the reactant gas of $CO_2/H_2/Ar$ (24.5 vol% / 71.8 vol% / 3.7 vol%) was fed into the reactor, and the system was pressured gradually to 1.0 MPa. N-octane as solvent was equipped to capture

the liquid hydrocarbons in the effluents. The obtained liquid hydrocarbons were analyzed by an off-line gas chromatograph using a flame ionization detector. CO_2 conversion, CO selectivity, and hydrocarbons selectivity were calculated according to equation (1), (2), and (3), respectively.

$$CO_{2\ conversion\ (\%)} = (CO_{2\ in}\text{-}CO_{2\ out})/CO_{2\ in} \times 100\% \quad (1)$$

CO_2 in: mole fraction of CO_2 in the inlet, CO_2 out: mole fraction of CO_2 in the outlet.

$$CO_{selectivity\ (\%)} = CO_{out}/ (CO_{2\ in}\text{-}CO_{2\ out}) \times 100\% \quad (2)$$

CO out: mole fraction of CO in the outlet.

$$C_{i\ hydrocarbon\ selectivity\ (C\text{-}mol\ \%)} = \text{Mole of } C_{i\ hydrocarbons} / \text{Mole of total hydrocarbon} \times 100\% \quad (3)$$

2.3. Results and discussion

2.3.1 Structure and surface properties of catalysts

Scanning electron microscopy (SEM) was carried out to reveal the morphologies and structures of the nitrogen functionalized carbon supported iron catalysts, as shown in Figure 2.1. As for Fe/C without nitrogen doping, the main morphological structure is spherical structure. Although such types of carbonaceous microspheres embedded with iron species nanoparticles were fabricated by hydrothermal treatment of a glucose and iron nitrate solution [44], nitrogen incorporation for the Fe/C catalysts through the hydrothermal process is rarely reported to catalyze CO_2 hydrogenation.

As shown, the introduction of different nitrogen source has a profound influence on the apparent morphology and structure of generated carbon materials during hydrothermal synthesis process. The dimensions of the spherical structure without N doping are mainly between 8 and 12 μm. When the nitrogen source of PYL was introduced, the carbon materials present the state of smooth pellet cementation. Obviously, the dispersibility of the carbon supports reduces with the addition of PYL. Different from

the utilization of PYL, carbon support presents coarse and irregular granules with the addition of EDA. Although the introduction of DFM reagent did not change the spherical structure of the support materials, the dimensions of the spherical structure were increased significantly which was mainly between 9 and 15 μm. Even if the morphology of the carbon support changed little with the utilization of PYD, the size of carbon spheres has decreased. From SEM micrographs, it is obvious that the original state of nitrogen source can affect the carbonation process of glucose, and thus shows different morphologies and structures.

Chain propagation is a structure-sensitive reaction, and the particle size has a profound influence on the activity and selectivity of hydrocarbons product especially for small-size particles [45, 46]. Previously, Xiong et al. attributed the improved chain propagation ability to the Fe crystallite size effect, where smaller carbide particles (from 5-30 nm) presented a higher C-C coupling activity [47, 48]. Similar phenomena have been proposed by other researchers (< 10 nm) [46]. Therefore, to investigate the size effect, the particle sizes of these spent catalysts are also compared in Figure 2.2. As can be observed, there is a significant difference in particle size, and the difference will affect the catalytic performance. According to statistical results obtained from HRTEM images (Figure 2.2), the order of these iron species is Fe/PYL (6-8 nm) < Fe/C-PYD, Fe/C (8-12 nm) < Fe/C-EDA (10-14 nm) < Fe/C-DFM (19-23 nm). Obviously, the distribution of particle sizes is affected by nitrogenous reagents. Thus, the introduction of PYL reagent contributed to the generation of small particles, which well be crucial for improving catalytic activity.

N_2 physisorption measurement was applied to investigate the structure of reference Fe/C and functionalized Fe/C catalysts (Figure 2.3). The detailed results are summarized in Table 2.1. As can be seen, the differences in surface area and average diameter are

obvious due to nitrogen incorporation. All of these catalysts have low surface area, which indicate that these supports are not very nonporous [48]. Among these nitrogenous reagents, the introduction of PYL or PYD can significantly increase the surface area of carbon supports during hydrothermal process, which is of importance for the dispersion of active species. Besides that, the average diameters of carbonaceous microstructures also agree well with surface areas (Table 2.1).

To investigate the phase composition of as-prepared and spent catalysts, X-ray diffraction (XRD) characterizations were used (Figure 2.4). The as-prepared Fe/C catalyst exhibits a typical phase of humboldtine ($FeC_2O_4{\cdot}2H_2O$, JCPDS 23-0293), as reported previously [29, 49]. In terms of Fe/C-DFM and Fe/C-PYD, the corresponding diffraction peaks are weak indicating the uniform distribution of particles or fine particle sizes. Different from the three catalysts above (Fe/C, Fe/C-DFM, and Fe/C-PYD), the main phase is iron oxides (Fe_2O_3, JCPDS 89-0596) for Fe/C-PYL and Fe/C-EDA. According to XRD results, it can be deduced that the introduction of different nitrogenous reagents can affect the formation of iron species precursor.

As for the spent catalyst (Figure 2.5), Fe/C consists of iron oxides (Fe_3O_4, JCPDS 89-0691) and iron carbides (Fe_5C_2, 20-0509) [10]. Fe/C-PYL and Fe/C-EDA have the same composition as spent Fe/C. The diffraction peaks of the metal Fe (JCPDS 23-0293) for the other two catalysts (Fe/C-DFM and Fe/C-PYD) were visibly strong while the carbides peaks were weak. Notably, although the iron species precursor is different, spent Fe/C-PYD and Fe/C-EDA contain the same phases as Fe/C catalyst. However, the same iron species precursor also leads to the differences in diffraction peaks (Fe/C, Fe/C-DFM, and Fe/C-PYD). It is indicated that the precursor influenced by nitrogenous reagents has little effect on final active phases. Therefore, the differences in diffraction peaks originate

from nitrogen incorporation instead of precursor difference. It is intuitively disclosed that the functionalization process derived from DFM and PYD modification, is not conducive to the carbonization of iron species under reaction conditions (Figure 2.5).

The differences in the structure of as-prepared and spent iron catalysts were assessed by Raman spectroscopy. In terms of the Raman spectra of different iron catalysts, two bands can be clearly seen at around 1590 and 1330 cm^{-1}, which can be attributed to the G band and the D band, respectively (Figure 2.6) [48]. Generally the intensity of D band is a feature for disordered graphite (including defects and sp3-hybridized carbon atoms) while the intensity of G band is relative to the growth of graphitic carbon, then the relative intensity (I_D/I_G) of D band and the G band can reflect the defect sites or graphitization degree [47, 48, 50]. These Raman peaks were further deconvoluted and compared in Table 2.2. For these as-prepared catalysts, the degrees of disordered graphite are increased with the introduction of nitrogenous reagent except for EDA, which indicates that N incorporation is a useful tool to enhance the amount of defect sites. However, significant differences in the intensity of I_D/I_G can be observed after CO_2 hydrogenation reaction. Different from these of Fe/C-PYL, Fe/C-EDA, and Fe/C-DFM, the intensity of I_D/I_G is significantly increased for Fe/C and Fe/C-PYD catalysts especially for Fe/C-PYD. The increases in I_D/I_G intensity are more likely derived from the structural damages rather than structural modification by nitrogenous reagent, which directly indicates the instability of the microstructure of the catalyst.

In order to explore the effect of nitrogen functionalization on the surface properties, the reduction degrees (H_2-TPR) of different as-prepared nitrogen functionalized catalysts based on hydrogen consumption values are compared (Figure 2.7). In addition to Fe/C-PYL catalysts, the first broad peak around 200-500 ^oC can be assigned to the reduction

process of iron oxide species to metallic Fe (Fe_2O_3 to Fe_3O_4, and Fe_3O_4 to Fe) [47]. And there are two obviously inverted peaks between 500-900 ^oC, which can be attributed to the degradation of carbonaceous species or carbon gasification at high temperature [47, 51]. As for Fe/C-PYL catalyst, a differentiable premature peak (at around 347 ^oC) arises compared to Fe/C, which indicates the nitrogen incorporation from PYL addition promotes the reduction of iron species. As opposed to Fe/C, the promotional effects of the other three kinds of nitrogen functional catalysts (Fe/C-EDA, Fe/C-DFM and Fe/C-PYD) are not obvious.

Meanwhile, the adsorption properties of CO_2 were also investigated. According to Figure 2.8, we can learn that there is a weak peak between 100 and 200 ^oC, which can be attributed to physical adsorption peaks of CO_2. The peaks between 350 and 550 ^oC can be assigned to chemisorbed peaks. However, the peaks between 550 and 800 ^oC are due to the degradation of carbonaceous materials. Compared with reference Fe/C, the adsorption intensity of CO_2 increases a lot with the introduction of other four nitrogenous reagents but expect PYD. For Fe/C-PYD, we speculate that it is possible that a small number of nitrogenous sites could be used to anchor the iron species or were contained within the carbon materials, thus showing a poor adsorption performance (Table 2.3, Figure 2.8). In terms of other three functionalized catalysts with a higher content of nitrogenous groups (Table 2.3), the enhancement of alkalinity significantly promoted the adsorption of CO_2.

It is well known that the surface composition of the catalyst has an important effect on the reaction performance [10]. To further investigate and compare the surface states of these catalysts, X-ray photoelectron spectroscopy (XPS) analysis was used. The survey scan spectra of different Fe-based catalysts were compared in Figure 2.9. From scan

spectra, it was found that although each nitrogenous reagent could introduce nitrogen atoms into the supports, there was a significant difference in the intensity of nitrogen atom on the surface of catalysts. To some extent, the results have clearly shown that the coupling strength of nitrogen atoms from different nitrogen reagents and carbon atoms from glucose, is obviously different during carbonization process. Generally, the formation of these carbon materials involves a series of complex processes such as dehydration, condensation, polymerization and aromatization [52, 53]. The introduction of nitrogenous reagent influences these processes through the different existence manner of nitrogenous functional groups, which in turn affects the morphology and structure of the catalyst.

Elemental compositions of nitrogen functionalized iron catalysts were explored by XPS measurements, and summarized in Table 2.3. It is clear that different nitrogen reagents have introduced varied amounts of nitrogen atoms. At least till now post-treatment such as nitric acid vapor treatment or calcination under NH_3 atmosphere is the common nitrogen doping treatment method [20, 39, 41], but the surface nitrogen content of these catalysts is less than 5 at.% [20, 39]. In contrast, one-step method employed here is more advantageous as it simplifies the preparation process of catalyst, lowering the catalyst preparation cost. In addition, a carbonaceous material catalyst with high nitrogen content (up to 9.1 at.%) can also be fabricated via the one-pot hydrothermal method (Table 2.3). It indicates that one-step method is a good alternative for nitrogen-atom incorporation. Notably, nitrogen atoms in PYD and DFM are possibly more different to be introduced into the carbon materials (Figure 2.9 and Table 2.3). Although the content of Fe appears to be related to the source of the nitrogenous reagent, the relationship between Fe content and nitrogenous reagent is not clear. However, when we further

correlate Fe content with the intensity of I_D/I_G, a positive-going relationship emerges (Table 2.4 and Figure 2.10). Obviously, Fe content is affected by I_D/I_G intensity, which is determined by the nitrogenous functional groups. Generally, nitrogenous groups, as an anchor of active sites, contribute to the immobilization of iron species [45, 48], thus there should be some relationship between the amount of iron species and the amount of nitrogen. By contrast, a good linear relationship exists between the iron content and the amount of defect sites (Figure 2.10) rather than the content of nitrogen atom. Therefore, the iron species are more likely to interact with the defect sites, not just the well-recognized anchoring effect from the nitrogen-containing groups. As discussed above, the preparation process of nitrogen functionalized carbonaceous material catalysts involves a series of complex steps. Similarly, it is reported that the existence of iron species can also influence the amount of nitrogen-atom doping and graphitization degree besides the morphological structure of catalyst [54]. Therefore, it is well accepted that there are some interactions among Fe, N and C elements for these formed nitrogen-containing catalysts. According to Table 2.2, the intensity of I_D/I_G after the reaction changes to a certain extent, which is derived from structural reconstruction or structure damage. In view of this, we can infer that the presence of nitrogen-containing functional groups in the catalyst will affect the structural changes during the reaction, in which I_D/I_G intensity is a visual manifestation. In other words, the presence of nitrogen atoms can regulate the surface defects of the catalyst during the reaction. At the same time, there exists an interaction between these defect sites and iron species which are active sites for catalyzing CO_2 hydrogenation. From the visual representation analysis, it reaches a good linear relationship between these defects and the surface iron content.

To determine the types of nitrogenous species or bonding configurations of

incorporated N-atom, N1s XPS spectra for these nitrogen functionalized catalysts were deconvoluted (Figure 2.11). All of these nitrogen functionalized catalysts have two characteristic peaks, regardless of what kind of nitrogen-containing reagent being used. The binding energy peaks at around 400.3 and 398.8 eV in the N1s spectra are ascribed to pyridine nitrogen and pyrrolic nitrogen, respectively [48, 55]. The N doping in carbon materials changes electron donor state (C-C/C-N 2pπ electron state) such as the enhancement of state density near the Fermi level [56, 57]. Pyridine-like nitrogen structures are able to change the valence band structure of C network efficiently, and the metal-like behavior derived from N doping is related to this feature [56, 57]. However, the pyridine-like nitrogen content is significantly decreased with the introduction of DFM and PYD reagents. The introduction of different nitrogen functional groups regulates the bonding configurations of nitrogen. Such different configurations exhibit variant effects, and then present the tuned for catalytic performance. In other words, the catalysts modified by DFM and PYD reagents may exhibit a poor promotional behavior.

Fe2p spectra of reference Fe/C and nitrogen functional catalysts are also compared (Figure 2.12). Compared with the reference Fe/C catalyst, the Fe2p3/2 peaks with nitrogen modification shifts toward low binding energy, indicating the increase of electron density for iron species. It is reported that the enhanced electron density of iron species derived from electron transfer, intensifies Fe-C bond while weakens the C-O bond [45, 58]. Although the nitrogen atoms adopt sp2 hybrid configuration in both pyridine-like and pyrrolic-like nitrogen structures, the nitrogen from the pyridine conjugated structure shows higher electron density than that of pyrrolic nitrogen groups. Hence, this high electron density nitrogen atom is more conducive to stabilizing the Fe-C bond, which is consistent with XRD results (Figure 2.5). Lu et al. also demonstrated that the nitrogen

incorporation promotes the formation of active carbides through Mössbauer spectra results [45]. In fact, according to the XRD patterns (Figure 2.5), it can be found that the use of different nitrogen containing reagents can significantly affect the formation of active phase. For Fe/C-PYD and Fe/C-DFM catalysts, the content of active phase (Fe_3O_4 and Fe_5C_2) decreased with the introduction of nitrogen reagents (PYD and DFM). Therefore, despite the presence of electron-enriched carbides, the catalytic activity was not improved, as shown in Table 2.5. Obviously, the high active phase content and the presence of electron-rich carbides are beneficial to improve the catalytic performance if these factors exist simultaneously.

Generally controllable morphologic structure and composition of the catalyst are of importance for understanding the reaction process or mechanism. For these functionalized carbonaceous material catalysts, the morphology, structure as well as composition can be well regulated via the introduction of varied nitrogenous reagents. Moreover, the nitrogen configuration in the catalyst system can also be tuned by applying different nitrogen-containing groups (Figure 2.11). Hence, the preparation process of these catalysts is a promising way for the fabrication of well-defined functionalized catalyst.

2.3.2 Catalytic performance of varied catalysts for CO_2 hydrogenation

CO_2 hydrogenation performances over these functionalized catalysts were evaluated in a fixed bed and summarized in Table 2.5. After adding PYL reagent as a nitrogen source, high CO_2 hydrogenation activity (21.6%) and low undesired CO by-product selectivity (29.2%) are achieved, compared to those achieved with the reference Fe/C (Table2.5, Entry 1-2). Meanwhile, the selectivity of liquid hydrocarbons is also increased slightly (Table 2.5, Figure 2.13a). As mentioned above, the existence of PYL can promote the

generation of small-sized carbide species of spent catalyst (Figure 2.2), in addition, it can also promote the increase of as-prepared catalyst surface area (Table 2.1). Unlike the other three nitrogenous reagents, PYL not only promotes the reduction process (moving towards lower temperatures), but also significantly improves the adsorption behavior of carbon dioxide on the surface of catalyst (Figure 2.7 and 2.8). These factors play an important role in the formation of active phase and the efficient formation of subsequent products. The XRD pattern also shows that the PYL-modified iron catalyst still has a good active carbide diffraction peak for the spent catalyst than Fe/C-PYD and Fe/C-DFM. Meanwhile, high-resolution of N1s XPS spectra of spent nitrogen functionalized catalyst showed that the PYL modified iron-based catalyst had more pyridine nitrogen, which is crucial for improving CO_2 hydrogenation performance. Therefore, compared with reference Fe/C catalyst, PYL modified catalysts presented higher activity (21.6% vs. 16.9%) and product selectivity (29.2% CO sel. vs. 41.2% CO sel.) For EDA reagent, the CO_2 hydrogenation activity (18.5%) is slightly increased without decreasing the CO selectivity. However, its product distribution of formed hydrocarbon migrates from long-chain hydrocarbons to low-carbon hydrocarbons. In fact, different from PYL addition, the catalyst after the reaction has a larger active phase size for EDA modified Fe/C catalyst (Figure 2.2), thus it presents a lower activity than PYL-modified one. Different from PYL and EDA reagent, catalytic activity is decreased obviously with the modifications from the other two nitrogen-containing reagents (Table 2.5, Entry 4-5). The main products are light hydrocarbons, especially for CH_4. This weak chain growth is due to poor active carbide formation (Figure 2.5) and low content of pyridine-like nitrogen structures (Figure 2.11), which are crucial for the formation of heavy hydrocarbons [59]. In addition, XRD patterns (Figure 2.5) clearly indicate that the doping of DFM or PYD is not

conducive to the carbonization of iron species or active phase formation (Fe_3O_4 and Fe_5C_2). Correspondingly, it presents an inferior catalytic (Table 2.5, 15.8% of DFM and 15.9% of PYD) activity than EDA and PYL modified Fe/C (21.6% of PYL, and 18.5% of EDA). It is worth noting that although the utilization of PYD can significantly promote the increase of specific surface area of as-synthesized Fe/C-PYD, the surface composition of the catalyst after the reaction shows that the surface composition has a more direct effect on the reaction by combining experiment results and characterization data. The detailed hydrocarbons distribution is compared in Figure 8a. The results of the CO_2 conversion as well as CO selectivity as a function of time on stream are also listed in Figure 2.13b and 2.13c. As observed, these carbon-supported iron catalysts reached steady state within 6 h. Besides that, the effect of PYL reagent additive amount on CO_2 hydrogenation performance was also studied (Figure 2.14). Compared with the reference Fe/C catalyst, the utilization of PYL reagent can reduce the selectivity of CO by-product. In other words, introduction of PYL reagent as a powerful catalyst modifier is conducive to the efficient use of carbon element.

Most of carbon support materials can be synthesized through organic template methods, such as the glucose mentioned above. On the basis we also considered whether these nitrogen-containing reagents could serve as templates to provide both nitrogen source and carbon source. Based on this catalyst design concept, we further evaluated the CO_2 hydrogenation performance over the corresponding catalysts. Compared with Fe/C-PYL, poor catalytic performance of the Fe-PYL was observed under the same conditions (Table 2.6). It indicated that the hydrothermal self-assembly process by coupling glucose and PYL or carbonizing glucose was more favorable and efficient than the utilization of pyridine alone. This effect was mainly due to the influences of organic templates (nitrogen

and carbon source) during hydrothermal process, thus it led to the differences in catalytic performance.

2.4. Conclusions

Nitrogen functionalized carbonaceous materials with embedded iron nanoparticles, acting as CO_2 hydrogenation catalysts, were developed successfully through a facile one-pot hydrothermal synthesis process. The morphologies and structures changed obviously with the implantation of different nitrogenous reagent. Besides, the introduction of nitrogenous reagents facilitated the formation of defect sites except EDA reagents. The microstructure for Fe/C-PYL and Fe/C-EDA was more stable than that of Fe/C-PYD and reference Fe/C. The content of iron presents a positive-going functional relationship with the amount of defect sites labeled as I_D/I_G intensity. Although N atom was well introduced into carbon support materials, the content of N atom and N bonding configurations differed by original reagents. The functionalized processes from PYL and EDA reagents were beneficial for the formation of pyridine-like nitrogen structures, which were responsible to the metal-like promoter behavior. Combined with characterization and experiment findings, it is concluded that the specific surface area, the amount of defect sites, the carbonization degree of iron species precursor, and the content of pyridine-like nitrogen structures played a crucial role in improving the catalytic performance of CO_2 hydrogenation. PYL as a well-performing nitrogen source precisely regulated the physiochemical properties of the final catalyst, consequently achieving an outstanding performance. This nitrogen-doped carbon material provided an efficient strategy or concept for catalyzing CO_2 hydrogenation.

References

[1] W. Li, H. Wang, X. Jiang, J. Zhu, Z. Liu, X. Guo, C. Song, RSC Adv, 8 (2018) 7651-7669.

[2] H. Yang, C. Zhang, P. Gao, H. Wang, X. Li, L. Zhong, W. Wei, Y. Sun, Catal Sci Technol, 7 (2017) 4580-4598.

[3] S. Saeidi, N.A.S. Amin, M.R. Rahimpour, J CO2 Util, 5 (2014) 66-81.

[4] M.V. Landau, R. Vidruk, M. Herskowitz, ChemSusChem, 7 (2014) 785-794.

[5] W. Wang, S. Wang, X. Ma, J. Gong, Chem Soc Rev, 40 (2011) 3703-3727.

[6] Y.M. Ni, Z.Y. Chen, Y. Fu, Y. Liu, W.L. Zhu, Z.M. Liu, Nat Commun, 9 (2018) 3457.

[7] J. Wei, Q. Ge, R. Yao, Z. Wen, C. Fang, L. Guo, H. Xu, J. Sun, Nat Commun, 8 (2017) 15174-15181.

[8] P. Gao, S. Li, X. Bu, S. Dang, Z. Liu, H. Wang, L. Zhong, M. Qiu, C. Yang, J. Cai, W. Wei, Y. Sun, Nat Chem, 9 (2017) 1019-1024.

[9] P. Gao, S. Dang, S. Li, X. Bu, Z. Liu, M. Qiu, C. Yang, H. Wang, L. Zhong, Y. Han, Q. Liu, W. Wei, Y. Sun, ACS Catal, 8 (2017) 571-578.

[10] L. Guo, J. Sun, X. Ji, J. Wei, Z. Wen, R. Yao, H. Xu, Q. Ge, Commun Chem, 1 (2018) 11.

[11] F. Studt, I. Sharafutdinov, F. Abild-Pedersen, C. F. Elkjær, J.S. Hummelshøj, S. Dahl, I. Chorkendorff, J.K. Nørskov, Nat Chem, 6 (2014) 320-324.

[12] L.X. Wang, L. Wang, J. Zhang, X.L. Liu, H. Wang, W. Zhang, Q. Yang, J.Y. Ma, X. Dong, S.J. Yoo, J.G. Kim, X.J. Meng, F.S. Xiao, Angew Chem, 130 (2018) 1-6.

[13] L. Guo, J. Sun, Q. Ge, N. Tsubaki, J Mater Chem A, 6 (2018) 23244-23262.

[14] B.L. Liang, T. Sun, J.G. Ma, H.M. Duan, L. Li, X.L. Yang, Y.R. Zhang, X. Su, Y.Q. Huang, T. Zhang, Catal Sci Technol, 9 (2019) 456-464.

[15] Z.Q. Ma, M.D. Porosoff, ACS Catal, 9 (2019) 2639-2656.

[16] W.D. Shafer, G. Jacobs, U.M. Graham, H.H. Hamdeh, B.H. Davis, J Catal, 369 (2019) 239-248.

[17] X.Z. Shao, X.F. Yang, J.M. Xu, S. Liu, S. Miao, X.Y. Liu, X. Su, H.M. Duan, Y.Q. Huang, T. Zhang, Chem, 5 (2019) 1-13.

[18] Y.B. Xu, C.M. Shi, B. Liu, T. Wang, J. Zheng, W.P. Li, D.P. Liu, X.H. Liu, Catal Sci Technol, 9 (2019) 593-610.

[19] Y. Wang, L. Tan, M.H. Tan, P.P. Zhang, Y. Fang, Y. Yoneyama, G.H. Yang, N. Tsubaki, ACS Catal, 9 (2019) 895-901.

[20] M. Oschatz, J.P. Hofmann, T.W.v. Deelen, W.S. Lamme, N.A. Krans, E.J.M. Hensen, K.P.d. Jong, ChemCatChem, 9 (2017) 620-628.

[21] S.-S. Nam, H. Kim, G. Kishan, M.-J. Choi, K.-W. Lee, Appl Catal A-Gen, 179 (1999) 155-163.

[22] T. Herranz, S. Rojas, F.J. Pérez-Alonso, M. Ojeda, P. Terreros, J.L.G. Fierro, Appl Catal A-Gen, 308 (2006) 19-30.

[23] T. Xie, J. Wang, F. Ding, A. Zhang, W. Li, X. Guo, C. Song, J CO2 Util, 19 (2017) 202-208.

[24] N. Boreriboon, X. Jiang, C. Song, P. Prasassarakich, J CO2 Util, 25 (2018) 330-337.

[25] G. Liu, Q. Chen, E. Oyunkhand, S. Ding, N. Yamane, G. Yang, Y. Yoneyama, N. Tsubaki, Carbon, 130 (2018) 304-314.

[26] M.L. Cubeiro, H. Morales, M.R. Goldwasser, M.J. Pérez-Zurita, F. González-Jiménez, C.U.d. N, Appl Catal A-Gen, 189 (1999) 87-97.

[27] W. Hou, B. Wu, Y. Yang, Q. Hao, L. Tian, H. Xiang, Y. Li, Fuel Process Technol, 89 (2008) 284-291.

[28] J. Sun, L. Guo, Q. Ma, X. Gao, N. Yamane, H. Xu, N. Tsubaki, Chem Asian J, 12 (2017) 366-371.

[29] L. Guo, J. Sun, J. Wei, Z. Wen, H. Xu, Q. Ge, J Energy Chem, 26 (2017) 632-638.

[30] T. Yang, J. Liu, R. Zhou, Z. Chen, H. Xu, S.Z. Qiao, M.J. Monteiro, J Mater Chem A, 2 (2014) 18139-18146.

[31] J.W. Qi, G.P. Wei, Y. Li, J.S. Li, X.Y. Sun, J.Y. Shen, W.Q. Han, L.J. Wang, Chem Eng J, 339 (2018) 499-508.

[32] Y. Chen, B. Song, M. Li, L. Lu, J. Xue, Adv Funct Mater, 24 (2014) 319-326.

[33] J.G. Wang, H.Z. Liu, H.H. Sun, W. Hua, H.W. Wang, X.R. Liu, B.Q. Wei, Carbon, 127 (2018) 85-92.

[34] F. Ma, H. Zhao, L. Sun, Q. Li, L. Huo, T. Xia, S. Gao, G. Pang, Z. Shi, S. Feng, J Mater Chem, 22 (2012) 13464-13468.

[35] J. Wei, J. Sun, Z. Wen, C. Fang, Q. Ge, H. Xu, Catal Sci Technol, 6 (2016) 4786-4793.

[36] W. Shen, W. Fan, J Mater Chem. A 1 (2013) 999-1013.

[37] H. Chen, F. Sun, J. Wang, W. Li, W. Qiao, L. Ling, D. Long, J Phys Chem C, 117 (2013) 8318-8328.

[38] H.J. Schulte, B. Graf, W. Xia, M. Muhler, ChemCatChem, 4 (2012) 350-355.

[39] L.M. Chew, P. Kangvansura, H. Ruland, H.J. Schulte, C. Somsen, W. Xia, G. Eggeler, A. Worayingyong, M. Muhler, Appl Catal A-Gen, 482 (2014) 163-170.

[40] Z. Li, R. Liu, Y. Xu, X. Ma, Appl Surf Sci, 347 (2015) 643-650.

[41] P. Kangvansuraa, L.M. Chewb, W. Saengsuic, P. Santawajad, Y. Poo-arporne, M. Muhlerb, H. Schulzf, A. Worayingyong, Catal Today, 275 (2016) 59-65.

[42] S. Kundu, W. Xia, W. Busser, M. Becker, D.A. Schmidt, M. Havenith, M. Muhler,

Phys Chem Chem Phys, 12 (2010) 4351-4359.

[43] R. Arrigo, M. Hävecker, R. Schlögl, D.S. Su, Chem Comm, 0 (2008) 4891-4893.

[44] G. Yu, B. Sun, Y. Pei, S. Xie, S. Yan, M. Qiao, K. Fan, X. Zhang, B. Zong, J Am Chem Soc, 132 (2010) 935-937.

[45] J. Lu, L. Yang, B. Xu, Q. Wu, D. Zhang, S. Yuan, Y. Zhai, X. Wang, Y. Fan, Z. Hu, ACS Catal, 4 (2014) 613-621.

[46] H.M.T. Galvis, J.H. Bitter, T. Davidian, M. Ruitenbeek, A.I. Dugulan, K.P.d. Jong, J Am Chem Soc, 134 (2012) 16207-16215.

[47] H. Xiong, M. Moyo, M.A.M. Motchelaho, L.L. Jewell, N.J. Coville, Appl Catal A-Gen, 388 (2010) 168-178.

[48] H. Xiong, M. Moyo, M.A. Motchelaho, Z.N. Tetana, S.M.A. Dube, L.L. Jewell, N.J. Coville, J Catal, 311 (2014) 80-87.

[49] J. Sun, H. Xu, G. Liu, P. Zhu, R. Fan, Y. Yoneyama, N. Tsubaki, ChemCatChem, 7 (2015) 1642-1645.

[50] J. Zhang, X. Wang, G. Qi, B. Li, Z. Song, H. Jiang, X. Zhang, J. Qiao, Carbon, 96 (2016) 864-870.

[51] M.C. Bahome, L.L. Jewell, D. Hildebrandt, D. Glasser, N.J. Coville, Appl Catal A-Gen, 287 (2005) 60-67.

[52] B. Hu, K. Wang, L. Wu, S.H. Yu, M. Antonietti, M.M. Titirici, Adv Mater, 22 (2010) 813-828.

[53] M. Sevilla, A.B. Fuertes, Chem Eur J, 15 (2009) 4195-4203.

[54] Z.X. Yan, C.J. Dai, M.M. Zhang, X.M. Lv, X.H. Zhao, J.M. Xie, Int J Hydrogen Energ, 44 (2019) 4090-4101.

[55] N.P. Wickramaratne, J. Xu, M. Wang, L. Zhu, L. Dai, M. Jaroniec, Chem Mater, 26

(2014) 2820-2828.

[56] R. Czerw, M. Terrones, J.-C. Charlier, X. Blase, B. Foley, R. Kamalakaran, N. Grobert, H. Terrones, D. Tekleab, P.M. Ajayan, W. Blau, M. Rühle, D.L. Carroll, Nano Lett, 1 (2001) 457-460.

[57] Z. Luo, S. Lim, Z. Tian, J. Shang, L. Lai, B. MacDonald, C. Fu, Z. Shen, T. Yu, J. Lin, J Mater Chem, 21 (2011).

[58] Q. Zhang, J. Kang, Y. Wang, ChemCatChem, 2 (2010) 1030-1058.

[59] Y.H. Choi, Y.J. Jang, H. Park, W.Y. Kim, Y.H. Lee, S.H. Choi, J.S. Lee, Appl Catal B-Environ, 202 (2017) 605-610.

Table 2.1 Surface area and average diameter of reference and nitrogen functionalized catalysts.

Entry	Catalyst	Surface area / m^2/g)[a]	Average diameter (μm)[b]
1	Fe/C	6.7	7
2	Fe/C-PYL	33.7	3
3	Fe/C-EDA	10.6	6
4	Fe/C-DFM	4.0	12
5	Fe/C-PYD	35.7	3

[a] Determined by BET curves. [b] Determined by SEM micrographs.

Table 2.2 The relative intensities (I_D/I_G) of G band and the D band for fresh and spent catalysts.

Entry	Catalyst	I_D/I_G[a]	
		Used	Fresh
1	Fe/C	2.27	1.32
2	Fe/C-PYL	1.55	1.92
3	Fe/C-EDA	1.21	1.11
4	Fe/C-DFM	1.57	1.66
5	Fe/C-PYD	4.19	1.75

[a] Determined by Raman spectroscopy.

Table 2.3 Elemental compositions of nitrogen functionalized carbon supported iron catalysts.

Entry	Catalyst	XPS analysis / (atom) %			
		Fe	C	O	N
1	Fe/C	8.2	69.4	22.4	/
2	Fe/C-PYL	4.5	68.9	22.2	6.4
3	Fe/C-EDA	3.8	60.2	26.9	9.1
4	Fe/C-DFM	4.6	74.2	17.8	3.4
5	Fe/C-PYD	17.5	31.8	49.5	1.2

Table 2.4 Positive relationship between structural defects and surface iron content.

Entry	Catalyst	I_D/I_G[a]	Content (atom) %[b]
		Used	Fe
1	Fe/C-PYD	4.19	17.5
2	Fe/C	2.27	8.2
3	Fe/C-DFM	1.57	4.6
4	Fe/C-PYL	1.55	4.5
5	Fe/C-EDA	1.21	3.8

[a] Determined by Raman spectroscopy. [b] Determined by XPS results.

Table 2.5 Catalytic performance of CO_2 hydrogenation over nitrogen functionalized catalysts.

Entry	Catalyst	T / °C	P / MPa	W/F / g·h·mol^{-1}	Conv. / %	CO Sel. / %	Selectivity / (c-mol) %		
							CH_4	C_2-C_4	C_{5+}
1	Fe/C	300	1.0	12	16.9	41.2	36.6	47.5	15.9
2	Fe/C-PYL	300	1.0	12	21.6	29.2	36.8	46.0	17.2
3	Fe/C-EDA	300	1.0	12	18.5	41.4	42.2	47.4	10.4
4	Fe/C-DFM	300	1.0	12	15.8	55.2	45.1	45.9	8.9
5	Fe/C-PYD	300	1.0	12	15.9	40.5	46.8	47.1	6.1

Table 2.6 Catalytic performance over different functional iron-based catalysts.

Entry	Catalyst	T / °C	P / MPa	W/F / g·h·mol^{-1}	Conv. / %	CO Sel. / %	Selectivity / (c-mol) %		
							CH_4	C_2-C_4	C_{5+}
1	Fe/C	300	1.0	12	16.9	41.2	36.6	47.5	15.9
2	Fe/C-PYL[a]	300	1.0	12	21.6	29.2	36.8	46.0	17.2
3	Fe-PYL[b]	300	1.0	12	14.2	38.7	38.4	47.4	14.1

[a] Glucose is the carbon source and PYL is the nitrogen source. [b] PYL is the carbon and nitrogen source.

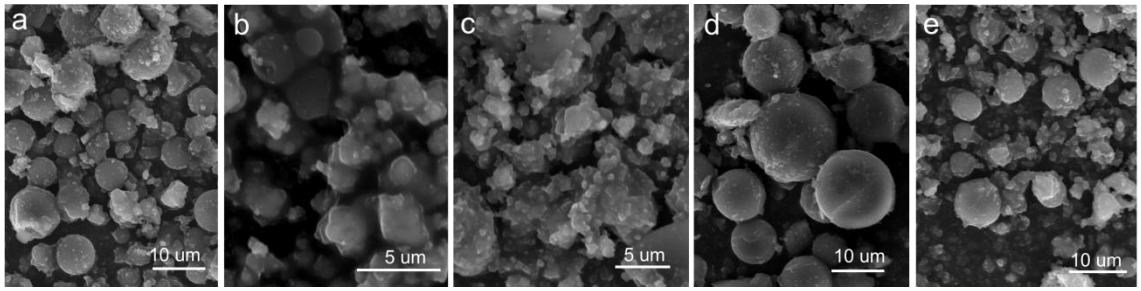

Figure 2.1 Typical SEM images of fresh (a) Fe/C, (b) Fe/C-PYL, (c) Fe/C-EDA, (d) Fe/C-DFM, (e) Fe/C-PYD.

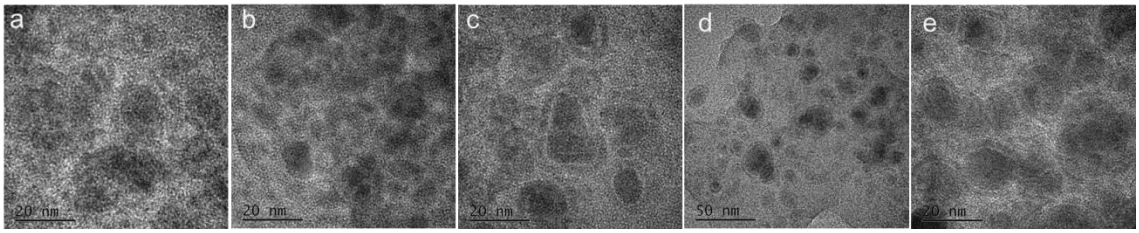

Figure 2.2 Typical TEM images of spent (a) Fe/C, (b) Fe/C-PYL, (c) Fe/C-EDA, (d) Fe/C-DFM, (e) Fe/C-PYD.

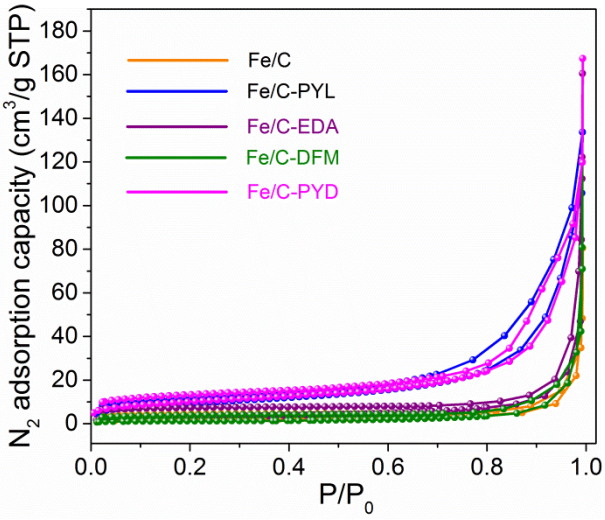

Figure 2.3 N_2 adsorption-desorption isotherms of nitrogen functionalized catalysts.

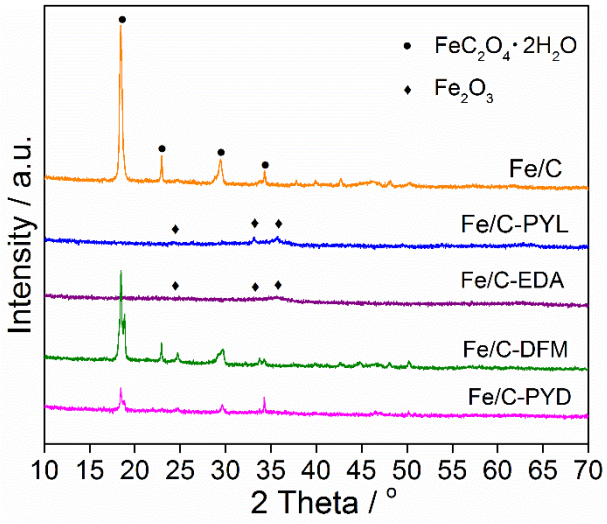

Figure 2.4 XRD patterns of the as-prepared iron-based catalysts.

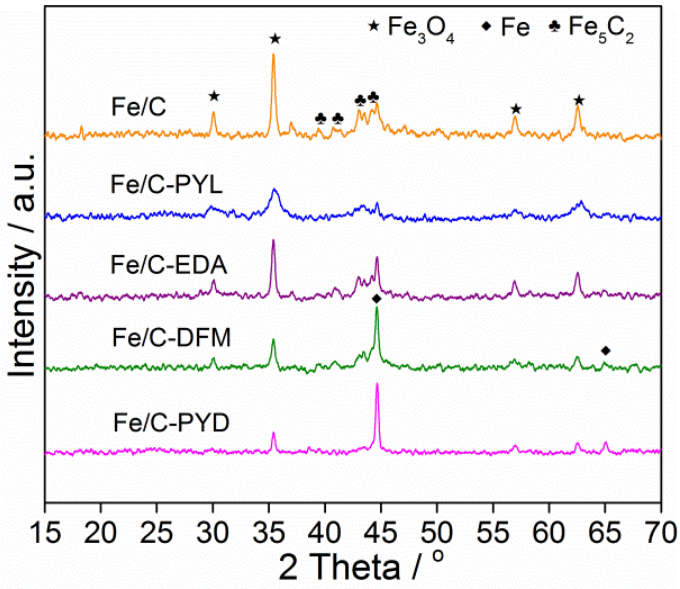

Figure 2.5 XRD patterns of the spent iron-based catalysts.

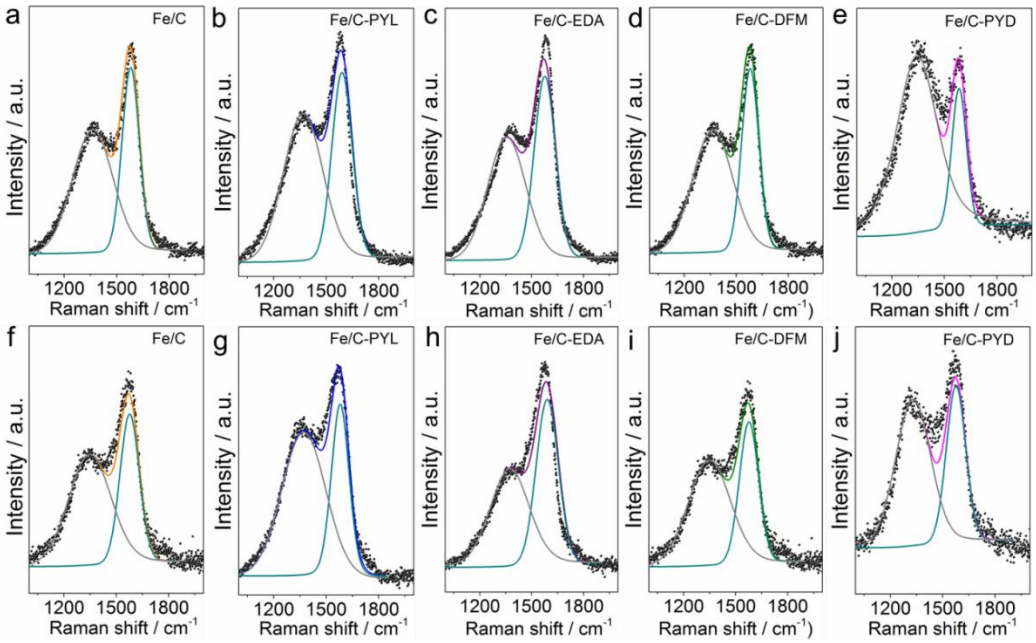

Figure 2.6 De-convolution of Raman spectra. (a-e) spent catalyst, (f-j) fresh catalysts.

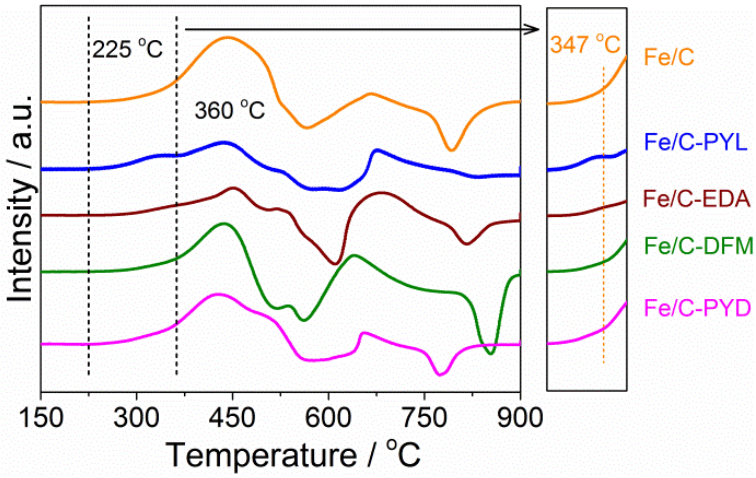

Figure 2.7 H_2-TPR profiles of the different nitrogen functionalized catalysts.

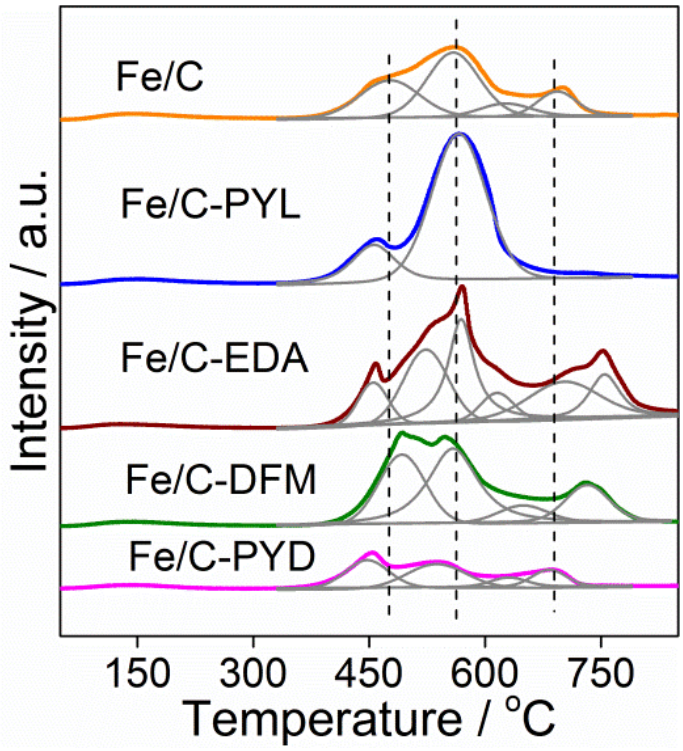

Figure 2.8 CO_2-TPD profiles of the different nitrogen functionalized catalysts.

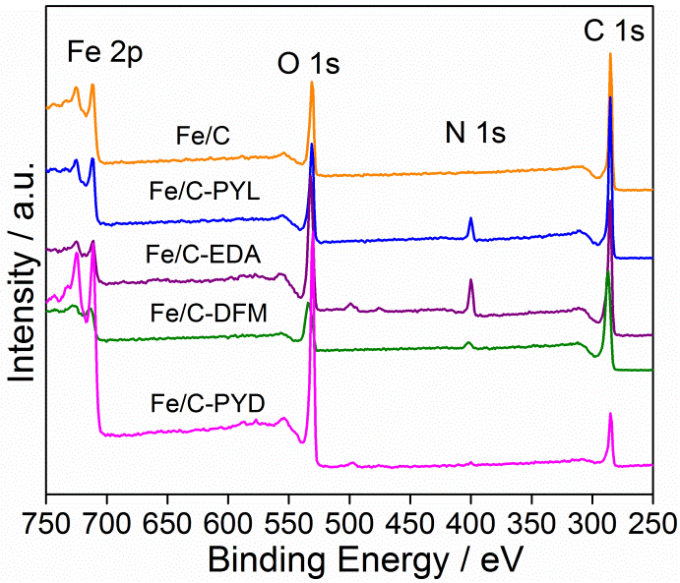

Figure 2.9 XPS survey scan spectra of different Fe-based catalysts.

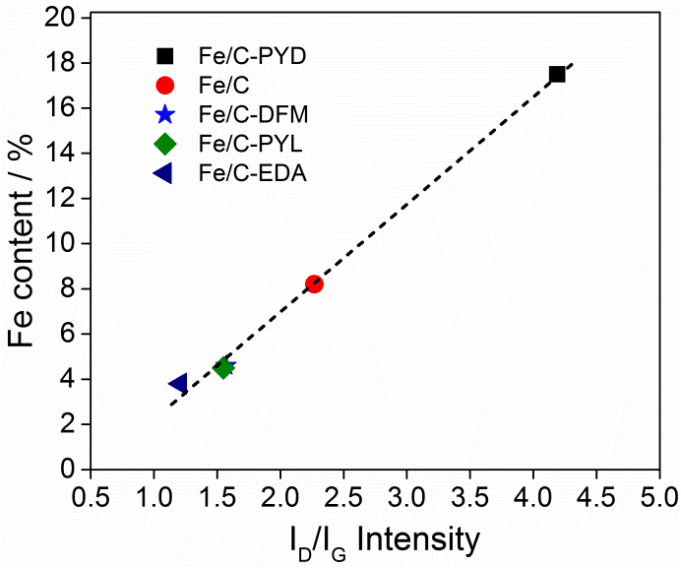

Figure 2.10 The positive-going relationship between I_D/I_G intensity and Fe atom content.

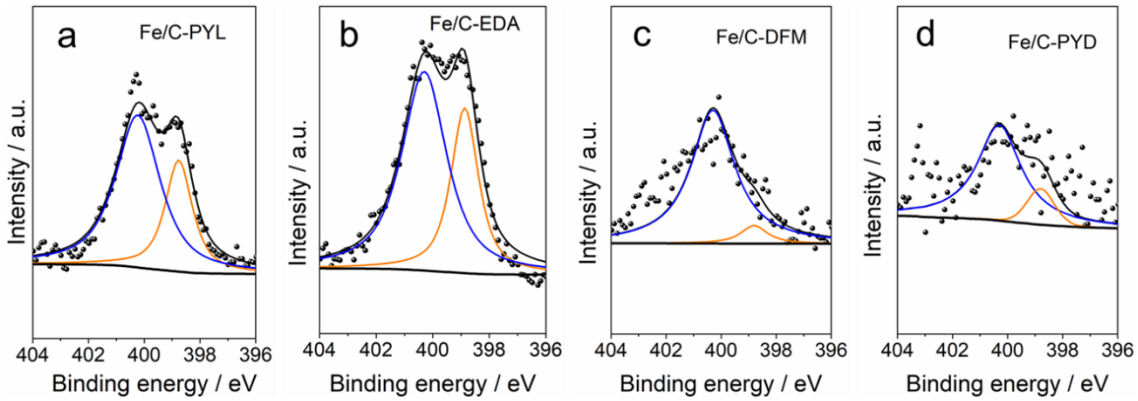

Figure 2.11 High-resolution N1s (a-d) XPS spectra of spent nitrogen functionalized catalysts (Blue line represents pyrrolic nitrogen, and Orange line represents pyridine nitrogen).

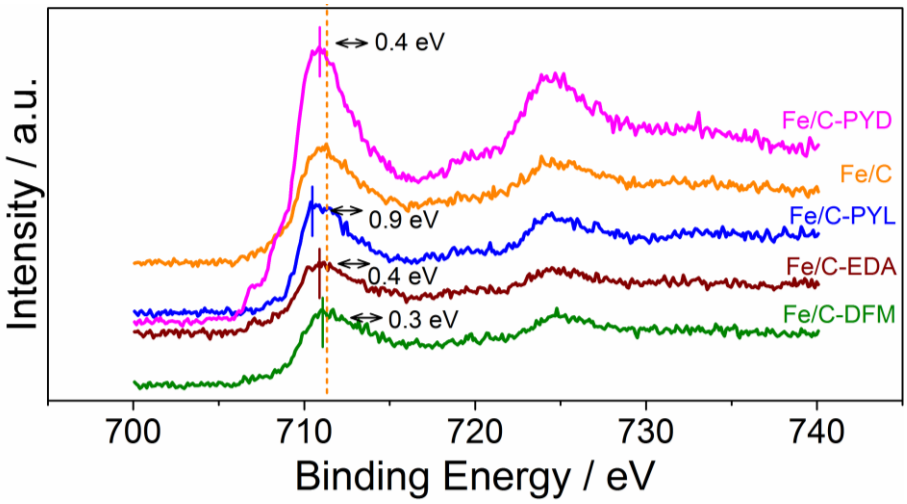

Figure 2.12 High-resolution Fe2p XPS spectra of spent nitrogen functionalized catalysts.

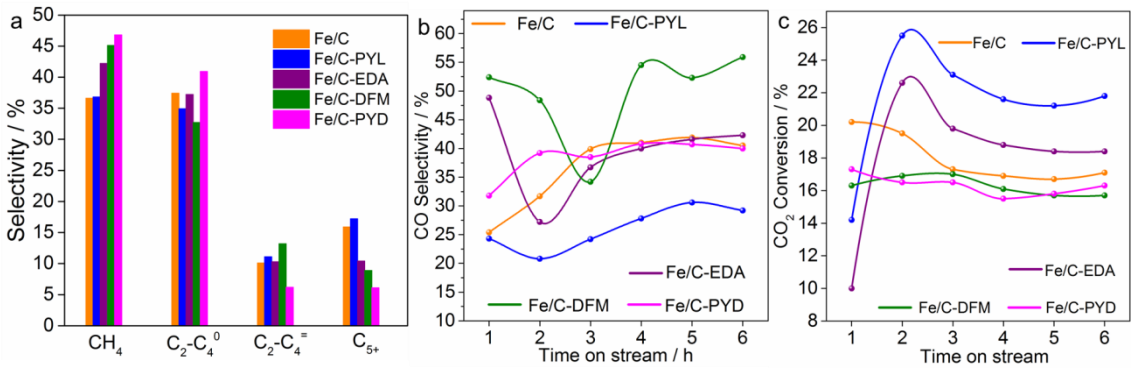

Figure 2.13 (a) Comparison of the product distribution over different catalysts. (b) CO selectivity vs time on stream. (c) CO_2 hydrogenation activity vs time on stream.

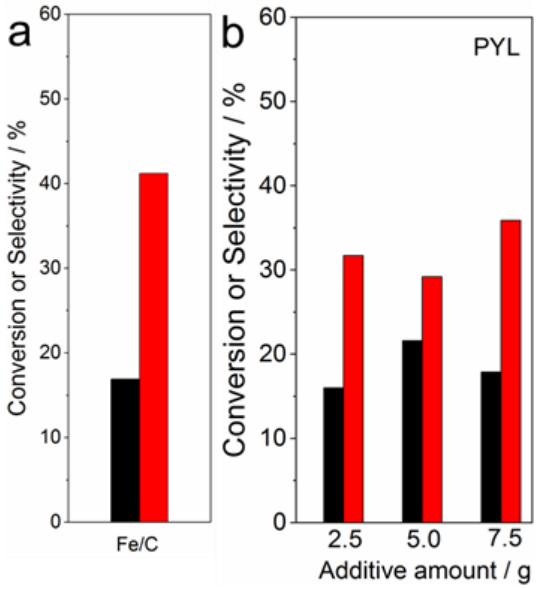

Figure 2.14 The catalytic performances over a reference Fe/C and PYL functionalized catalysts (black bar represents CO_2 conversion, and red bar represents CO selectivity).

Chapter 3

Combined Methane Dry Reforming and Methane Partial Oxidization for Syngas Production over High Dispersion Ni Based Mesoporous Catalyst

Ni based mesoporous Al_2O_3 catalysts were prepared by evaporation-induced self-assembly (EISA) method, and were employed as catalyst in combined methane dry reforming (DRM) and methane partial oxidization (POM) reaction.

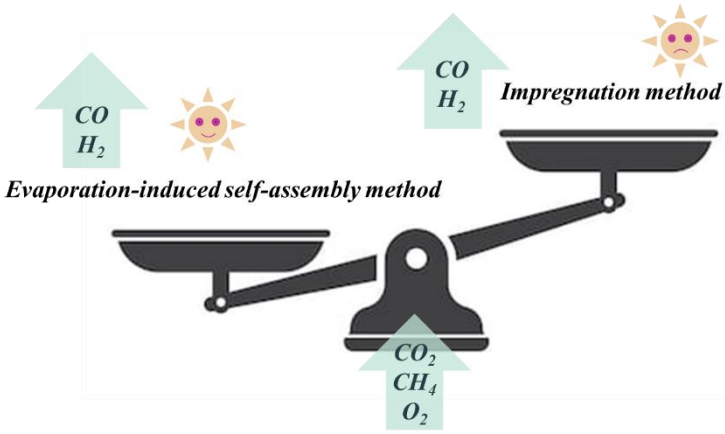

Abstract

Ni based mesoporous Al_2O_3 catalysts were prepared by evaporation-induced self-assembly (EISA) method, and were employed as catalyst in combined methane dry reforming (DRM) and methane partial oxidization (POM) reaction. Transmission electron micrographs (TEM), N_2 physical adsorption-desorption, H_2 chemisorption and temperature programmed reduction (H_2-TPR), X-ray diffraction (XRD) and Raman spectroscopy were used to characterize the catalysts. The TEM and N_2-physisorption characterization showed that the catalysts had typical mesoporous structure. The catalytic activity tests results indicated that the catalysts prepared by the one-pot method had better catalytic performance for combined methane dry reforming and methane partial oxidation reaction. The coupling reactions between DRM and POM in the mesoporous channel can facilitate the heat exchange better, then promoting catalytic performance. The TEM and Raman analysis of used catalysts showed that combined DRM with POM could effectively suppress the formation of carbon on catalysts surface.

Keywords: Methane dry reforming, Mesoporous alumina, Nickel-based catalyst, Methane partial oxidation

3.1. Introduction

Methane dry reforming (DRM) to produce synthesis gas is a most important process in C1 chemistry, which has received extensive attention in the last two decades [1-6]. On one hand, it is a potential chemical way to utilize methane and CO_2, two main greenhouse gases resulting in serious environment problem. On the other hand, synthesis gas, the product of methane dry reforming, is an important raw material to produce liquid hydrocarbons [7-9].

Methane dry reforming reaction is a highly endothermic process according to reaction thermodynamics, requiring large amount of extra energy. Meanwhile, another deficiency of methane dry reforming process is that large whiskers carbon generating on the catalyst surface, which could deactivate the activity of catalyst and results in another problems [10-13]. Besides, the molar ratio of H_2/CO produced in DRM process is often less than 1, which does not match the need of the process of methanol synthesis and Fischer-Tropsch synthesis [13-15].

On account of the above problems, it is desired to couple the methane dry reforming with other reaction process to overcome abovementioned deficiencies. As we know that POM reaction is a typical exothermic process [16-18], which stoichiometrically produces a H_2/CO molar ratio of 2. However, this POM reaction is difficult to control, because of the appearance of hot spot and the possible risk of explosion in reaction. It is also difficult to keep the catalyst being maintained in reducing state. Thus, the combination of endothermic DRM process and exothermic POM process is expected to overcome the shortcomings of both two processes. The combined process (DRM-POM) can also effectively interchange the energy by combining the exothermic process and the endothermic process of DRM and POM reaction [19-21]. Furthermore, it can provide

different H_2/CO molar ratio to meet the gas to liquid (GTL) process by changing the O_2/CO_2 ratio of reactant composition.

In previous study, the main catalytic metal for POM-DRM process was noble metal [22-24], which could provide better catalytic activity and stability. However, the noble metal catalysts are unsuitable widely used for its high cost. Therefore, the low-cost metal and cobalt-based catalysts were also investigated [25, 26]. Great efforts had been made to improve the catalytic performance of nickel-based catalysts, such as modification with alkaline earth metal oxide or small amounts of noble metals, changing the structure or chemical composition of support, and so on.

Recently we found a reduced mesoporous alumina catalyst, with low content of Ni, was an excellent catalyst for methane dry reforming reaction under atmospheric pressure [27]. In addition, characterization results indicated that this kind of Ni-Al_2O_3 catalyst had higher dispersion of Ni metal particles and stronger nickel-alumina interaction than that of the supported catalyst after reduction. In this study, we investigated the performance of the typical mesoporous Al_2O_3 catalyst prepared by the EISA method in combined DRM and POM under same condition. For comparison, a supported catalyst with ordered mesoporous Al_2O_3 was also prepared by sample impregnation method. We expected that this kind of mesoporous Ni-Al_2O_3 catalysts with high dispersion of Ni will be also beneficial for the combined reaction of methane.

3.2. Experimental

3.2.1 Catalyst Preparation

The catalyst was prepared by the EISA method with minor modification as previous literature [7]. Typically, appropriate amount of surfactant $(EO)_{20}(PO)_{70}(EO)_{20}$ (P123,

Sigma Aldrich) was firstly dissolved in absolute ethanol. Then, the aluminum source aluminumisopropoxide and $Ni(NO_3)_2 \cdot 6H_2O$ were carefully added into the solution under vigorous stirring. After the nickel nitrate dissolved, a fixed amount of concentrated nitric acid was slowly dropped into the solution. Few minutes later, the aluminumisopropoxide dissolved, the solution was still vigorously stirred at least 5 h. The obtained suspension was heated at 60 °C to remove ethanol in a furnace with a small opened window for 72 h. The obtained product was heated to 700 °C at a rate of 2 °C min^{-1} and then calcined for 5 h under air atmosphere. The obtained catalyst sample was named as Ni-MA. The mesoporous alumina support (MA) was also synthesized according to the above method. Supported catalysts were prepared via conventional impregnation method using same nickel resource as above. The obtained sample was firstly dried at 120 °C at least 3 h and then calcined at 500 °C for 3 h. The loading of nickel was 6 wt% in both the catalyst samples.

To demonstrate the superiority of EISA method than impregnation method (post-treatment processing), the EISA method here was applied to synthesize related Ni-based catalysts. Thus, a nickel based catalyst with spinel-like structure prepared by evaporation-induced self-assembly was also compared for combined DRM and POM reaction. In brief, 0.01 mol $Ni(NO_3)_2 \cdot 6H_2O$, 0.02 mol $Al(NO_3)_3 \cdot 9H_2O$, and 0.066 mol urea melt at 120 ºC for 20 min. Thereinto, the molar ratio of urea / metal nitrate equals 2.2. Subsequently, the mixtures was transferred to 600 ºC muffle furnace to burn 30 min. after that, the catalyst precursor was further calcined at 700 ºC for 4h. The spinel-like structure ($NiAl_2O_4$) catalyst was obtained, labelled as $NiAl_2O_4$-C. For comparison, a similar structure of $NiAl_2O_4$ was also prepared through precipitation method, marked as $NiAl_2O_4$-P. Besides, to further enhance catalytic performance, Pt metal was impregnated on the surface of

catalyst. The loading of Pt in the catalyst system is 1.0 wt%.

3.2.2 Catalyst characterization

The powder X-ray diffraction data were collected using X-ray diffractometer (RinT2200V/PC, from Rigaku Corporation) in the 2θ region of 10-80°, operated at 40 kV and 30 mA.

Nitrogen physical adsorption measurements were measured using a physical absorption instrument (Autosorb-1-C, from Quantachrome) at -196 °C. The samples were pretreated by degassing under vacuum condition at 200 °C for 2 h. The surface area of samples was calculated according to BET method, and the distribution of pore was determined from the branch of desorption isotherms according to BJH method.

H_2-TPR was carried out on a reduction device (BELCAT-B-TT, JAPAN INC.) being connected to a thermal conductivity detector (TCD). A mixture gas (5 vol%H_2/Ar) was employed as reduction gas in a flow rate of 30 ml/min. All the samples were subjected in the range of 50-800 °C. The sample (about 30 mg) was heated to 150 °C for 1 h in the flow of Ar before each test.

The micro morphology was obtained by TEM on a transmission electron microscope (JEOL JEM-2100 UHR). Raman spectra were recorded using a Raman microscope (Renisha Invia 2000, UK) at 514.5 nm wave length. The samples were uniformly dispersed by ultrasound treatment and then dropped onto a transparent glass wafer.

The average particle size and exposed surface area of metal nickel were confirmed by H_2 chemisorption. The samples were firstly reduced by pure hydrogen at 700 °C before H_2 chemisorption, and then cooled to 30 °C under a flow of helium. After that, the chemisorption system was evacuated for 1 h and then the system gas changed to hydrogen to begin the chemisorption process.

3.2.3 Catalytic performance evaluation

The catalytic performance was evaluated over a static-bed catalytic reactor (quartz, i.d., 6 mm) under atmospheric pressure. The feed gas flow contained of CH_4, CO_2 and O_2 in a fixed molar ratio of CH_4:(CO_2+2O_2) = 1 and were introduced into reaction system by separate line, respectively. The Ar as internal standard substance was added into reaction with CH_4 in a molar ratio of CH_4: Ar = 9:1. The catalyst was firstly reduced at 700 °C for 2 h using a 5 vol% H_2/Ar as reductant at certain flow rate before each reaction. The effluent gas was firstly flowed through a cold trap in order to remove water vapors and then quantitatively analyzed using two different GC with TCD. The calculation method of conversion and the molar rate of H_2/CO was listed as following.

CH_4 conversion, vol% = $((CH_4/Ar)_{in} - (CH_4/Ar)_{out}) / (CH_4/Ar)_{in} \times 100$

CO_2 conversion, vol% = $((CO_2/Ar)_{in} - (CO_2/Ar)_{out}) / (CO_2/Ar)_{in} \times 100$

H_2/CO ratio = H_2 generation rate / CO generation rate

3.3. Results and discussion

3.3.1 Characterization of the as-prepared catalysts

Figure 3.1 shows the N_2 adsorption-desorption isothermal curves. As showed in Figure 3.1, the mesoporous samples presented the typical type-IV adsorption-desorption isotherms with clear hysteresis loops. This finding suggests that the ordered mesoporous pore appeared in the samples. By using the BJH method, the distributions of pore size are compared in Table 3.1. It is clear that the distributions of pore size are narrow, indicating there existed only one type of pore. It can be observed that all the samples possessed high surface area larger than 265 m^2/g and large pore volume. The average pore diameter was range from 8.43 to 12.2 nm. The nickel surface area of Ni/MA and Ni-MA, which was

calculated via hydrogen chemisorption, was 3.25 and 3.75m^2/g, respectively. For Ni-MA catalyst and Ni/MA catalyst, the introduction manner of Ni is different from each other. In terms of Ni-MA, Ni should be uniformly incorporated into the mesoporous MA bulk support during a synthesis process. Hence, smaller Ni particles might stay in smaller holes and then behave in a slightly larger aperture distribution than Ni/MA catalyst. As for Ni/MA catalyst, Ni particles would be uniformly dispersed on the surface of the MA support, and present a small pore size distribution. Based on BET results, it is can be deduced that the introduction manner of Ni can well regulate the pore size distribution of support. In view of the good stability of the catalyst as revealed by the following stability study, the reduced catalyst was not investigated. Generally, there exist five different hysteresis shapes for different catalytic supports. The H1 style hysteresis usually reflects the cylindrical pore structure with uniform diameter distribution, in which the tube opens at both ends. The H2 style hysteresis represents the complex pore structure such as ink-bottle type pores. And it can be further divided into H2a and H2b hysteresis. H2a usually exists in ordered 3D mesoporous materials. H2b is commonly found in ordered mesoporous materials after hydrothermal treatment. However, H3 and H4 style hysteresis represent an irregular pore structure. In the case of H5 style hysteresis, it is rare and it usually consists of a hole with two ends open and a hole with one end blocked. By comparing the hysteresis ring, it can be inferred that the samples exhibit an H2b hysteresis.

XRD patterns of the catalysts are compared in Figure 3.2. The catalysts were firstly reduced according to reduction procedure described in experiment section. It can be observed that there were three typical diffraction peaks in Figure 3.2b, which could be identified as the (311), (400) and (440) reflection of the γ-alumina. For the unreduced catalysts, it exhibited a broad peak around 20-30°, corresponding to an amorphous phase

of alumina, which is in accordance with previous reports [29, 30]. No evident characteristic peaks of NiO were found in Figure 3.2a, indicating that the nickel species were well dispersed on the support. On the reduced catalysts, the XRD patterns showed signals of diffraction peaks at 2θ=34.2°, 52.1°,76.6° and 37.0°, 45.0°,65.5°, which were indexed to the (111), (200), (220) and (311), (400) and (440) planes of metallic nickel and $NiAl_2O_4$ spinel, respectively. This indicated that Ni species existed in two forms. Compared with γ-alumina, the diffraction for Ni was quite weak, implying that the Ni clusters were very small.

The TEM images of samples are demonstrated in Figure 3.3. For MA and Ni-MA, it can be clearly observed that there existed homogeneous pores. For Ni/MA, it is clear that the nickel particles were uniformly dispersed on the surface of MA, which might block the pores of MA. But for Ni-MA, it can be found that there are no the nickel particles were appeared on the surface of MA, indicating the nickel particles were well embedded into the structure of γ-alumina.

The interaction between metal particles and support is very important factor for catalytic performance. TPR measurements were applied to investigate this interaction between nickel and γ-alumina and the TPR curves are showed in Figure 3.4. It can be found that the reduction temperature of Ni-MA appeared at 705 °C, but the reduction temperature of Ni/MA was located at 655 °C, about 50 °C lower than that of Ni-MA, suggesting the nickel γ-alumina interaction of Ni/MA was weaker than that of Ni-MA. This due to the fact that the nickel species in Ni-MA catalyst were completely embedded into the frame structure of γ-alumina during the preparation process by the EISA method.

3.3.2 Catalytic performance

Addition of oxygen to the reactant feed during the methane dry reforming can

effectively overcome the shortcomings of DRM and POM process. The methane conversion would increase due to part of methane taking part in POM reaction, compared with single DRM reaction. Meanwhile, the carbon dioxide conversion would slightly decrease for new CO_2 produced during POM reaction. The combined DRM and POM reaction results over Ni-MA and Ni/MA are presented in Figure 3.5. During 6 h reaction, the Ni-MA catalyst showed the conversions of CH_4 and CO_2 as 85.9% and 78.1% respectively. For Ni/MA, the conversion of CH_4 and CO_2 were 81.3% and 74.8%, respectively, lower than those of Ni-MA. This is because that the exposed Ni surface area of Ni-MA was 3.75m^2/g, larger than that of Ni/MA. As we all known that large exposed nickel surface area could provide more reaction sites for methane activation. Besides, DRM is endothermic and POM is exothermic. Obviously, for Ni-MA, the coupling reactions between DRM and POM in the mesoporous channel can facilitate the heat exchange (Figure 3.6), therefore we infer that the presence of mesoporous channel can also enhance the activity. As Ni-MA had higher catalytic activity and larger exposed activated sites, the followed reaction conditions experiment was focused on the Ni-MA catalyst. Previously, a Ce modified Pt/ZrO_2 catalyst was adopted for combined partial oxidation and dry reforming reaction of methane [31]. Thereinto, the conversion of CH_4 was only 54%, and when the reaction time reached 5 h, the conversion of CH_4 dropped to 50%. Besides, a NiO decorated MgO-ZrO_2 system was reported for POM and DRM coupled reactions [32]. Although this NiO-MgO-ZrO_2 catalyst had a good stability during 400 min, CH_4 conversion activity should have further improvement if compared with this mesoporous Ni-MA catalyst. Even compared with supported noble metal (e.g., Ru, Rh and Pt) catalysts [33, 34], the catalytic performances such as stability and reaction activity of this mesoporous Ni-MA catalyst are still rather comparable. Based on the points

discussed above, we can deduce that this mesoporous catalyst synthesized through one-step EISA method is a promising catalyst to some degree, and conducive to improving coupled reforming reaction performance consisting of DRM and POM process.

The influences of reaction temperature on H_2/CO molar ratio are showed in Figure 3.7. The H_2/CO molar ratio was decreased gradually with reaction temperature increasing, which is ascribed to another endothermic process (reverse water gas shift reaction). It occurred during the reaction and was promoted by increasing the temperature, which could consume CO_2 as well as H_2, and resulted in the increasing of CO_2 conversion as well as a decreasing of H_2/CO molar ratio accordingly.

The influences of CO_2/O_2 ratio are listed in Table 3.2. It can be found that the conversion of methane and the molar ratio of H_2/CO presented an increasing tendency with the decreasing of CO_2/O_2 molar ratio under different reaction temperature. According to the catalytic results, the CH_4 conversion increased from 68.0% to 80.7% at 700 °C and from 93% to 94% at 800 °C. Meanwhile, the H_2/CO ratio increased from 0.98 to 1.38 at 700 °C and from 0.96 to 1.36 at 800 °C. However, the CO_2 conversion firstly decreased with the decreasing of CO_2/O_2 from 1/0 to 0.5/0.25 and then increased with the decreasing of CO_2/O_2. This is because that methane dry reforming and methane partial oxidation reaction reached the balance state according to its chemical equation when the molar ratio of CO_2/O_2 equal to 0.5/0.25.

The catalytic activity stability of Ni-MA with time on stream at 750 °C is shown in Figure 3.8. For the single methane dry reforming reaction, the catalytic activity of Ni-MA is decreased slightly after 100 h reaction. The conversions of CO_2 and CH_4 are decreased about 3.5%. Compared with the single methane dry reforming reaction, the conversions of CO_2 and CH_4 are kept almost unchanged during all 100h reaction period under

combined methane dry reforming with methane partial oxidation reaction with CH_4: CO_2: O_2=1: 0.5: 0.25.

The carbon deposition is an important factor, which affects the catalytic performance on methane dry reforming reaction. The different carbon type creates different influence on catalytic performance. The different carbon structure is usually identified by Raman analysis. In order to analyze the influence from methane partial oxidation on the methane dry reforming, the used Ni-MA in single methane dry reforming under the same conditions was prepared in this paper. The Raman spectra of spent Ni-MA from different reaction after 100h reaction are compared in Figure 3.9. For single dry reforming reaction, two weak peaks appeared at 1350 cm^{-1} and 1580 cm^{-1} corresponding to the D band and G band, respectively. The D band and G band are characteristic bands of regular-structure carbon, indicating that regular structure carbon is formed on the surface of Ni-MA during single dry reforming reaction. Compared with single dry reforming reaction, it can be observed that no peak appeared in the spectra of used Ni-MA when the reactant gas contained oxygen, indicating that it was less likely to form regular structure carbon on the catalyst in the process of combined methane partial oxidation and methane dry reforming reaction.

The images of used Ni-MA catalyst in different conditions are exhibited in Figure 3.10. It can be observed that the Ni-MA still kept the structure as fresh catalyst. Unlike the morphology of reaction in single methane dry reforming which had some carbon nanotubes on its surface (Figure 3.10a), the morphology of reaction in combined reaction presented amorphous carbon (Figure 3.10b) which could be easily converted into product during the reaction [35,36].

In addition, catalytic performances over spinel-like catalysts prepared from different

method were also evaluated (Figure 3.11 and Figure 3.12). For $NiAl_2O_4$-C catalyst, it present a high conversion for both of CH_4 and CO_2 than those of $NiAl_2O_4$-P, meaning one-step EISA method is a promising alternative way for efficient catalyst preparation. Meanwhile, the spinel-like structure catalyst with Pt incorporation (Pt-$NiAl_2O_4$-C) shows a benign performance. It is worth noting that catalysts in this chapter can be divided into catalysts prepared by one-step method (EISA method) and catalysts prepared by two-step method. Different from the two-step method (Impregnation method), the one-step method shows a more convenient preparation process. At the same time, the catalyst has better performance, which provides a good concept for the design of efficient catalyst

3.4. Conclusions

Mesoporous Ni-MA catalyst was prepared by one-step EISA method and possessed strong interaction between nickel species and support γ-alumina and large exposed metal surface area. The catalysts had better catalytic performance for combined DRM and POM reaction, ascribing to the larger exposed metal Ni surface area of Ni-MA than that of Ni/MA. The high reaction temperature was beneficial to conversion of reactants and resulted in decreasing of H_2/CO molar ratio. The conversion of methane and the molar ratio of H_2/CO presented an increasing tendency with the decrease of CO_2/O_2 molar ratio under different reaction temperatures. The catalytic performance remained stable at 750 °C for 100 h reaction. The characterization results of used catalysts indicated that combined POM with DRM could effectively suppress carbon deposition. For combined DRM and POM reaction, one is endothermic and the other is exothermic. Obviously, for Ni-MA, the coupling reactions between DRM and POM in the mesoporous channel can facilitate the heat exchange better, therefore the presence of mesoporous channel can also enhance the activity. In addition, EISA method was applied to fabricate a spinel-like

catalyst, presenting an excellent performance than impregnation method. Based the consideration above, high exposed metal surface and excellent heat exchange play crucial role for combined DRM and POM reaction. This strategy provides a promising concept for efficient catalyst preparation.

References

[1] H. Li, Y. He, D. Shen, S. Cheng, J. Wang, H. Liu, C. Xing, S. Shan, C. Lu, R. Yang, Int J Hydrog Energy, 42 (2017) 10844-10853.

[2] X. Huang, G. Xue, C. Wang, N. Zhao, N. Sun, W. Wei, Y. Sun, Cat Sci Technol, 6 (2016) 449-459.

[3] I. Luisetto, C. Sarno, D. De Felicis, C. Battocchio, S. Tuti, S. Licoccia, E. Di Bartolomeo, Fuel Process Technol, 158 (2017) 130-140.

[4] Q. Ma, D. Wang, M. Wu, T. Zhao, Y. Yoneyama, N. Tsubaki, Fuel, 108 (2013) 430-438.

[5] D. Li, M. Lu, S. Xu, C. Chen, Y. Zhan, L. Jiang, Int J Hydrog Energy, 42 (2017) 5063-5071.

[6] Y. Wang, L. Yao, S. Wang, D. Mao, C. Hu, Fuel Process Technol, 169 (2018) 199-206.

[7] P. Djinovic, J. Batista, A. Pintar, Int J Hydrog Energy, 37 (2012) 2699-2707.

[8] M. Nagai, K. Nakahira, Y. Ozawa, Y. Namiki, Y. Suzuki, Chem Eng Sci, 62 (2007) 4998-5000.

[9] Mariana M.V.M. Souza, Donato A.G. Aranda, Martin Schmal, J Catal, 204 (2001) 498-511.

[10] K. Yasin, S. Zahra, B. Farzad, Chem Eng J, 299 (2016) 353-366.

[11] H. Ren, Y. song, W. Wang, Chem Eng J, 259 (2015) 581-593.

[12] J. Zhu, X. Peng, L. Yao, J. Shen, D. Tong, C. Hu, Int J Hydrog Energy, 36 (2011) 7094-7104.

[13] M. Zhang, J. Zhang, Y. Wu, J. Pan, Q. Zhang, Y. Tan, Y. Han, Appl Catal B, 244 (2019) 427-437.

[14] L. Liu, T. Zhao, Q. Ma, Y. Shen, J Nat Gas Chem, 18 (2009) 375-378.

[15] T. Zhao, K. Zhang, X. Chen, Q. Ma, N. Tsubaki, Catal Today, 149 (2010) 98-104.

[16] R. Chai, Z. Zhang, P. Chen, G. Zhao, Y. Liu, Y. Lu, Micro Meso Mater, 253 (2017) 123-128.

[17] J. Xue, L. Chen, Y. Wei, H. Wang, Chem Eng J, 327 (2017) 202-209.

[18] Q. Wei, X. Gao, G. Liu, R. Yang, H. Zhang, G. Yang, Y. Yoneyama, N. Tsubaki, Fuel, 211 (2018) 1-10.

[19] K.M. Kang, I.W. Shim, H.Y. Kwak, Fuel Process Technol, 93 (2012) 105-114.

[20] U. Oemar, K. Hidajat, S. Kawi, Fuel Process Technol, 40 (2015) 12227-12238.

[21] L. Pelletier, Dirkson D.S. Liu, Appl Catal A, 317 (2007) 293-298.

[22] M.P. Kohn, M.J. Castaldi, R.J. Farrauto, Appl Catal B, 94 (2010) 125-133.

[23] U. Oemar, K. Hidajat, S. Kawi, Catal Today, 281 (2017) 276-294.

[24] A.I. Tsyganok, M. Inaba, T. Tsunoda, K. Suzuki, K. Takehira, T. Hayakawa, Appl Catal A, 275 (2004) 149-155.

[25] I.V. Zagaynow, A.S. Loktev, A.L. Arashanova, V.K. Ivanov, A.G. Dedov, I.I. Moiseev, Chem Eng J, 290 (2016) 193-200.

[26] B.V. Ayodele, M.R. Khan, C.K. Cheng, Int J Hydrog Energy, 41 (2016) 198-207.

[27] K. Tao, L. Shi, Q. Ma, D. Wang, C. Zeng, C. Kong, M. Wu, L. Chen, S. Zhou, Y. Hu, N. Tsubaki, Chem Eng J, 221 (2013) 25-31.

[28] D. Mustard, C. Bartholomew, J Catal, 67 (1981) 186-206.

[29] L. Xu, H. Zhao, H. Song, L. Chou, Int J Hydrog Energy, 37 (2012) 7497-7511.

[30] Q. Yuan, A. Yin, C. Luo, L. Sun, Y. Zhang, W. Duan, H. Liu, C. Yan, J Am Chem Soc, 130 (2008) 15210-15216.

[31] W. Wang, S. Stagg-Williamsa, F. Noronhab, L. Mattosb, F. Passosc, Catal Today, 98 (2004) 553-563.

[32] Y. Asencios, E. Assaf, Fuel Process Technol, 106 (2013) 247-252.

[33] A. Tsyganoka, M. Inabab, T. Tsunodab, K. Suzukib, K. Takehirac, T. Hayakawa, Appl Catal A Gen, 275 (2004) 149-155.

[34] B. Nematollah, M. Rezaei, M. Khajenoori, Int J Hydrog Energy, 36 (2011) 2969-2978.

[35] Q. Ma, J. Sun, X. Gao, J. Zhang, T. Zhao, Y. Yoneyama, N. Tsubaki, Cat Sci Technol, 6 (2016) 6542-6550.

[36] N. Wang, X. Yu, K. Shen, W. Chu, W. Qian, Int J Hydrog Energy, 38 (2013) 9718-9731.

Table 3.1 The physicochemical properties of the MA and MA supported catalysts.

samples	BET surface area (m^2/g)	Pore volume (cm^3/g)	Average pore diameter (nm)	Exposed Ni surface area[a] (m^2/g)
MA	310	0.945	12.2	/
Ni-MA	265	0.775	11.7	3.75
Ni/MA	287	0.611	8.43	3.25

[a] calculated by H_2 chemisorption method.

Table 3.2 Effect of O_2/CO_2 ratio on the catalytic performance.

a

NO.	Reaction Temperature	CH_4: CO_2: O_2	Conversion (%)		H_2/CO
		v/v	CH_4	CO_2	
1	700 ºC	1:1:0	68.0	79.2	0.98
2		1: 0.75: 0.125	71.6	72.1	1.12
3		1: 0.5: 0.25	72.8	60.0	1.28
4		1: 0.375: 0.25	80.7	78.8	1.38

b

NO.	Reaction Temperature	CH_4: CO_2: O_2	Conversion (%)		H_2/CO
		v/v	CH_4	CO_2	
1	800 ºC	1:1:0	93.0	93.0	0.96
2		1: 0.75: 0.125	93.0	91.0	1.08
3		1: 0.5: 0.25	94.0	89.0	1.21
4		1: 0.375: 0.25	94.0	90.0	1.36

Reaction conditions: CH_4 W/F=1 g h/mol, atmospheric pressure

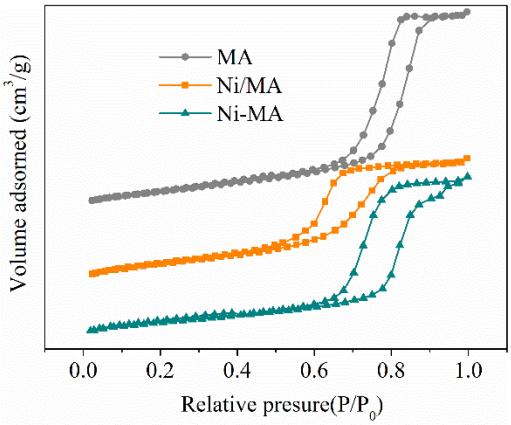

Figure 3.1 N_2 adsorption-desorption isotherms of different catalysts.

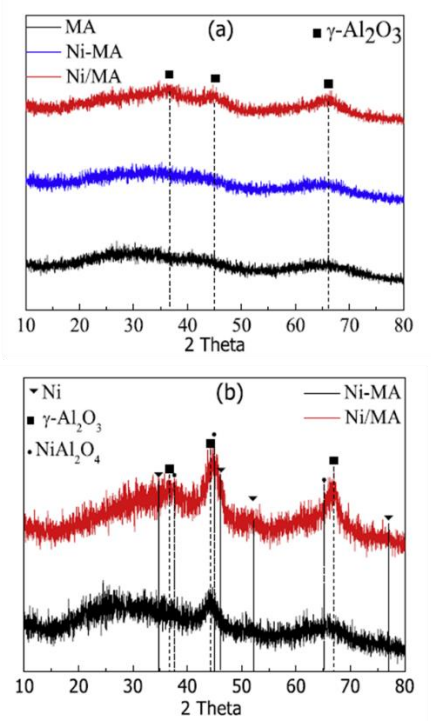

Figure 3.2 XRD patterns of Ni/MA and Ni-MA (a) before reduction (b) after reduction.

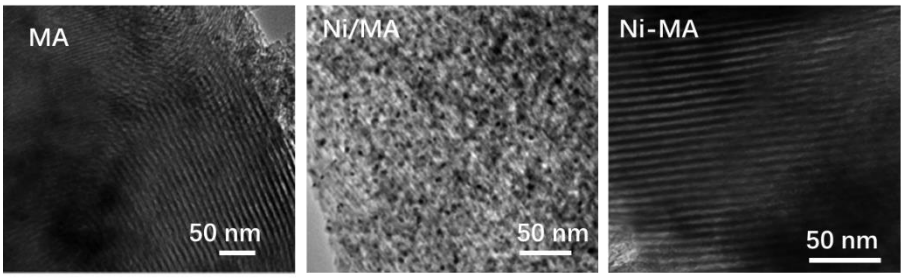

Figure 3.3 TEM images of different samples.

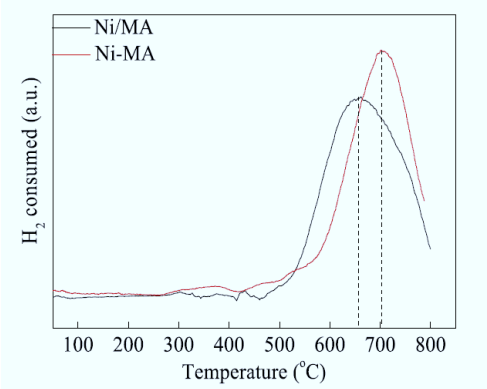

Figure 3.4 H_2-TPR curves of different catalysts.

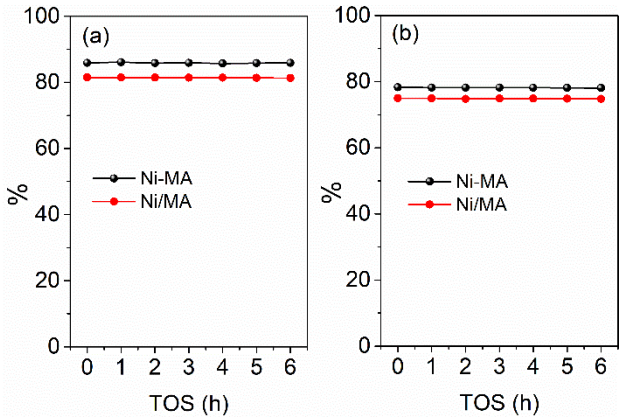

Figure 3.5 CH_4 (a) and CO_2 conversion (b) with time over Ni-MA and Ni/MA. (Reaction conditions: W/F (CH_4) = 1 g h mol^{-1}, 750 °C, CH_4: CO_2: O_2=1:0.5:0.25.)

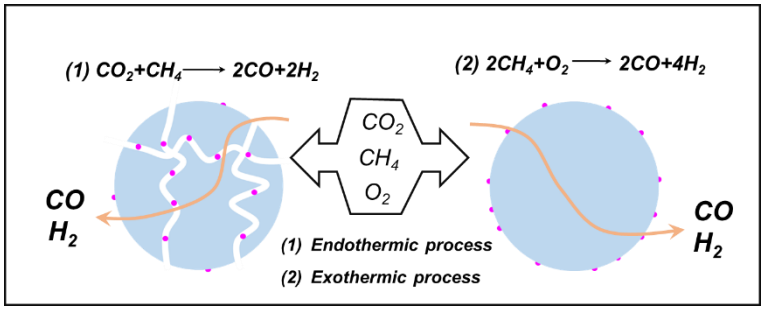

Figure 3.6 Influence of channel structure on catalytic processes.

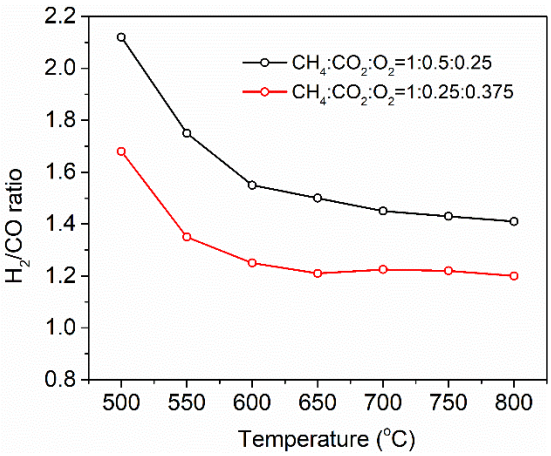

Figure 3.7 Influence of reaction temperature on H_2/CO ratio. (Reaction conditions: W/F (CH_4) = 1 g h mol^{-1})

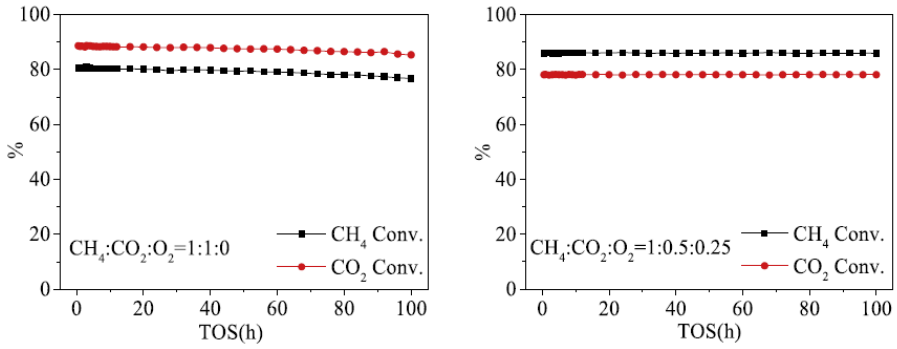

Figure 3.8 Catalytic stability of Ni-MA (Reaction conditions: 750 °C, W/F (CH_4) = 1 g h mol^{-1}).

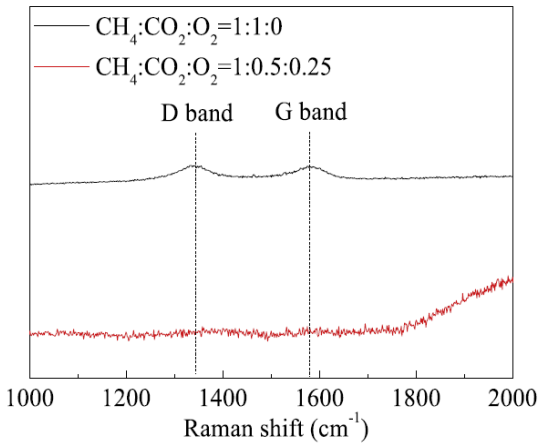

Figure 3.9 Raman spectra of used Ni-MA.

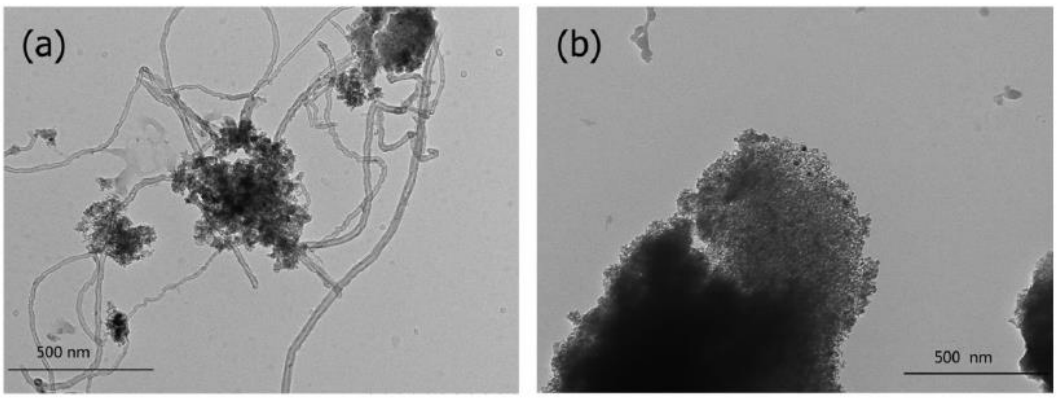

Figure 3.10 TEM images of used Ni-MA after 100 h reaction (a) after single DRM reaction (b) after combined DRM and POM reaction.

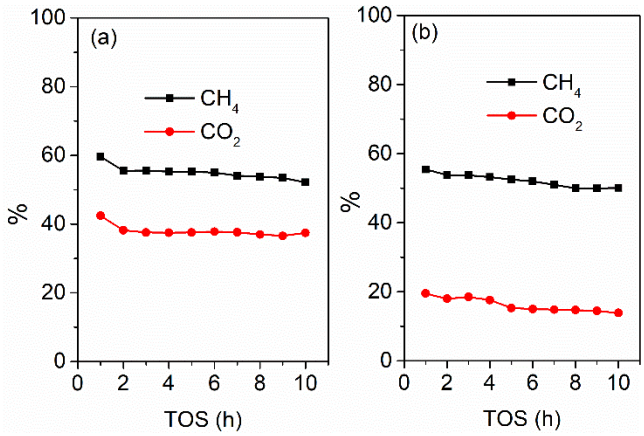

Figure 3.11 CH_4 and CO_2 conversion with time over $NiAl_2O_4$-C and $NiAl_2O_4$-P. (Reaction conditions: W/F (CH_4) = 1 g h mol^{-1}, 650 °C, CH_4: CO_2: O_2=1:0.5:0.25.)

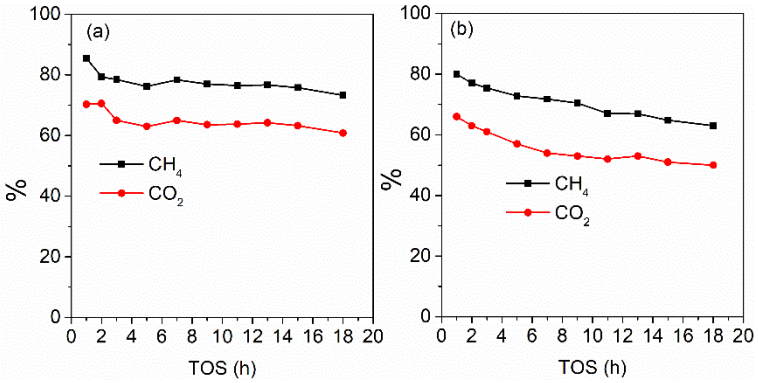

Figure 3.12 CH_4 and CO_2 conversion with time over Pt-$NiAl_2O_4$-C and Pt-$NiAl_2O_4$-P. (Reaction conditions: W/F (CH_4) = 1 g h mol^{-1}, 750 °C, CH_4: CO_2: O_2=1:0.5:0.25.)

Chapter 4

Directly converting carbon dioxide to linear α-olefins on bio-promoted catalysts

A carbon dioxide hydrogenation to olefin process that achieves 72% selectivity for alkenes and 50.3% selectivity for C_{4-18} alkenes, of which formation of linear α-olefins accounts for 80%. The process is catalyzed by carbon-supported iron, commonly used in C-C coupling reactions, with multiple alkali promoters extracted from corncob.

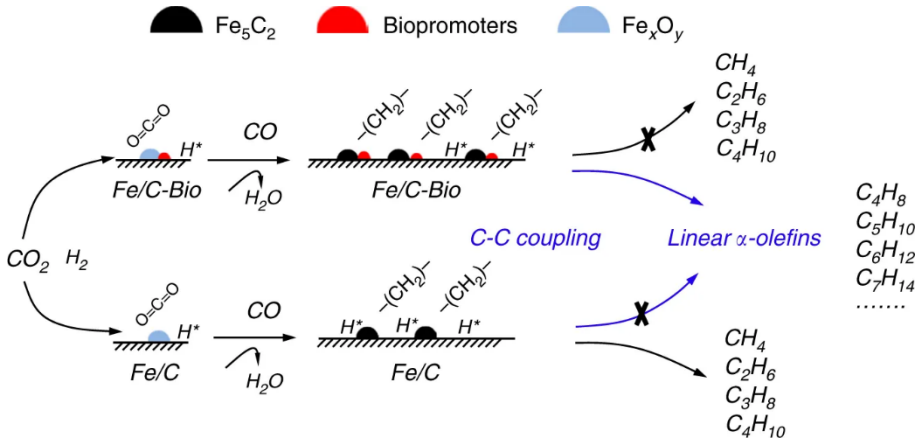

Abstract

Although considerable efforts have been made in converting carbon dioxide to hydrocarbons via hydrogenation processes, precise control of C-C coupling towards heavy olefins remains a challenge. Here we report a carbon dioxide hydrogenation to olefin process that achieves 72% selectivity for alkenes and 50.3% selectivity for $C_{4–18}$ alkenes, of which formation of linear α-olefins accounts for 80%. The process is catalyzed by carbon-supported iron, commonly used in C-C coupling reactions, with multiple alkali promoters extracted from corncob. The design is based on the synergistic catalysis of mineral elements in biomass enzyme on which carbon dioxide can be directly converted into carbohydrate. The mineral elements from corncob may promote the surface enrichment of potassium, suppressing the secondary hydrogenation of alkenes on active sites. Furthermore, carburization of iron species is enhanced to form more Fe_5C_2 species, promoting both the reverse water–gas shift reaction and subsequent C-C coupling.

Keyword: CO_2 hydrogenation; Linear α-olefins; Biopromoters; Alkali metal, Iron catalyst

4.1. Introduction

Converting carbon dioxide (CO_2) to valuable commodity chemicals is a potential route to mitigate the detrimental effects associated with anthropogenic CO_2 emissions, and may benefit energy carrier technology and chemical production [1, 2]. Among common CO_2 transformation pathways comprising photocatalytic conversion, electrochemical reduction, catalytic hydrogenation, and other related processes, CO_2 hydrogenation to hydrocarbons via reverse water-gas shift (RWGS) reaction followed by C-C coupling has been deemed as one of the most promising means of CO_2 utilization over the last two decades [3-5].

Generally, light hydrocarbons with less than four carbon numbers, especially methane, are the major hydrocarbon products in the process of CO_2 hydrogenation. The addition of alkali metal ions to iron catalysts can increase the selectivity for light olefins during CO_2 or CO hydrogenation. The addition of alkali promoters results in a decrease in H_2 adsorption and an increase in CO_2 adsorption, significantly enhancing production of light olefins [6, 7]. It is reported that alkali (K and Na)-promoted Fe-based catalysts exhibit excellent selectivity exceeding 45% for light olefins [8, 9].

In addition to lower olefins, higher olefins and in particular linear α-olefins (LAOs), which contain a terminal carbon–carbon double bond, are important and expensive industrial feedstocks for producing highly value-added chemicals, such as lubricants, detergents, and polyolefins [10, 11]. Currently, heavy α-olefins with carbon number higher than four are generally produced via oligomerization of ethylene mostly produced from petroleum resources [12-14]. Recently, Zhai et al. reported a Na and Zn modified Fe_5C_2 catalyst applied to Fischer–Tropsch synthesis (FTS) which delivered high selectivity for C_{5+} alkenes and particularly LAO [15]. No related reports concerning LAO

production from CO_2 have been reported to our knowledge, in spite of the fact that CO_2 conversion to heavy hydrocarbons has been demonstrated in recent years [16-18].

Precise control of carbon chain growth to achieve a high selectivity for heavy hydrocarbons with a desired carbon range or bonding pattern (saturated, unsaturated, branched, etc.) remains a severe challenge that limits selective conversion of CO_2. In contrast to CO hydrogenation, CO_2 as a thermodynamically stable molecule needs an initial reduction to a CO intermediate and then subsequent C-C coupling. This requires active sites matching both RWGS and C-C coupling. Thus, these challenges make CO_2 hydrogenation to heavy hydrocarbons more difficult than FTS. Very recently, two multifunctional catalysts (Na-Fe_3O_4/HZSM-5 and In_2O_3/HZSM-5) were reported, which can selectively convert CO_2 to gasoline-ranged hydrocarbons with selectivity of more than 78% in all hydrocarbons [19, 20].

CO_2 in nature can be efficiently converted into carbohydrates via biological photosynthesis over enzymes in biomass. Biomass as a renewable resource contains many mineral elements, such as K, Mg, Ca, and Si, which are involved in carbohydrate synthesis from CO_2 conversion. Such mineral elements in biomass form an optimal composition ratio match with the evolution of plants, and promote enzymes to exhibit high-performance biocatalysis. The introduction of mineral elements from biomass, i.e. corncob (CC), is a promising alternative to the use of chemical promoter sources. These environmental friendly resources have been named as biopromoters [21]. Herein, we design an enzyme-like integrated catalyst comprising iron carbides and alkali promoters from calcined CC ash, accomplishing direct conversion of CO_2 hydrogenation into LAO with a selectivity in hydrocarbons of higher than 40% and a total olefin selectivity in hydrocarbons of 72%. In this "CO_2-LAO" reaction the product selectivity approached

that of FTS [15]. Compared to unpromoted and chemically promoted iron-based catalysts, the biopromoter modified iron catalysts are demonstrated to have a synergetic effect for improving the performance of CO_2 hydrogenation.

4.2. Experimental

4.2.1 Catalyst Preparation

To attain mineral element-rich powder, corncob (CC) was calcined under 500 ºC and remains 180 min in flowing air. The element content of pretreated CC ash was shown in Table 4.1. As for the preparation of Fe/C, glucose and iron nitrate was dispersed in the de-ion water solution. After vigorous stirring of 1 h, the derived turbid liquid was transferred into a 100 mL capacity Teflon-lined stainless-steel autoclave, followed by one-pot hydrothermal treatment at 150 ºC for 24 h. Obtained products were washed and filtered off for 5 times with distilled water and ethanol successively. Finally, products were dried in crucibles at 120 ºC overnight, denoted as Fe/C.

The promoter(s)-modified Fe/C catalysts were fabricated by simple physical mixing the corresponding promoter(s) and Fe/C powder. The raw material for each promoter in the promoted Fe/C catalyst is KCl, MgO, $CaCO_3$ and SiO_2. Fe/C-K, Fe/C-Mg, Fe/C-Ca and Fe/C-Si catalysts just contain single corresponding chemical promoter; Fe/C-Chem catalysts contain four chemical promoters; Fe/C-Bio stands for biopromoters-modified Fe/C catalysts. The addition of each chemical element is equal to the value existed in the content of biopromoters-modified Fe/C-Bio. For example, Fe/C-Bio was fabricated via physical mixing 0.15g prepared CC ash and 1.0g Fe/C powder, following pelleting the mixtures with a 20 ~ 40 mesh size.

To remove the soluble KCl existed in biopromoters, 0.15g biopromoters were

washed for 5 times with 1.5L deionized water for 10 h (noted as CC-W). The pretreated CC-W was mixed with Fe/C and marked as Fe/C-Bio-W. As for the Fe/C-K, Ca, Mg, S catalyst, the introduction form of S element was iron sulfate ($FeSO_4$).

4.2.2 Catalyst characterization

The element content of pretreated CC ash was tested by a Philips Magix-601 wave-dispersive X-Ray Fluorescence (WD-XRF) and a PerkinElmer 7300DV Inductively Coupled Plasma Optical Emission Spectrometer (ICP-OES). X-ray diffraction (XRD) spectra were obtained on a PANalytical X'pert Pro diffractometer equipped with Cu-Kα (40 kV, 40 mA) irradiation. Scanning electron microscopy (SEM) images were taken by a JSM-7800F microscope operated at an accelerating voltage of 1.5 kV, which were used to obtain the surface morphology and elemental composition of the prepared catalysts. Scanning electron microscopy with dispersive spectroscopy (SEM-EDS) was used to attain the elemental maps.

Transmission electron microscope (TEM) images were obtained by using a JEOL JEM-2000EX (120 kV) microscope. The X-ray photoelectron spectroscopy (XPS) measurements were conducted on an ESCALAB 250Xi equipped with Al Kα radiation. The ^{57}Fe Mössbauer spectra (MES) of the catalysts were recorded at room temperature using a Topologic 500A spectrometer and a proportional counter. ^{57}Co (Rh) moving in a constant acceleration mode was used as a radioactive source. Magnetic hyperfine field was calibrated with the 330-kOe field of α-Fe at ambient temperature.

The hydrogen temperature-programmed reduction (H_2-TPR) experiments were carried out in a home-made apparatus. A 10 mg of sample was in situ treated by an Ar stream (30 ml·min^{-1}) at 400 °C for 30 min. After cooling down to room temperature, the sample was heated to 1000 °C with a temperature ramp of 10 °C·min^{-1} in a 5% H_2 / 95%

Ar flow (30 ml·min^{-1}). The hydrogen concentration in the effluent was continuously monitored by a TCD detector.

4.2.3 Catalytic performance test

The prepared catalysts were in situ reduced at 400 ºC for 10 h using H_2 (40 mL/min, atmospheric pressure) prior to CO_2 hydrogenation tests. Briefly, CO_2 hydrogenation reaction was performed with a continuous flowing fixed-bed reactor from feed gas (CO_2: 24 v %, H_2: 72 v %, N_2: 4 v %). An ice trap of n-octane as solvent was equipped to capture the heavy hydrocarbons in the effluent. Reaction conditions were 320°C, 1.0MPa, and W/F = 10 g·h·mol^{-1}. Gas products were analyzed by two on-line gas chromatographs, one of which employed an active charcoal column equipped with a thermal conductivity detector (Shimadzu, GC-8A). Another used a capillary column and a flame ionization detector (Agilent Technologies, 7890A) to analyze light hydrocarbons. Liquid products from the ice trap were analyzed by an off-line gas chromatograph using a flame ionization detector (Agilent Technologies, 7890A).

4.3. Results and discussion

4.3.1 Structure and surface properties of catalysts

The corresponding contents of K, Mg, Ca and Si in the prepared CC ash were 22.8 wt%, 21.8 wt%, 7.2 wt% and 2.1 wt%, respectively, and the remaining elements were O and other trace elements accounting for 46.1 wt% (Table 4.1). The main phases of K, Mg, Ca and Si are ascribed to KCl, MgO, $CaCO_3$ and SiO_2, respectively (Figure. 4.1). The single mineral promoter, simulated four promoters and biopromoters were added into Fe/C catalyst by a facile physical mixing method, marked as Fe/C-M, Fe/C-Chem and Fe/C-Bio respectively, and the loading of iron in these catalysts ranged from to 14.0% to

16.4% (Table 4.2). The morphology of fresh Fe/C-Bio existed in the form of spherical structure with a diameter of 3-5 μm, and Fe, K, Ca and Mg promoters were uniformly distributed in the catalyst system (Figure 4.2). Carbonaceous spheres as promising supports possess excellent features, such as facilitated the formation of iron carbides during H_2 activation and suppressed the aggregation of nanoparticles during reaction processes [22, 23].

X-ray diffraction (XRD) measurements were used to determine the species phases of catalysts. According to the characteristic diffraction peaks data of KCl (JCPDS, 41-1476), XRD pattern of Fe/C-Bio and Fe/C-Chem shows the existence of K promoter (Figure 4.3). The diffraction patterns of MgO and $CaCO_3$ were not detected in Fe/C-Bio owing to the low content in the catalysts. Other than used Fe/C and Fe/C-Chem, additional peaks of Fe_5C_2 were clearly observed in the used Fe/C-Bio, indicating more Fe_5C_2 formation with the addition of biopromoters. Besides, the peaks of Fe_5C_2 can be also obviously distinguished after 100h reaction. The existence of more Fe_5C_2 is beneficial to the enhancement of C-C coupling and suppressing of methane formation [27, 28]. Finally, iron oxides and iron carbides will achieve well matching of reverse water-gas shift reaction (equation (1)) and subsequent C-C coupling (equation (2)), improving the activity of CO_2 hydrogenation as well as the selectivity of heavy hydrocarbons.

$$CO_2 + H_2 \rightarrow CO + H_2O \qquad (1)$$

$$CO + 2H_2 \rightarrow -CH_2- + H_2O \qquad (2)$$

For the used Fe/C, the main phases were Fe and Fe_3O_4 rather than Fe_5C_2, showing an inferior selectivity of heavy hydrocarbons. Fe^0 and Fe_3O_4 existed in Fe/C-Chem were also main phases, and presented a higher selectivity of alkenes compared to Fe/C owing to the promotion effect of alkali metal.

Transmission electron microscope (TEM) was applied to determine the distribution and size of iron species (Figure 4.4). After reaction, Fe/C-Bio exhibited uniform particles distribution of iron species while fresh Fe/C-Bio consisted of irregular large particles. The precursor of iron species contains a large number of humboldtine ($FeC_2O_4 \cdot 2H_2O$, JCPDS 23-0293) in carbonaceous spheres (Figure 4.5) [21]. The decomposition of humboldtine under H_2 condition presented magnetite, iron carbides and metal Fe [29]. The decomposed metal Fe acts with CO_2 and H_2 to form active sites of RWGS and C-C coupling, then converts CO_2 and H_2 into hydrocarbons [1]. Therefore, no additional calcination is needed in our work, which is different from conventional preparation processes.

The difference between structure shape and size of iron particles result from humboldtine decomposition and subsequent reaction with CO_2 and H_2. The statistical result of particles shows that Fe/C-Bio particle size mainly distributed on the range of 5-9 nm, which is beneficial to maintain a low CH_4 selectivity and high light olefins selectivity for CO hydrogenation due to the reported particle size effect [30]. However, the particle size distribution of used Fe/C-Chem was centered on 11-15 nm, which is much larger than that of Fe/C-Bio. Well size distribution of particles is vital for the activity and selectivity of catalytic performance, thus small average particle size change of iron species from 7 to 9 nm is favorable for maintaining the catalytic performance of catalyst during stability test (Figure 4.2c and Figure 4.6). Besides particle size, the main active phases are different between Fe/C-Chem and Fe/C-Bio as further verified by high-resolution TEM (HR-TEM). Fe_5C_2 was detected as main active phase for Fe/C-Bio (Figure 4.4f) while Fe_3O_4 was present for Fe/C-Chem (Figure 4.4e), well consistent with XRD analysis. In Figure 4.4b, iron species of Fe/C-Chem presented a core-shell structure,

and the core of Fe_3O_4 and Fe was encapsulated by a shell of amorphous carbon [31]. As for Fe/C-Bio, iron species were mainly isolated Fe_5C_2 nanoparticles without similar core-shell structure. These findings indicate that biopromoters are conducive to the carburization of Fe_3O_4 and Fe core with amorphous carbon shell, producing small particles of active phases and providing more contact interfaces between active sites and feed gas.

Fe species in these promoted catalysts are more easily reduced. In Figure 4.7, the H_2-TPR curves of Fe/C, Fe/C-Bio and Fe/C-Chem are presented. In heating conditions under a H_2 atmosphere, the decomposition of humboldtine, a precursor for active iron species prepared by the hydrothermal process, will produces magnetite, iron carbides and metal Fe with an obvious H_2 consumption peak (450 ºC for Fe/C) in the H_2-TPR curve. After promoter is introduced in the Fe/C catalyst, the H_2 reduction process is clearly enhanced in terms of the peak shift towards a low temperature (404 ºC for Fe/C-Chem and 424 ºC for Fe/C-Bio), suggesting the promotional effect on the decomposition of humboldtine of the electronic promoters (K, Mg, Ca). Totally, the reduction process with H_2 at 400ºC before reactions is enhanced on bio- and chem-promoted catalysts.

The ^{57}Fe Mössbauer spectra of the catalysts in Figure 4.8 further disclose the formation and transformation of active phases in the various stages from fresh, reduced, to used catalysts. The detailed composition and comparison of different phases are also listed in Table 4.3 and Figure 4.9. As indicated above, iron species in the fresh Fe/C-Bio are present in terms of humboldtine. After reduction at 400 ºC in hydrogen, the Fe/C catalyst without promoters is composed of metal iron (76%), χ-Fe_5C_2 (8.7%) and super-paramagnetism (spm) Fe^{3+} (15.3%). More interestingly, the composition is greatly changed after biopromoters are physically introduced in the catalyst. The content of χ-

Fe_5C_2 reaches as high as 64.5%, accompanied by a sharply decrease of metal iron to 9.8%, demonstrating an obviously promotional effect of biopromoters on the carbonization of iron in the reduction process. The content of χ-Fe_5C_2 further climbes to a higher value of 87.2%, while no metal iron is observed in the Fe/C-Bio catalyst after reaction, suggesting that the metal iron is further carbonized after exposing in the atmosphere of CO_2 and H_2 as feedstocks.

In comparison, the content of χ-Fe_5C_2 for the used Fe/C catalyst with chemical promoters is only 34.1%, and a large amount of metal iron (30.1%) cannot be completely carbonized in the catalyst. These findings clearly show that the superiority of biopromoters in promoting the formation of iron carbides as compared to chemical promoters, and the above promotional effect primarily occurs in the reduction process prior to catalytic reactions. In spite of similar chemical composition for the Fe/C catalysts with chemical and biological promoters, the unique synergistic catalytic role probably exists in the bio-promoted catalyst.

X-ray photoelectron spectroscopy (XPS) was applied to investigate the phase composition and content of surface species. The binding energy peaks at 711.4, 710.3 and 708.5 eV in the Fe2p spectrum are correspondingly ascribed to Fe^{III}, Fe^{II} and Fe-C (Figure 4.10a) [32]. As for C1s spectrum, the binding energy peaks ca. 281.0, 282.0 and 284.8eV are correspondingly contributed to C-Fe, C=C and C-C bonds (Figure 4.10b) [21]. Clearly, the content of Fe-C in the Fe2p spectrum is significantly enhanced with the addition of biopromoters, in accordance with that of C-Fe suggested in the C1s spectrum, further indicating the existence of biopromoters aggravates the carbonization process of iron species. The calculated surface content of iron carbides on the used Fe/C-Bio catalyst is increased to 48% from 19% for the reduced catalyst. Both contents are lower than those

from the previous MES analysis, reflecting that the iron carbides are more favorable to be formed on catalyst bulk.

More importantly, it is necessary to study the content of K and carbides in catalysts surface in view of the fact that K influences the olefins hydrogenation as well as carbides affects the selectivity of heavy hydrocarbons. According to the results of XPS surface analysis, the surface atom ratio of K/Fe in the reduced Fe/C-Bio reaches 1.4, far higher than its stoichiometry in bulk (0.3), and the value further climbs to as high as 2.7 after reaction, nearly double of that before reaction, suggesting the obvious K enrichment on catalyst surface in the reduction and reaction process [33, 34]. Simultaneously, the K content in bulk of the fresh, used for 6 h and used for 100 h Fe/C-Bio catalyst is not obviously changed a lot (Table 4.2 & 4.4).

However, the surface K/Fe ratio in the used Fe/C-Chem catalyst is merely 0.4, close to the theoretical value. K was more easily to be enriched on the surface of the bio-promoted catalyst rather than chemical-promoted catalysts. It seems that K in biopromoters has stronger migration ability than chemical promoters, probably resulting from the unique synergistic effect between K with other elements. This synergistic effect may be due to more favorable interactions between potassium promoters and other elements, or to other trace metal elements enhancing potassium migration ability. The migration ability could improve its contact interface between active phases and electronic promoter.

A relationship between the surface K/Fe ratio and the content of iron carbides can be accordingly established as shown in Figure 4.10c. Under the experiment conditions in this work, the content of iron carbides gradually increase with the increase of the surface K/Fe ratio. However, there must be an optimized value for the surface K/Fe ratio as the

excessive K may cover the active iron sites. In our case, surface enriched K sharply promotes the formation of more carbides than unpromoted and chemical promoted ones, which is in accordance with XRD patterns, MES analysis, XPS spectra as well as other reports [35]. In addition, the carbides content from XPS for the used Fe/C-Chem is almost unchanged compared with the used Fe/C, suggesting surface enriched K is more effective than bulk dispersed K. The vast amount of carbides produces higher α value, improving chain growth probability.

It is imperative to investigate the secondary hydrogenation ability of olefins, which severely influence olefin selectivity in hydrocarbons, thus the in-situ pulse experiments of propene over reacted Fe/C, Fe/C-Chem and Fe/C-Bio catalysts were further employed. Figure 4.11 shows that more propene was converted into propane on the unpromoted Fe/C compared to the case of Fe/C-Bio and Fe/C-Chem when isometric propene was pulsed into the reactor. It indicates the addition of promoters will suppress the hydrogenation of olefins, and biopromoters-modified iron catalyst shows higher habitation ability towards olefins hydrogenation than chemical promoters. As shown in Table 4.5, the selectivity of olefins over Fe/C-Bio (72 %) is the highest, followed by Fe/C-Chem (53.1 %), and Fe/C presented an inferior selectivity of olefins (21.2 %), which is in accordance with the results of pulse experiments.

Linear α-olefins are known to be the primary intermediates of C-C coupling. After LAO are formed, they can reabsorb on the active sites and undergo secondary reactions. Weaker hydrogenation ability of olefins over Fe/C-Bio is beneficial to the production of α-olefins. Ethylene, propylene, and α-olefins with low carbon number undergo oligomerization reactions over carbides to form more long-chain linear α-olefins. A well match between the high activity of C-C coupling and weak hydrogenation ability is

responsible for the excellent catalytic performance with a high C_{4-18} alkenes selectivity of 50.3% as well as 80% LAO in C_{4-18} alkenes. The detailed reaction scheme in combination with experimental and characterization results were depicted in Figure 4.12. Thus, it is possible to tune the selectivity of linear olefins by changing the activity of C-C coupling and hydrogenation ability of active sites. Although the addition of chemical promoters weakens the secondary hydrogenation reaction as well, it does not sharply raise the content of carbides on catalyst surface as well as the interface between carbides and promoters. Therefore, the catalytic performance via biopromoters addition cannot be completely simulated by a chemical addition route of multiple promoters. Enough content of carbides and weak alkenes hydrogenation ability are indispensable for heavy olefins formation.

It is noteworthy that the formation of enough content of carbides in the H_2 reduction stage prior to catalytic reactions is more important to achieve superior performance in LAO production reactions instead of the in-situ carbonization process, as reflected by the carbides content from the previous characterization analysis. The similar superior performance in LAO production with CO and H_2 as feedstocks (Table 4.6) also demonstrates it. In an additional case for comparison, the bare Fe catalyst is prepared without glucose in raw materials under the same hydrothermal conditions as Fe/C. Therefore, no iron carbides are formed in this bare Fe catalyst after the pretreatment under the same H_2 reduction condition as others. However, it shows the lowest conversion and LAO selectivity among all self-made iron-based catalysts.

4.3.2 Catalytic performance

The performance of CO_2 hydrogenation on prepared catalysts with suitable additive amount was evaluated under optimal reaction conditions (Table 4.5 and Figure 4.13). C_{4-}

$_{18}$ alkenes selectivity was sharply increased from 11.6% to 50.3%, and methane selectivity was suppressed simultaneously from 39.2% to 11.8% when biopromoters were added into the Fe/C catalyst. It is noteworthy that LAO selectivity accounts for 80% in C_{4-18} alkenes and LAO is mainly concentrated on the carbon number range of 4 to 9, which is beneficial to the production of lubricating oil and plasticizer. Compared to the selectivity of C_{4-18} alkenes over conventional iron-based catalysts, the C_{4-18} alkenes selectivity over biopromoters modified iron catalysts reaches maximum value in reported literatures (Table 4.7). Besides that, all the Fe/C, bio-promoted and chem-promoted Fe/C catalysts show stable catalytic performance in a 6 h reaction (Figure 4.14). A long-time stability test of 100h for the Fe/C-Bio shows that the conversion of CO_2 remains unchanged, as well as the selectivity to CH_4, C_{5+} and LAO (Figure 4.6), therefore it indicates that bio-promoted iron-based catalysts are stable and efficient for heavy olefins production especially for LAO. More interestingly, we also find similar results after replacing the feedstock from the mixture of CO_2 and H_2 by that of CO and H_2 (Table 4.6). After biopromoters are physically introduced, the CO conversion and LAO selectivity in C_{4-18} alkenes is both evidently promoted to 85% (vs 49% for the Fe/C) and 67% (vs 41% for the Fe/C) under the same catalytic conditions (280 ^{o}C, 1.0 MPa, H_2/CO = 1:1), respectively. Furthermore, a very high total olefin selectivity of 78.4% as well as a high conversion of 95% is observed after the temperature is lifted to 320 ^{o}C, which is the same temperature as CO_2 hydrogenation.

To verify the biopromoter effect and explain the superior selectivity of linear olefins, each separated promoter addition experiment was also carried out (Table 4.5). The CO_2-LAO performance was improved when the K, Mg, Ca was alone added to unpromoted Fe/C, among which the promotional effect of K was most obvious in terms of enhancing

olefins selectivity (21.2% to 60.4%). The potassium promoter not only is beneficial to the RWGS reaction (enhanced CO_2 conversion) but also enhances selective C-C coupling to olefin (enhanced heavy olefin selectivity). As for the effect of potassium promoter, it is generally believed that the improved surface adsorption property of H_2*/CO_2* and carbide content are the main reasons for the activity improvement. Therefore, potassium-modified iron catalyst showed the highest activity (28.0%) and high-carbon hydrocarbon selectivity (30.5%) among all single promoter (Ca, Mg, and Si) addition experiments.

Unlike the catalyst modified by chemical promoters, the catalyst modified by biopromoters has more small size carbide particles (Figure 4.4), which is important for improving CO_2 hydrogenation activity and maintaining high activity. Accordingly, the catalyst driven by biopromoters showed high catalytic activity (31.0%) among these catalysts. In particular after 100 hours of stable reaction, the catalyst remained at a small particle size (Figure 4.4i, 9.0 nm). In addition, the iron catalyst modified by biopromoters can also form more carbides during the reduction process than chemical promoters modified one (Figure 4.8, 4.9 and 4.10). Combined with the XPS spectra, it can be further found that the basic metal potassium from the biopromoters has a higher migration ability and can form a good interaction interface with the iron species on the catalyst surface. The high content of surface basic promoters (especially K^+) also helps to increase the concentration of acidic CO_2 molecules and promote the growth of carbon chain. More importantly, through *in situ* pulse experiment, it was found that the Fe-based catalyst modified by biopromoters had the weakest olefins hydrogenation ability compared with Fe/C and Fe/C-Chem, thus showing high olefins selectivity (72.0%). Considering that the promoters are introduced by physical mixing method, the influence of the fresh catalyst structure on the catalytic performance difference can be almost ignored. Obviously, the

changes in the surface composition of these spent catalysts are caused by the promoters. Correspondingly, as for Fe/C-Bio, the high contents of surface carbides and promoters boost the catalytic activity, presenting highest activity (Table 4.5.) Meanwhile, the reduced secondary hydrogenation ability of primary alkenes further significantly increases the heavy olefin selectivity.

To further investigate the effect of K promoter, the biopromoters were washed with deionized water for several times then subsequently added into Fe/C (noted as Fe/C-Bio-W). The content of light hydrocarbons (including C_{1-3}) is increased while CO_2 conversion is decreased after soluble KCl was removed (Table 4.1 & 4.8). It indicates that soluble and insoluble K salts are both essential for improving the selectivity of heavy olefins. In addition, the doping of basic Mg and Ca promoter results in a small increase in terms of higher olefins selectivity. In view of the promoting effect between S and alkali metal, the doping of alkali metals and S element was also tested in reaction conditions (Table 4.9) [24]. The existence of few S element introduced by physical mixing did not improve the olefins selectivity. K as a key ingredient mainly suppresses methanation reaction of CO_2 and increases the activity of C-C coupling [25], and the addition of Mg and Ca also suppresses the formation of methane as well as enhances the selectivity to olefins during the process of C-C coupling [26]. Yet for Fe/C-Chem, C_{4-18} alkenes selectivity is only half of those on Fe/C-Bio. These findings indicate that the higher selectivity of C_{4-18} alkenes obtained from Fe/C-Bio is difficult to be simulated by the doping of chemical promoters, suggesting that biopromoters, rather than chemical promoters, induce unique synergistic promoting effect.

4.4. Conclusions

In summary, although the addition of K promoter from chemicals suppressed the

alkenes hydrogenation, the activity of C-C coupling is lower than that for Fe/C-Bio owing to the lack of enough content of carbides. K in biopromoters shows stronger migration ability than chemical promoters during CO_2 hydrogenation process. These surface enriched K could obviously promote the formation of carbides and further enhance the activity of C-C coupling. Besides, the surface enriched K suppresses the hydrogenation of alkenes and leads to more formation of alkenes. The optimal content and existing form of mineral elements in biomass is promising for improving the performance of heterogeneous catalytic CO_2 hydrogenation when these promoters were added into iron catalysts. Thus, this design of biopromoters-modified catalyst provides a new strategy for selective hydrogenation of CO_2 into high value-added products, and sheds a light on the rational design of high efficiently catalysts referenced from bio-catalysis in nature.

Reference

[1] M.D. Porosoff, B. Yan, J.G. Chen, Energy Environ Sci, 9 (2016) 62-73.

[2] W. Wang, S. Wang, X. Ma, J. Gong, 40 (2011) 3703-3727.

[3] R.E. Owen, P. Plucinski, D. Mattia, L. Torrente-Murciano, V.P. Ting, M.D. Jones, J CO2 Util, 16 (2016) 97-103.

[4] C.G. Visconti, M. Martinelli, L. Falbo, A. Infantes-Molina, L. Lietti, P. Forzatti, G. Iaquaniello, E. Palo, B. Picutti, F. Brignoli, Appl Catal B-Environ, 200 (2017) 530-542.

[5] L. Xu, Q. Wang, D. Liang, X. Wang, L. Lin, W. Cui, Y. Xu, Appl Catal A-Gen, 173 (1998) 19-25.

[6] R. Satthawong, N. Koizumi, C. Song, P. Prasassarakich, Catal Today, 251 (2015) 34-40.

[7] P.H. Choi, K.W. Jun, S.J. Lee, M.J. Choi, K.W. Lee, Catal Lett, 40 (1996) 115-118.

[8] J. Zhang, S. Lu, X. Su, S. Fan, Q. Ma, T. Zhao, J CO2 Util, 12 (2015) 95-100.

[9] J. Wei, J. Sun, Z. Wen, C. Fang, Q. Ge, H. Xu, Catal Sci Technol, 6 (2016) 4786-4793.

[10] J. Skupinska, Chem Rev, 91 (1991) 613-648.

[11] Y. Lu, Q. Yan, J. Han, B. Cao, J. Street, F. Yu, Fuel, 193 (2017) 369-384.

[12] B.L. Small, M. Brookhart, J Am Chem Soc, 120 (1998) 7143-7144.

[13] W. Keim, Angew Chem Int Ed, 52 (2013) 12492-12496.

[14] C. Li, I. Sayaka, F. Chisato, K. Fujimoto, Appl Catal A-Gen, 509 (2016) 123-129.

[15] P. Zhai, C. Xu, R. Gao, X. Liu, M. Li, W. Li, X. Fu, C. Jia, J. Xie, M. Zhao, X. Wang, Y.-W. Li, Q. Zhang, X.-D. Wen, D. Ma, Angew Chem Int Ed, 55 (2016) 1-7.

[16] R. Satthawong, N. Koizumi, C. Song, P. Prasassarakich, J CO2 Util, 3-4 (2013) 102-106.

[17] R. Satthawong, N. Koizumi, C. Song, P. Prasassarakich, Top Catal, 57 (2013) 588-

594.

[18] Y.H. Choi, Y.J. Jang, H. Park, W.Y. Kim, Y.H. Lee, S.H. Choi, J.S. Lee, Appl Catal B-Environ, 202 (2017) 605-610.

[19] J. Wei, Q. Ge, R. Yao, Z. Wen, C. Fang, L. Guo, H. Xu, J. Sun, Nat Commun, 8 (2017) 15174.

[20] P. Gao, S. Li, X. Bu, S. Dang, Z. Liu, H. Wang, L. Zhong, M. Qiu, C. Yang, J. Cai, W. Wei, Y. Sun, Nat Chem, 9 (2017) 1019-1024.

[21] J. Sun, H. Xu, G. Liu, P. Zhu, R. Fan, Y. Yoneyama, N. Tsubaki, ChemCatChem, 7 (2015) 1642-1645.

[22] G. Yu, B. Sun, Y. Pei, S. Xie, S. Yan, M. Qiao, K. Fan, X. Zhang, B. Zong, J Am Chem Soc, 132 (2010) 935-937.

[23] B. Sun, K. Xu, L. Nguyen, M. Qiao, F.F. Tao, ChemCatChem, 4 (2012) 1498-1511.

[24] H.M.T. Galvis, J.H. Bitter, C.B. Khare, M. Ruitenbeek, A.I. Dugulan, K.P.d. Jong, Science, 335 (2012) 835-838.

[25] M. Amoyal, R. Vidruk-Nehemya, M.V. Landau, M. Herskowitz, J Catal, 348 (2017) 29-39.

[26] A.N. Pour, S.M.K. Shahri, H.R. Bozorgzadeh, Y. Zamani, A. Tavasoli, M.A. Marvast, Appl Catal A-Gen, 348 (2008) 201-208.

[27] T.H. Pham, Y. Qi, J. Yang, X. Duan, G. Qian, X. Zhou, D. Chen, W. Yuan, ACS Catal, 5 (2015) 2203-2208.

[28] J.G. Rivera de la Cruz, M.K. Sabbe, M.-F. Reyniers, J Phys Chem C, 121 (2017) 25052-25063.

[29] V. Carles, P. Alphonse, P. Tailhades, A. Rousset, Thermochim Acta, 334 (1999) 107-113.

[30] H.M.T. Galvis, J.H. Bitter, T. Davidian, M. Ruitenbeek, A.I. Dugulan, K.P.d. Jong, J Am Chem Soc, 134 (2012) 16207-16215.

[31] C. Yang, H. Zhao, Y. Hou, D. Ma, J Am Chem Soc, 134 (2012) 15814-15821.

[32] T. Yamashita, P. Hayes, Appl Surf Sci, 254 (2008) 2441-2449.

[33] P.S.S. Prasad, J.W. Bae, K.-W. Jun, K.-W. Lee, Catal Surv Asia, 12 (2008) 170-183.

[34] J. Li, X. Cheng, C. Zhang, J. Wang, W. Dong, Y. Yang, Y. Li, J Chem Technol Biotechnol, 92 (2017) 1472-1480.

[35] Z. You, W. Deng, Q. Zhang, Y. Wang, Chinese J Catal, 34 (2013) 956-963.

Table 4.1 The element composition of prepared corncob ash.

Material	Composition of element /wt%									
	K	Si	Ca	Mg	O	Cl	Al	Fe	S	others
CC	22.8	21.8	7.2	2.1	27.0	6.8	5.6	3.2	0.8	2.7
CC-W	13.1	24.8	5.7	2.4	41.6	0.3	6.6	3.3	0.1	2.1

Table 4.2 The element composition of as-prepared catalysts.

Catalyst	Composition of element /wt%				
	Fe	K	Si	Ca	Mg
Fe/C	16.4	-	-	-	-
Fe/C-Bio	14.3	3.0	2.8	1.0	0.3
Fe/C-Chem	14.0	2.9	2.8	1.0	0.3

Table 4.3 Detailed Mössbauer parameters of various catalysts.

Catalyst	Assignment	Mössbauer parameters			
		IS (mm/s)	QS (mm/s)	Hhf (kOe)	Spectral contribution
Reduced Fe/C	χ-Fe_5C_2 (III)	0.30	0	334	1.9
	χ-Fe_5C_2 (II)	0.22	0	210	4.3
	χ-Fe_5C_2 (I)	0.15	0	110	2.5
	Fe^{3+}(spm)	0.36	0.83	/	15.3
	Fe^0	0	0	334	76
Reduced Fe/C-Bio	χ-Fe_5C_2 (II)	0.18	0.04	212	40.5
	χ-Fe_5C_2 (I)	0.17	/	204	24.0
	Fe^{3+}(spm)	0.32	0.82	/	25.7
	Fe^0	-0.08	0.09	336	9.8
Used Fe/C-Bio	χ-Fe_5C_2 (III)	0.21	0.04	114	14.6
	χ-Fe_5C_2 (II)	0.26	0.10	217	31.1
	χ-Fe_5C_2 (I)	0.20	0.05	186	41.5
	Fe^{3+}(spm)	0.34	1.08	/	12.8
Used Fe/C-Chem	χ-Fe_5C_2 (II)	0.27	0.11	214	14.5
	χ-Fe_5C_2 (I)	0.21	0.05	185	19.6
	Fe^{3+}(spm)	0.34	1.02	/	22.1
	Fe^0	–0.01	0.02	331	30.1
	Fe_3O_4 (B)	0.67	–0.01	460	9.1
	Fe_3O_4 (A)	0.32	–0.04	491	4.6

Table 4.4 The content of K determined by ICP-OES in various Fe/C-Bio catalysts.

	After 6h reaction	After 100h reaction
K content /wt%	2.5	2.8

Table 4.5 The catalytic performance of CO_2-LAO over various catalysts. [a]

Cat.	Conv. /%	CO sel. /%	Hydrocarbons sel. /%			Alkenes sel. /%		LAO/O[b]	α[c]
			CH_4	C_{2-3}	C_{4-18}	$C_{4-18}^{=}$	$C_{2-18}^{=}$	/%	
Fe/C	25	22.2	39.2	34.4	26.4	11.6	21.2	3.4	0.53
Fe/C-Bio	31	23.2	11.8	24.4	63.8	50.3	72.0	80	0.72
Fe/C-Chem	24	36.2	26.7	39.8	33.5	24.8	53.1	73	0.57
Fe/C-K	28	22.6	24.0	38.1	37.9	30.5	60.4	75	0.53
Fe/C-Ca	25	31.9	29.0	37.0	34.0	13.7	24.3	42	0.55
Fe/C-Mg	26	28.5	33.2	35.2	31.6	14.9	27.0	42	0.56
Fe/C-Si	22	28.0	43.1	36.6	20.3	5.7	12.9	56	0.54

Note. a. All the conversion and selectivity data are collected at a stable 4-6 h on stream. Reaction conditions: 320 °C, 1.0 MPa, H_2/CO_2 = 3:1, W/F=10 g•h•mol^{-1}, Additive amount of biopromoters is 15 wt% (mass ratio of biopromoters to Fe/C); b. the ratio of linear α-$C_{4-18}^{=}$/$C_{4-18}^{=}$, LAO stands for linear α-C_{4-18} alkenes. The additive amount of K, Mg, Ca and Si is equal to that in the Fe/C-Bio; c. The value of α is calculated based on C_{3-10} products.

Table 4.6 The catalytic performance of various catalysts in CO hydrogenation.[a]

Catalyst	Conv. /%	CO_2 Sel. /%	Hydrocarbons Sel. / C-mol %			Alkenes Sel. C-mol %		LAO/O[b] /%
			CH_4	C_{2-3}	C_{4-18}	$C_{4-18}^{=}$	$C_{2-18}^{=}$	
Fe[c]	30	24.8	8.7	21.1	70.2	38.6	48.6	31
Fe/C	49	28.7	9.9	19.9	70.2	43.6	54.9	41
Fe/C-Bio	85	31.6	11.0	21.9	67.2	52.2	68.3	67
Fe/C-Bio[d]	95	40.9	10.7	24.9	64.4	56.3	78.4	67

Note. All the conversion and selectivity data are collected at a stable 4-6 h on stream. a. Reaction conditions: 280 ºC, 1.0 MPa, H_2/CO = 1:1, W/F=10 g•h•mol^{-1}; b. the ratio of linear α-$C_{4-18}^{=}/C_{4-18}^{=}$, LAO stands for linear α-C_{4-18} alkenes; c. The bare Fe catalyst is prepared without glucose in raw materials under the same hydrothermal conditions as Fe/C; d. The reaction temperature is changed to 320 ºC.

Table 4.7.1 Comparison of the catalytic performance in CO_2 hydrogenation in literatures.

Sample	Conv. (%)	CO Sel. (%)	Hydrocarbon Selectivity (%)				Ref.
			CH_4	$C_{2-4}^{=}$	C_{4-18}	$C_{4-18}^{=}$	
$Fe/Co/Mg/Cu/K/Al_2O_3$	30.0	17.0	22.9	<47.0	30.1[a]	N.G.	A
1Fe-1Zn-1K	51.0	6.0	34.9	53.6	3.7[b]	N.G.	B
CAT A	27.2	21.5	28.1	51.8	30.5	29.4	C
$CuFeO_2$	18.1	31.9	3.9	31.3	<56.6	N.G.	D
K/Fe-Cu-Al-O	89.0	1.0	13.0	27.0	43.0[c]	N.G.	E
K-Fe15	45.0	12.5	18.3	42.3	<35.4	<30.0	F
0.05MnFe	30.0	7.7	29.3	<47.9	3.9[d]	<19.2	G
K^+-Fe/ZrO_2	43.0	15.0	18.0	44.0	28.8[e]	19.0[f]	H
Ce/Mn/Fe	38.6	11.5	35.6	N.G.	N.G.	<34.3[g]	I
KMnFe	41.4	11.5	29.4	57.0[h]	N.G.	N.G.	J
FeCe	24.8	21.3	47.9	<50.9	5.7[i]	N.G.	K

Table 4.7.2 Comparison of the catalytic performance in CO_2 hydrogenation in literatures.

Sample	Conv. (%)	CO Sel. (%)	Hydrocarbon Selectivity (%)				Ref.
			CH_4	$C_{2-4}^{=}$	C_{4-18}	$C_{4-18}^{=}$	
FeCe	24.8	21.3	47.9	<50.9	5.7[i]	N.G.	L
Fe/C-Bio	**30.5**	**23.2**	**11.8**	**33.2**	**63.9**	**50.3**	**This work**

Note: a. C_{5-15} products; b. C_{5+} products; c. C_{5+} products; d. C_{6+} products; e. C_{5+} products; f. $C_{5+}^{=}$ products; g. $C_{2+}^{=}$ products; h. $C_{2+}^{=}$ products; i. C_{6-10} products; N.G. means "not given". **A** Sun, J. et al. ACS Catal. 4, 1-8 (2014).; **B** Rodemerck, U. et al. ChemCatChem 5, 1948-1955 (2013)., **C** Zhang, J. et al. J. CO2 Util. 12, 95-100 (2015)., **D** Hu, B. et al. Appl. Catal. B 132-133, 54-61 (2013)., **E** Choi, Y. H. et al. Appl. Catal. B 202, 605-610 (2017)., **F** Landau, M. V. et al. ChemSusChem 7, 785-794 (2014)., **G** Visconti, C. G. et al. Appl. Catal. B 200, 530-542 (2017)., **H** Al-Dossary et al. Appl. Catal. B 165, 651-660 (2015)., **I** Wang, J. et al. Catal. Today 215, 186-193 (2013)., **J** Dorner, R. et al. Catal. Comm. 11, 816-819 (2010)., **K** Dorner, R. W. et al. Appl. Catal. A 373, 112-121 (2010)., **L** Pérez-Alonso et al. Catal. Comm. 9, 1945-1948 (2008).

Table 4.8 The catalytic performance of CO_2-LAO over washed and unwashed catalysts. [a]

Catalyst	Conv. (%)	CO Sel. (%)	Hydrocarbons Sel. (C-mol %)			Alkenes Sel. (C-mol %)		LAO/O[b] (%)	α[c]
			CH_4	C_{2-3}	C_{4-18}	$C_{4-18}^{=}$	$C_{2-18}^{=}$		
Fe/C	25.0	22.2	39.2	34.4	26.4	11.6	21.2	3.4	0.53
Fe/C-Chem	24.3	36.2	26.7	39.8	33.5	24.8	53.1	73	0.57
Fe/C-Bio-W[a]	27.9	24.1	15.8	28.5	55.7	47.1	72.5	65	0.70
Fe/C-Bio	30.5	23.2	11.8	24.4	63.8	50.3	72.0	80	0.72

Note. All the conversion and selectivity data are collected at a stable 4-6 h on stream a. In order to remove soluble potassium salt, 0.15g biopromoters were washed several times for several times with 1.5L distilled water; subsequently, the pre-treated biopromoters were added into 1.0g Fe/C; b. the ratio of linear α-$C_{4-18}^{=}$/$C_{4-18}^{=}$, LAO stands for linear α-C_{4-18} alkenes; c. The value of α is calculated based on C_{3-10} products.

Table 4.9 The catalytic performance of CO_2-LAO over various catalysts. [a]

Catalyst	Conv. (%)	CO Sel. (%)	Hydrocarbons Sel. (C-mol %)			Alkenes Sel. (C-mol %)		LAO/O[b] (%)	α[c]
			CH_4	C_{2-3}	C_{4-18}	$C_{4-18}^{=}$	$C_{2-18}^{=}$		
Fe/C	25.0	22.2	39.2	34.4	26.4	11.6	21.2	3.4	0.53
Fe/C-K, Ca, Mg	26.7	30.9	23.5	35.9	40.6	33.7	62.2	68	0.59
Fe/C-K, Ca, Mg, S	23.1	42.1	30.0	36.6	33.4	26.6	54.6	65	0.59

Note. All the conversion and selectivity data are collected at a stable 4-6 h on stream; a. Reaction conditions: 320 °C, 1.0 MPa, H_2/CO_2 = 3:1, W/F=10 g•h•mol^{-1}, Additive amount of biopromoters is 15 wt% (mass ratio of biopromoters to Fe/C powder); b. the ratio of linear α-$C_{4-18}^{=}/C_{4-18}^{=}$, LAO stands for linear α-C_{4-18} alkenes; c. The value of α is calculated based on C_{3-10} products. The reaction continued 6h and remained stable.

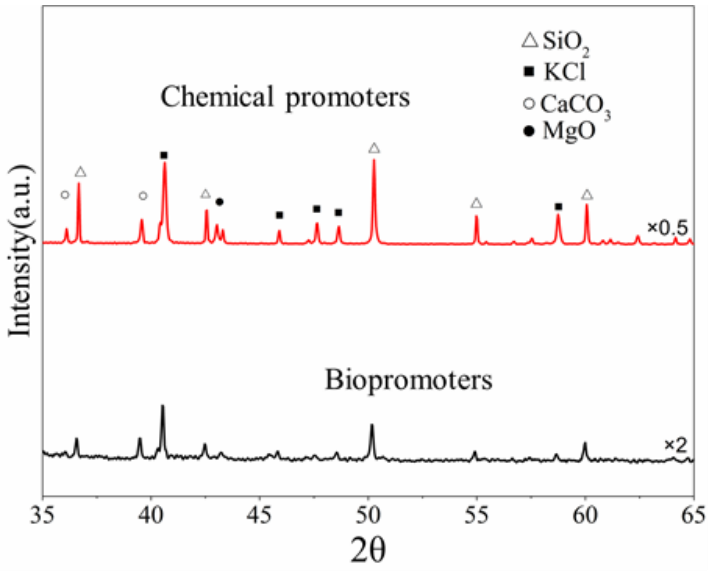

Figure 4.1 XRD patterns of the pre-treated CC ash (biopromoters) and the physical mixtures (chemical promoters) of KCl, $CaCO_3$, MgO, and SiO_2.

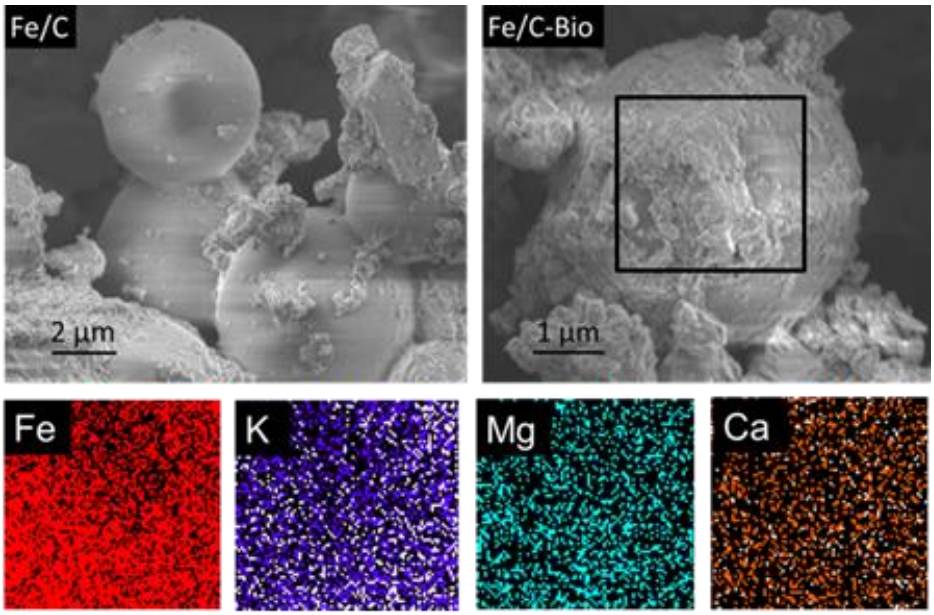

Figure 4.2 SEM images of fresh Fe/C and Fe/C-Bio and element maps of Fe, K, Mg and Si in Fe/C-Bio.

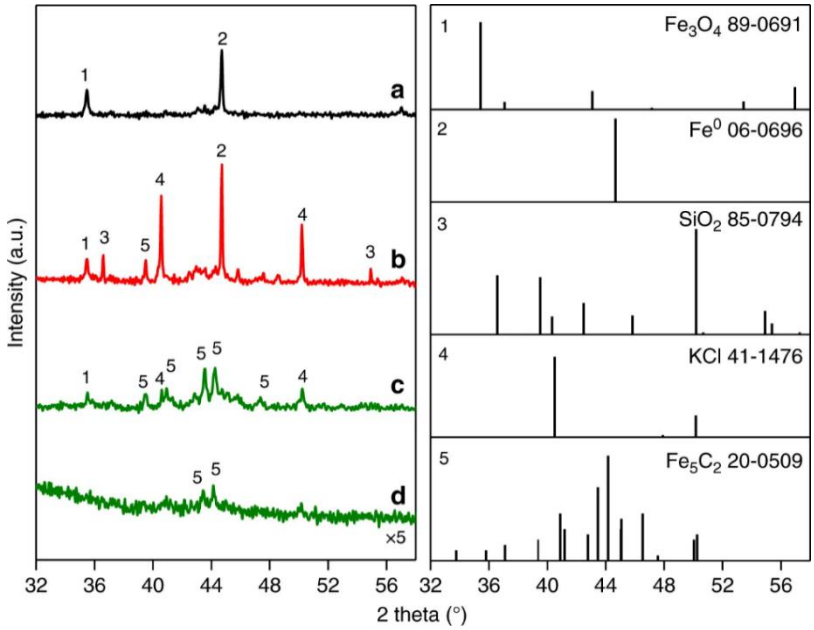

Figure 4.3 XRD patterns of various used catalysts. The Fe/C (a), Fe/C-Chem (b), and Fe/C-Bio (c) are derived after catalytic reaction for 6 h. (d) Fe/C-Bio catalyst after catalytic reaction for 100 h.

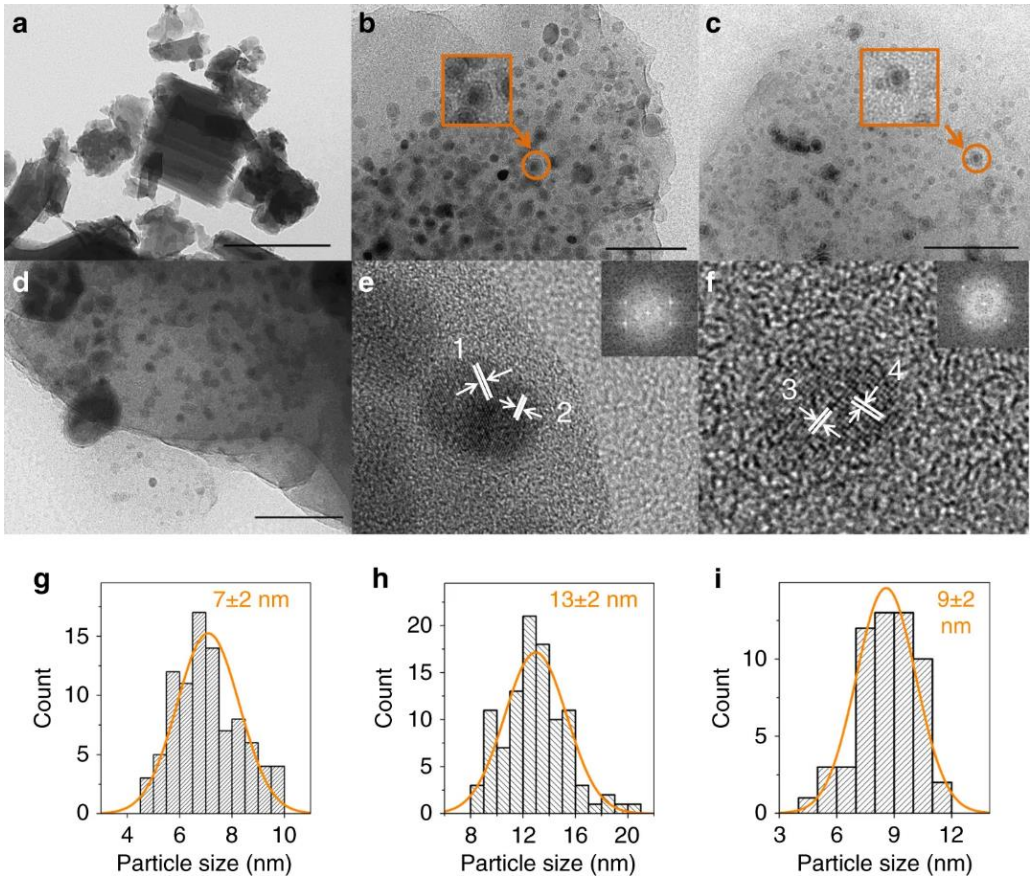

Figure 4.4 TEM images of catalysts. a Fresh Fe/C-Bio. b Fe/C-Chem used for 6 h. c Fe/C-Bio used for 6 h. d Fe/C-Bio used for 100 h. The lattice spacing 1 (or 2) of 2.96 Å corresponds to Fe_3O_4 (220). e High-resolution TEM images of Fe/C-Chem used for 6 h. The lattice spacing 3 of 2.50 Å and lattice spacing 4 of 2.93 Å corresponds to Fe_5C_2 (002) and Fe_5C_2 (310), respectively. f High-resolution TEM images of Fe/C-Bio used for 6 h. g Particle distribution of panel c. h Particle distribution of panel b. i Particle distribution of panel d. The scale bar for panel a, 500 nm. The scale bar for panels b–d, 100 nm.

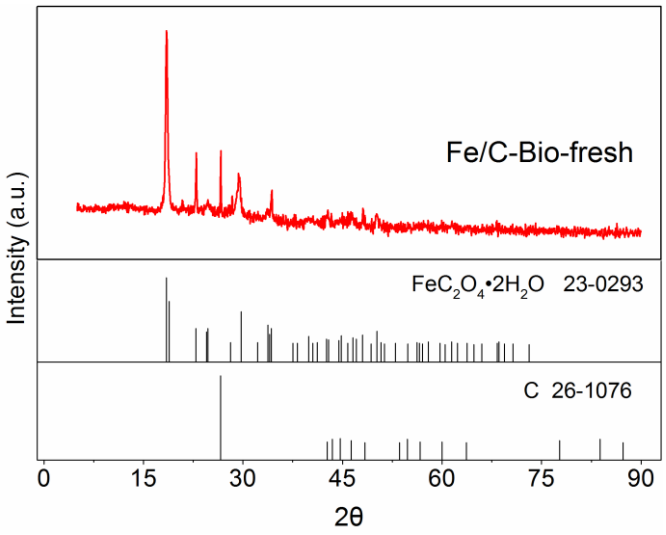

Figure 4.5 XRD patterns of the fresh Fe/C-Bio catalyst.

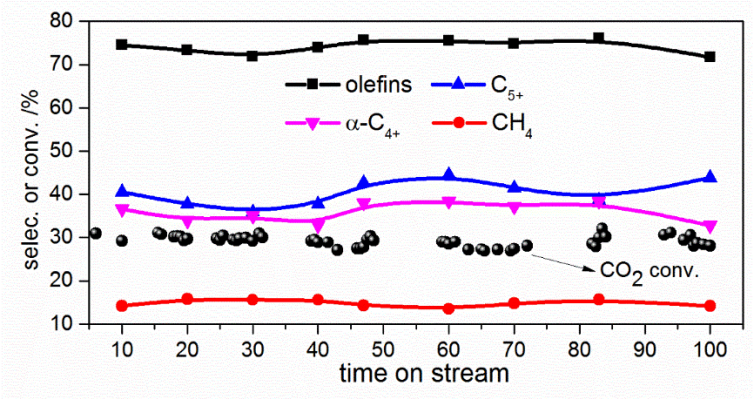

Figure 4.6 CO_2 Conversion and selectivity of hydrocarbons as a function of time on stream over the Fe/C-Bio catalyst. Reaction conditions: H_2/CO_2=3, P=1.0MPa, T=320 ^oC, Additive amount=15 wt%, W/F=10 g•h•mol^{-1}.

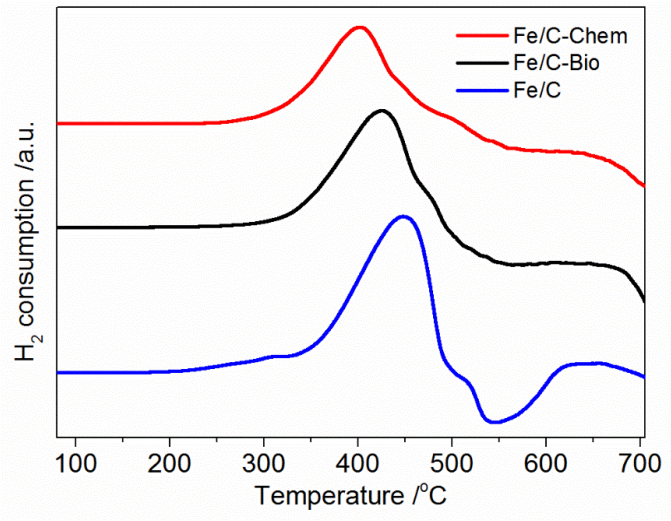

Figure 4.7 H_2-temperature programed reduction (H_2-TPR) curves of various catalysts.

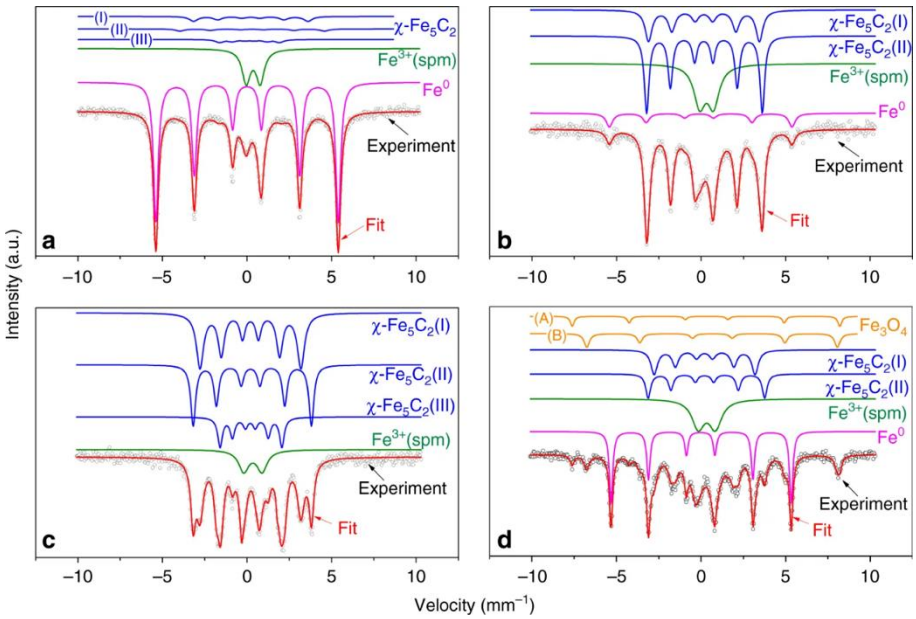

Figure 4.8 ^{57}Fe Mössbauer spectra of various catalysts. a Reduced Fe/C, b reduced Fe/C-Bio, c used Fe/C-Bio, and d used Fe/C-Chem. In each panel, the black scatter curve stands for the experiment data, and the red line stands for the calculated data by fitted. Data analyses were performed assuming a Lorentzian line-shape for computer folding and fitting. The components of iron phases were identified based on the Mössbauer parameters including isomer shift, quadruple splitting, and magnetic hyperfine field.

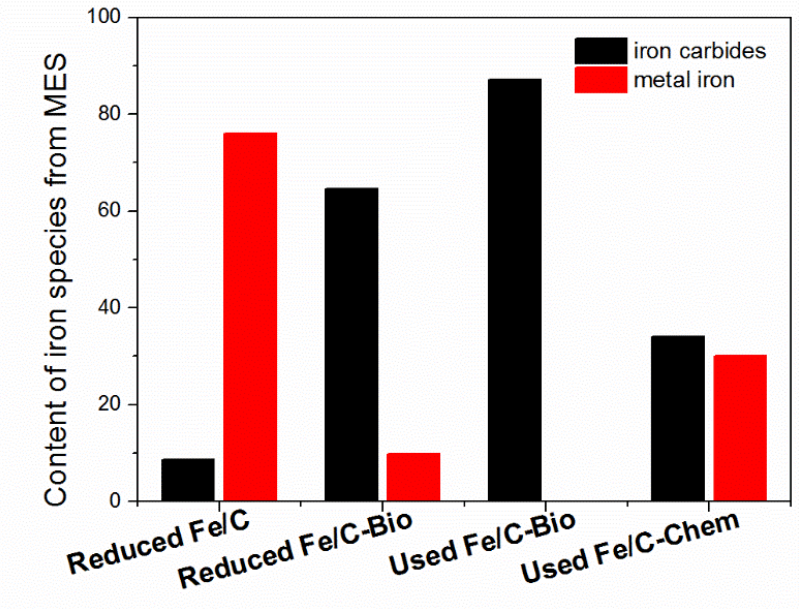

Figure 4.9 The content of iron species from MES in different catalysts.

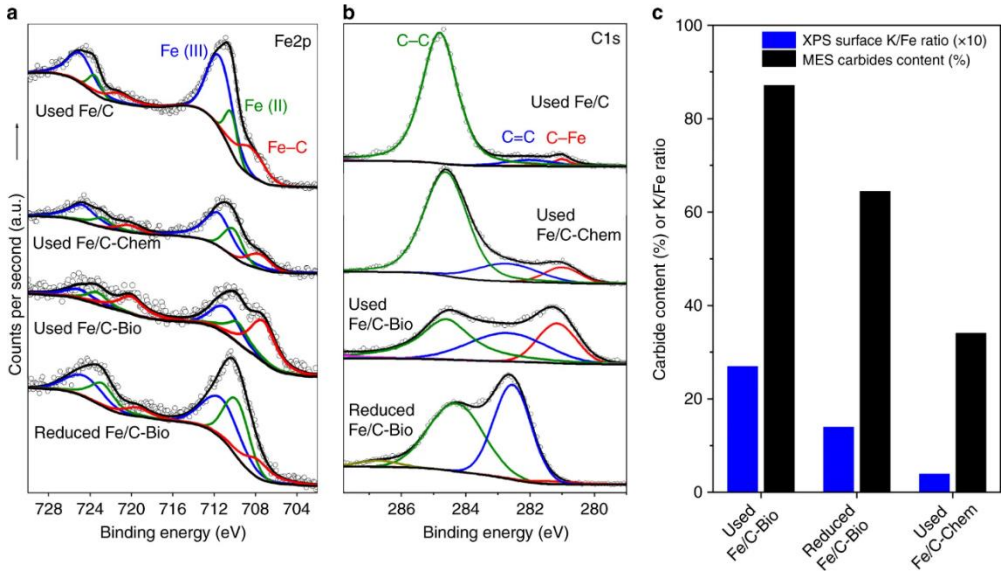

Figure 4.10 Surface analysis of different catalysts. Fe2p (a) and C1s (b) XPS spectra of used Fe/C, Fe/C-Bio, Fe/C-Chem, and reduced Fe/C-Bio. c The relationship between surface K/Fe ratio and carbides content in the catalysts. The carbides content and K/Fe ratio on surface is derived from XPS analysis, and the carbides content in bulk is calculated from ^{57}Fe Mössbauer spectra analysis.

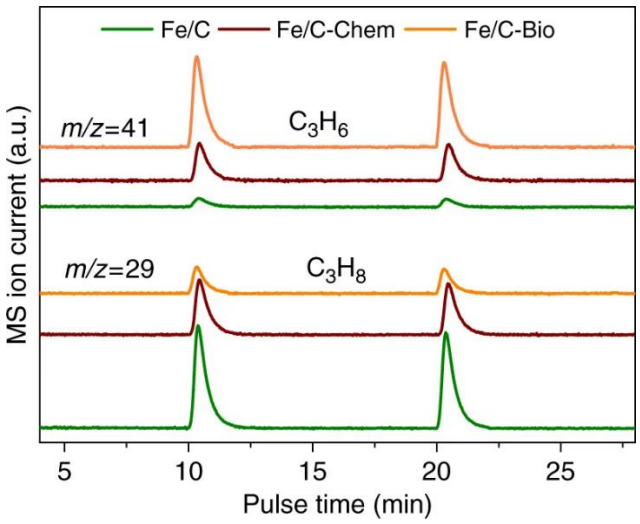

Figure 4.11 Characterization of hydrogenation ability by the pulse experiment of propylene. Before reaction, the catalysts (100 mg) were in situ reduced with H_2 (30 ml min^{-1}, 400 °C) and remained 90 min, then reacted in feed gas (20 ml min^{-1}, 0.1 MPa, 320 °C) for 30 min. After re-switching to a flow of H_2 (20 ml min^{-1}), propene of 120 μl was pulsed into the reactor with a certain time interval and detected by mass spectrometry.

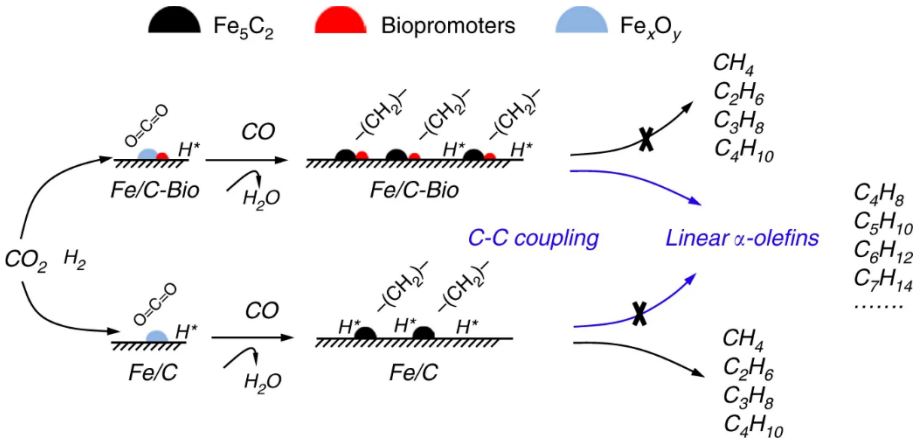

Figure 4.12 Reaction scheme for CO_2 hydrogenation to LAO. The existences of biopromoters weaken secondary hydrogenation of olefins and strengthen the reaction activity of C–C coupling.

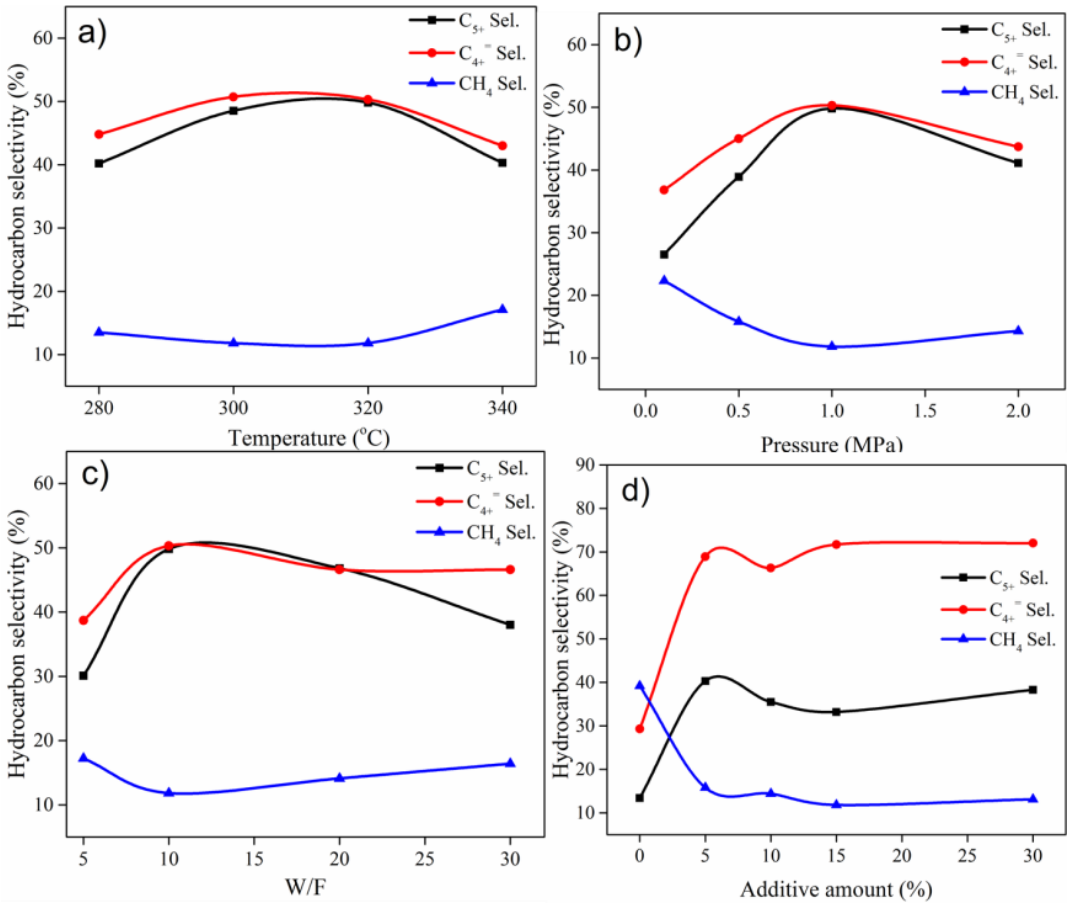

Figure 4.13 Hydrocarbon selectivity as a function of a) temperature, b) pressure, c) W/F, d) additive amount (mass ratio of biopromoters to Fe/C powder). (a) H_2/CO_2=3, P=1.0 MPa, W/F=10 g•h•mol^{-1}, Additive amount =15 wt%. (b) H_2/CO_2=3, T=320 °C, W/F=10 g•h•mol^{-1}, Additive amount=15 wt%. (c) H_2/CO_2=3, P=1.0 MPa, T=320 °C, Additive amount=15 wt%. (d) H_2/CO_2=3, T=320 °C, P=1.0MPa, W/F=10 g•h•mol^{-1}.

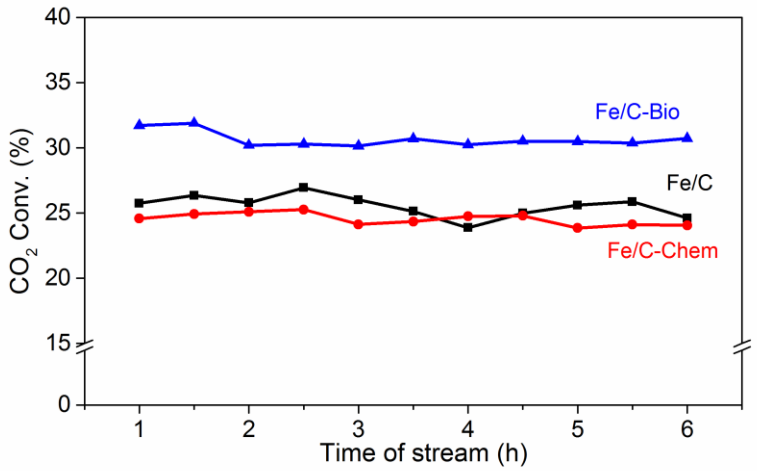

Figure 4.14 Time on-stream CO_2 conversion of different catalysts. Reaction conditions: H_2/CO_2=3, P=1.0MPa, T=320 ºC, Additive amount=15 wt%, W/F=10 g•h•mol^{-1}.

Chapter 5

Summary

Considering the stern environmental pressure and global ecologic problems caused by greenhouse gases, the reduction of CO_2 emissions from production and living has become one of more focused research topics in this century. Contrary to carbon capture and storage (CCS), the reutilization of catalyzing CO_2 to valuable chemicals or fuels provides a new path. Based on the concept of reutilization, plentiful studies have been done on CO_2 conversion including electrocatalysis, photocatalysis and thermalcatalysis.

In chapter 1, we designed a bimetallic Fe/Co catalyst through impregnation method for catalyzing CO_2 into liquid hydrocarbons. The introduction of cobalt metal increases the adsorption ability of CO_2, which promotes the CO_2 activation over iron species through RWGS reaction. Meanwhile, the introduction of cobalt metal further promotes the formation of carbides in comparison to potassium modified one, achieving a high C-C bond coupling activity. The CO_2 conversion activity is usually less than 40%, taking into account the thermodynamics under normal operation conditions. To further enhance the catalytic activity of CO_2 hydrogenation via the utilization of ex situ water removal manner, a two-stage reactor system was developed and investigated, where the water product formed by RWGS reaction was trapped in the first ice-trap and the mixtures sequentially entered the second reactor. Facts proved that ex situ water removal is of great significance in enhancing catalytic activity and reducing the selectivity of CO by-product. This effectively promotional effect derived from water removal facilitates constructing a new route for improving the catalytic performance of CO_2 conversion, further enhancing

the yield of liquid fuel.

In chapter 2, a nitrogen functionalized carbon with embedded iron nanoparticles was developed by a simple one-pot hydrothermal synthesis process for improving CO_2 hydrogenation performance. Thereinto, four different nitrogenous reagents (pyridine, ethylenediamine, and diethylformamide, and pyrrolidine) were adopted to synthesized the functionalized catalysts. The characterization and catalytic performance evaluation revealed that different nitrogen sources have various effects on physical-chemical properties of catalysts. In addition, we found that the presence of nitrogen-containing functional groups in the catalyst will affect the structural changes during the reaction, in which I_D/I_G intensity is a visual manifestation. The improved CO_2 hydrogenation performance over these functionalized catalysts was found to be correlated with the specific surface areas, the carbonization degree of iron species precursor, the amount of defect sites, and the content of pyridine-like nitrogen structures, which are determined by the doping nitrogen atom types. Pyrrolidine as a well-performing nitrogen source precisely regulated the physiochemical properties of the final catalyst, consequently achieving an outstanding performance.

In chapter 3, a promising Ni based mesoporous Al_2O_3 catalyst was prepared by one-step evaporation-induced self-assembly (EISA) method, and was employed as an efficient catalyst in combined methane dry reforming (DRM) and methane partial oxidization (POM) reaction. In order to further elaborate the advantages of one-step preparation method, nickel based catalysts supported by mesoporous alumina were also prepared by impregnation method. The catalytic activity tests results indicated that the catalysts prepared by the one-pot method had better catalytic performance for combined methane dry reforming and methane partial oxidation reaction, which can be ascribed to the larger

exposed metal Ni surface area of Ni-MA than that of Ni/MA. Meanwhile, the catalytic performance remained stable at 750 °C for 100 h reaction. The characterization results of used catalysts indicated that combined POM with DRM could effectively suppress carbon deposition.

In chapter 4, we designed a biopromoters-modified iron catalyst for catalyzing CO_2 into olefins. CO_2 hydrogenation to olefin process achieves 72% selectivity for alkenes and 50.3% selectivity for C_{4-18} alkenes, of which formation of linear α-olefins accounts for 80%. The process is catalyzed by carbon-supported iron, commonly used in C-C propagation reactions, with multiple alkali promoters extracted from waste corncob. The design is based on the synergistic catalysis of mineral elements in biomass enzyme on which carbon dioxide can be directly converted into carbohydrate. The mineral elements from corncob may promote the surface enrichment of potassium, suppressing the secondary hydrogenation of alkenes on active sites. Furthermore, carburization of iron species is enhanced to form more Fe_5C_2 species, promoting both the reverse water-gas shift reaction and subsequent C-C coupling. More importantly, *in situ* pulse experiments showed that the addition of promoters will suppress the hydrogenation of olefins, and biopromoters-modified iron catalyst shows higher habitation ability towards olefins hydrogenation than chemical promoters, thus it presents a high selectivity of LAOs.

List of Publications

1. **Lisheng Guo**, Yu Cui, Peipei Zhang, Xiaobo Peng, Yoshiharu Yoneyama, Guohui Yang, Noritatsu Tsubaki. Enhanced Liquid Fuel Production from CO_2 hydrogenation: Catalytic Performance of Bimetallic Catalysts over a Two-stage Reactor System. ***ChemistrySelect***, 2018, 3, 13705-13711. IF=1.811
2. **Lisheng Guo**, Peipei Zhang, Yu Cui, Guangbo Liu, Jinhu Wu, Guohui Yang, Yoshiharu Yoneyama, Noritatsu Tsubaki. One-Pot Hydrothermal Synthesis of Nitrogen Functionalized Carbonaceous Material Catalysts with Embedded Iron Nanoparticles for CO_2 Hydrogenation. ***ACS Sustainable Chemistry & Engineering***, 2019, 8331-8339. IF=7.632
3. **Lisheng Guo**, Jian Sun, Xuewei Ji, Jian Wei, Zhiyong Wen, Ruwei Yao, Hengyong Xu, Qingjie Ge. Directly Converting Carbon Dioxide to Linear α-Olefins on Bio-promoted Catalysts. ***Communications Chemistry*** (**highlight** by Commun Chem, selected as **Green Chemistry** content by Nature Family Journal), 2018, 1, 11. IF=4.253
4. Qingxiang Ma, **Lisheng Guo**, Yuan Fang, Hangjie Li, Jiangli Zhang, Tian-Sheng Zhao, Guohui Yang, Yoshiharu Yoneyama, Noritatsu Tsubaki. Combined methane dry reforming and methane partial oxidization for syngas production over high dispersion Ni based mesoporous catalyst. ***Fuel Processing Technology***, 2019, 188, 98-104. IF=4.982
5. **Lisheng Guo**, Jie Li, Rungtiwa Kosol, Yu Cui, Naoya Kodama, Xiaoyu Guo, R. Prasert, V. Tharapong, Guangbo Liu, Jinhu Wu, Guohui Yang, Yoshiharu Yoneyama,

Noritatsu Tsubaki. Heteroatom Doped Iron Based Catalysts Prepared by Urea Self-Combustion Method for Efficient CO_2 Hydrogenation. ***Fuel***, 2020, 267, 118102. IF=5.578

6. **Lisheng Guo**, Yu Cui, Hangjie Li, Yuan Fang, Reubroycharoen Prasert, Jinhu Wu, Guohui Yang, Yoshiharu Yoneyama, Noritatsu Tsubaki. Selective formation of linear-alpha olefins (LAOs) by CO_2 hydrogenation over bimetallic Fe/Co-Y catalyst. ***Catalysis Communications***, 2019, 105759. IF=3.612
7. **Lisheng Guo**, Jian Sun, Qingjie Ge, Noritatsu Tsubaki. Recent Advances of Direct Catalytic Hydrogenation of Carbon Dioxide to Valuable C_{2+} Hydrocarbons. ***Journal of Materials Chemistry A***, 2018, 6, 23244-23262. IF=11.301
8. **Lisheng Guo**, Jian Sun, Jian Wei, Zhiyong Wen, Hengyong Xu, Qingjie Ge. Fischer-Tropsch synthesis over iron catalysts with corncob-derived promoters. ***Journal of Energy Chemistry***, 2018, 26, 632-638. IF=7.216
9. **Lisheng Guo**, Jie Li, Yu Cui, Rungtiwa Kosol, Yan Zeng, Guangbo Liu, Jinhu Wu, Tian-Sheng Zhao, Guohui Yang, Lishu Shao, Peng Zhan, Jienan Chen, Noritatsu Tsubaki. Spinel-structure catalyst catalyzing CO_2 hydrogenation with an ultra-high yield. ***Chemical Communications***, 2020, 56, 9372-9375. IF=5.996
10. Jian Sun, **Lisheng Guo**, Qingxiang Ma, Xinhua Gao, Noriyuki Yamane, Hengyong Xu, Noritatsu Tsubaki. Functionalized Natural Carbon Supported Nanoparticles as Excellent Catalysts for Hydrocarbon Production. ***Chemistry-An Asian Journal***, 2017, 12, 366-371. **(Co-first author, Hot paper)** IF=4.056
11. Xiaoyu Guo, **Lisheng Guo**, Yu Cui, Tharapong Vitidsant, Prasert Reubroycharoen, Guangbo Liu, Jinhu Wu, Yoshiharu Yoneyama, Guohui Yang, Noritatsu Tsubaki. Enhanced α-olefins selectivity by promoted CO adsorption on ZrO_2@FeCu catalyst.

Catalysis Today, 2020, DOI: 10.1016/j.cattod.2020.03.049. IF=5.825

12. Xiaoyu Guo, **Lisheng Guo**, Yan Zeng, Rungtiwa Kosol, Xinhua Gao, Yoshiharu Yoneyama, Guohui Yang, Noritatsu Tsubaki. Catalytic oligomerization of isobutyl alcohol to jet fuels over dealuminated zeolite Beta. ***Catalysis Today***, 2020, DOI: 10.1016/j.cattod.2020.04.047. IF=5.825
13. Hongli Wu, **Lisheng Guo**, Fengyun Ma, Yuelan Wang, Wenlong Mo, Xing Fan, Hangjie Li, Yuming Yu, Inamullah Miana, Noritatsu Tsubaki. Structure and surface characteristics of Fe-promoted Ni/Al_2O_3 catalysts for hydrogenation of 1, 4-butynediol to 1, 4-butenediol in a slurry-bed reactor. ***Catalysis Science & Technology***, 2019, 9, 6598-6605. **(Hot paper)** IF=5.721
14. Yuan Fang, **Lisheng Guo**, Yu Cui, Peipei Zhang, Yoshiharu Yoneyama, Guohui Yang, Noritatsu Tsubaki. NaBH4 In-situ Reduced Cobalt Catalyst Supported on Zeolite A for 1-Hexene Hydroformylation. ***ChemistrySelect***, 2019, 4, 10447-10451. IF=1.811
15. Xiaoyu Guo, **Lisheng Guo**, Yuichi Suzuki, Jinhu Wu, Yoshiharu Yoneyama, Guohui Yang, Noritatsu Tsubaki. Catalytic Oligomerization of Isobutyl Alcohol to Hydrocarbon Liquid Fuels over Acidic Zeolite Catalysts. ***ChemistrySelect***, 2020, 5, 528–532. IF=1.811
16. AL-Hassan Nasser, **Lisheng Guo**, Hamada ELnaggar, Yang Wang, Xiaoyu Guo, Ahmed Abdel Moneim and Noritatsu Tsubaki. Mn-Fe nanoparticles on a reduced graphene oxide catalyst for enhanced olefin production from syngas in a slurry reactor. ***RSC Advances***, 2018, 8, 14854-14863. IF=3.119
17. Li Tan, Peipei Zhang, Yu Cui, Yuichi Suzuki, Hangjie Li, **Lisheng Guo**, Guohui Yang, Noritatsu Tsubaki, Direct CO_2 hydrogenation to light olefins by suppressing CO by-product formation. ***Fuel Processing Technology***, 2019, 196, 106174. IF=4.982

18. Li Tan, Peipei Zhang, Yuichi Suzuki, Hangjie Li, **Lisheng Guo**, Yoshiharu Yoneyama, Jiangang Chen, Xiaobo PENG, Noritatsu Tsubaki. Bifunctional capsule catalyst of Al_2O_3@Cu with strengthened dehydration reaction field for direct synthesis of dimethyl ether from syngas. ***Industrial & Engineering Chemistry Research***, 2019, 58, 22905-22911. IF=3.573
19. Hangjie Li, Peipei Zhang, **Lisheng Guo**, Yingluo He, Yan Zeng, Montree Thongkam, Jaru Natakaranakul, Tatsuki Kojima, Prasert Reubroycharoen, Tharapong Vitidsant, Guohui Yang, Noritatsu Tsubaki. A Well-Defined Core-Shell Structured Capsule Catalyst for Direct Conversion of CO_2 into Liquefied Petroleum Gas. ***ChemSusChem***, 2020, 13, 2060-2065. IF=7.962
20. Hongli Wu, Meng Zou, **Lisheng Guo**, Fengyun Ma, Wenlong Mo, Yuming Yu, Inamullah Mian, Jingmei Liu, Shuangjie Yin, Noritatsu Tsubaki. Effects of calcination temperatures on the structure-activity relationship of Ni-La/Al_2O_3 catalysts for syngas methanation. ***RSC Advances***, 2020, 10, 4166-4174. IF=3.112
21. Yu Cui, Shingo Asano, Jie Li, Yuuya Araki, **Lisheng Guo**, Noritatsu Tsubaki. Jet Fuel Synthesis from Syngas and Carbon Dioxide. ***Journal of the Hydrogen Energy Systems Society of Japan***, 2020, 45, 16-24.

List of Conferences

1. Enhanced Liquid Hydrocarbon Fuel Production from CO_2 Hydrogenation: Catalytic Performance of Bimetallic Catalysts with a Two-stage Reactor System. 49th Petroleum-Petrochemicals Symposium of JPI, Yamagata, Japan, Oct 31-Nov 1, 2019. **Oral**
2. Nitrogen-Doped Carbon Supported Iron Catalysts for CO_2 Hydrogenation. 124th Catalysis Society of Japan Meeting, Oral, Nagasaki, Japan, Sep 18-20, 2019. **Oral**
3. Directly Converting Carbon Dioxide to Linear α-Olefins on Bio-promoted Catalysts. 12th Natural Gas Conversion Symposium (NGCS), San Antonio, United States, June 1-6, 2019. **Rapid presentation**
4. Enhanced Liquid Fuel Production from CO_2 hydrogenation: Catalytic Performance of Bimetallic Catalysts with a Two-stage Reactor System. 123rd Catalysis Society of Japan Meeting, Osaka, Japan, March 21-22, 2019. **Poster**

Acknowledgements

I would like to express my heartfelt gratitude to Professor Noritatsu Tsubaki for his constant encouragement, valuable guidance, constructive comments, and innovative suggestions through the course of this thesis. What is more important is that his profound erudition and rigorous attitude to science influenced me deeply, inspiring me to move towards the scientific way of passing the future. Without his pushing me ahead, encouragement and guidance, I could not have completed this thesis.

I am greatly appreciative to Associate Professor Yoshiharu Yoneyama and Associate Professor Guohui Yang for the kind assistance in the experiment. Meanwhile, I am grateful to members in Tsubaki lab for their supports and many helpful discussions. They are Dr. Jie Li, Dr. Peipei Zhang, Dr. Li Tan, Dr. Xinhua Gao, Dr. Yang Wang, Dr. Xiaobo Feng, Mr. Yu Cui, Mr. Fei Chen, Mr. Xiaoyu Guo, Mr. Heng Zhao, Mr. Jiaming Liang, Mr. Naoya Kodama, Mr. Hangjie Li, Ms. Yuan Fang, Mr. Yinglue He, Ms. Yan Zeng. I am also grateful to the UNIVERSITY for the financial help during the difficult period of the epidemic. Besides, I also want to thank Professor Qingjie Ge, Professor Jian Sun and many other teachers for their assistance in study and life.

Finally, thanks to my esteemed parents and my beloved for encouragement, which give me the strongest support to lead me forward, I was able to successfully fulfill my study during PhD period. My words here cannot express all my feeling and appreciations. Only with their support have I been able to accomplish the PhD study. Likewise, the scholarship from China Scholarship Council (CSC) is acknowledge from my heart.